Title
Glassy Dynamics on a Lattice and in Nature

Author
Schuster, Kelsey Carle

Publication Date
2016

Glassy Dynamics on a Lattice and in Nature

By

Kelsey Carle Schuster

A dissertation submitted in partial satisfaction of the

requirements for the degree of

Doctor of Philosophy

in

Chemistry

in the

Graduate Division

of the

University of California, Berkeley

Committee in charge:

Professor David Chandler, Chair
Professor Phillip L. Geissler
Professor Joel E. Moore

Summer 2016

Glassy Dynamics on a Lattice and in Nature

Abstract

Glassy Dynamics on a Lattice and in Nature

by

Kelsey Carle Schuster

Doctor of Philosophy in Chemistry

University of California, Berkeley

Professor David Chandler, Chair

When a liquid is cooled below its melting temperature under conditions that prevent it from crystallizing, it forms an amorphous solid, or "glass." Glass-forming materials are ubiquitous, ranging from familiar silica glasses of which everyday windows are composed, to liquid water. While structurally indistinguishable from high-temperature liquids, supercooled liquids exhibit rich and complex dynamics. For instance, as the temperature is lowered, structural reorganization within supercooled liquids occurs over increasingly long time scales. Inspecting atomistic mobility over an interval of time reveals that dynamics is "heterogeneous," with distinct regions of mobility and immobility in space-time. In this dissertation, we characterize glassy dynamics in experimental systems and in coarse-grained lattice models. We show how the characteristic dynamics of atomistic glass-forming materials can be reproduced using a kinetically constrained lattice model referred to as the Arrow model, and thus present glassy dynamics "on a lattice." We then show that combining the Arrow model with a second lattice model that undergoes a thermodynamic phase transition captures the competition between crystallization and glass formation experienced by a material cooled below its melting temperature. With this combined model, we demonstrate how specific cooling protocols influence polycrystalline structure, and we qualitatively reproduce the non-monotonic temperature dependence of crystallization time scales. Finally, we explore glassy dynamics "in nature" by applying many of the same tools and ideas used to characterize glasses to study dynamical features of protein side-chains. We demonstrate the presence of supercooled liquid-like dynamics in a biomolecular system.

To Nathan

Acknowledgements

First and foremost, I would like to thank my family for their unwavering love and support. My parents, James and Carla, always emphasized the value of education and made me believe that with hard work, I could accomplish nearly anything I set out to do. I thank them for believing in me and encouraging me to pursue my interests, even when those interests took me all the way to California. I thank my grandmother Jean for being one of my earliest examples of a strong, capable woman; I strive to emulate her kindness, humor, perseverance, and dedication to family. I thank my siblings, Brenna and Taylor, for being two of my best friends and for reminding me to not take myself too seriously (Brenna's husband Scott also helps with this). I recently married into the Skinner family, who have welcomed me as one of their own. I thank Larry, Laura, Blair, Michelle, Wesley, and Carey for the joy they've brought to my life (and for allowing me to marry their son/brother!). I'm proud to call them family.

Academically, I owe much thanks to my adviser, David Chandler. He took me on as a student—even though I had little previous experience with theoretical chemistry—and was patient with me as I learned. He has served as an excellent mentor, always offering enough guidance for me to make progress, while still encouraging me to explore solutions on my own. David's passion for science and dedication to communicating knowledge is truly inspiring, and it has been a privilege to be a member of his research group.

Prior to my time in Berkeley, my academic trajectory was influenced by Wheaton College, my undergraduate institution. Peter Walhout introduced me to physical chemistry as my professor, and scientific research as my research adviser. I am thankful for his guidance as I navigated the graduate school application process and eventually decided on UC Berkeley. Although I didn't continue with experimental chemistry research post-Wheaton, my work with Dr. Walhout taught me to think critically about research problems.

I am deeply indebted to Aaron Keys and David Limmer, the senior members of the Chandler group when I first joined. They patiently answered my many questions, showed me how to effectively present research, and demonstrated how to be successful in the group. Aaron served as my mentor when I joined, and in addition to getting me situated studying glassy dynamics, he helped me greatly improve my technical skills. I would also like to thank fellow Chandler group members Kranthi Mandadapu, Milo Lin, Dayton Thorpe, Alex Hudson, Jonathan Landy, and Shachi Katira for helpful discussions and fruitful collaborations. Kranthi, in particular, worked with me on the results presented in Chapter 4 of this dissertation. A special thanks to Cheryl Higley and Leslie Dietterick, the wonderful Chandler group administrative assistants, for keeping the group running smoothly.

Over the course of my time at UC Berkeley, I was fortunate to interact with talented researchers outside of the Chandler group. Geissler group members Todd Gingrich, Patrick Shaffer, Anna Schneider, Chris Ryan, Suri Vaikuntanathan, Michael Gruenwald, Katie Klymko, Grant Rostkoff, John Haberstroh, and others contributed to the friendly and collaborative atmosphere in the Pitzer Center. I had the privilege of working with Greg Bowman when he was a Miller Fellow at Berkeley; the final chapter of this dissertation is a result of our collaboration. I thank Phill Geissler for allowing me to gain experience with theoretical chemistry in his group over the summer before I started graduate school, and for offering helpful feedback on my research and dissertation in the years following. Phill's expert teaching of both semesters of graduate statistical mechanics provided a sound foundation for the research I completed in the Chandler group. I thank Naomi Ginsberg for giving me the opportunity to serve as a graduate student instructor for her statistical mechanics course. Naomi's enthusiasm about the material was obvious in every lecture she gave, and I became a better teacher by working with her. I thank Joel Moore, Martin Head-Gordon, and Jamie Cate for serving on my qualifying exam committee and providing helpful feedback on my research.

I am incredibly thankful for the friendships I made during my time in Berkeley. My current and former roommates—Cheri Ackerman, Sarah Gitman, Caitie Cook, and Lindsey Osimiri—made the time spent at my apartment much more enjoyable. I'm so glad we lived together. I met Avery Lindeman and Camila Bacellar when we were fellow chemistry first-years, but I never could have predicted how much they would come to mean to me. From dinner dates, to rooftop brunches, to football and baseball games, to road trips across California; we did it all together. Their friendship made my years in graduate school so much happier.

Finally, I thank Nathan, my husband and best friend. He wholly supported my decision to pursue a Ph.D. at UC Berkeley, even though it meant we would have to live apart for the duration of my degree. He always believed I would succeed and has been a constant source of joy and encouragement during my time in graduate school. I am incredibly grateful for his love and support; I don't think I could have done it without him. And after years of Skype dates and cross-country visits, we will finally be together.

Contents

List of Figures

List of Tables

Chapter 1

Introduction

1.1 The Glass Transition

The characteristic dynamics of glass-forming materials is the unifying theme of the research presented in this dissertation. When a liquid is cooled below its melting temperature T_{m} in a manner that allows the constituent molecules to reorganize into a crystalline structure, it undergoes a first-order phase transition to an ordered solid. However, some preparations of the material may not permit this reorganization. For example, cooling the liquid to temperatures below T_{m} at a fast rate may result in a supercooled liquid state below the melting temperature. The supercooled liquid state is structurally indistinguishable from a high-temperature ($T > T_{\mathrm{m}}$) liquid but has rich dynamics, as discussed below in Section 1.1.1.

The crystal state is the thermodynamically stable state below T_{m} (i.e., the free energy of the crystal state is lower than that of the supercooled liquid state), and so the supercooled liquid is said to be "metastable." There is a significant enough barrier to crystallization that the supercooled liquid is only able to crystallize over very long time scales. As the supercooled liquid is cooled further, particles in the metastable liquid are no longer able to relax over time scales relevant to the experiment. It is at this point that the liquid falls out of equilibrium and forms a "glass," a solid material with amorphous structure. The temperature at which this transition occurs is known as the "glass transition temperature" T_{g}; the specific value of T_{g} depends on both the material and its preparation [1]. The glass transition is not a first-order thermodynamic phase transition like that from liquid to crystal, where the phase transition occurs in configuration space. Rather, it is a first-order *dynamical* transition and occurs in trajectory space [2]. Fig. 1.1 shows a schematic of the glass transition, where the freezing transition and glass transitions corresponding to two different cooling protocols are indicated.

1.1.1 Dynamical Properties of Supercooled Liquids

While supercooled liquid structure cannot be distinguished from high-temperature liquid structure, their dynamical properties are distinct [1, 5]. Here we discuss several of the

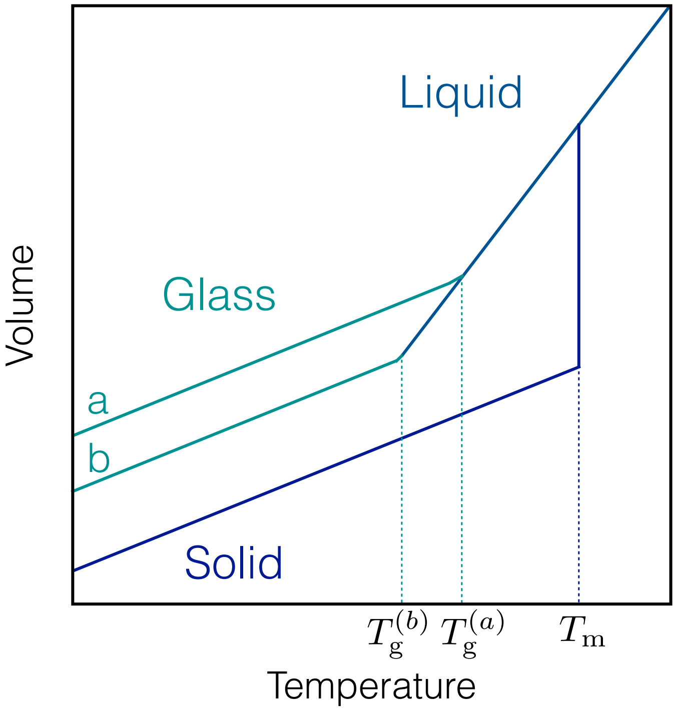

Figure 1.1: Illustration of the glass transition. As a liquid is cooled through its melting temperature T_{m}, it will either crystallize and experience a sudden decrease in volume, or it will become supercooled [3, 4]. Continuing to cool the supercooled liquid will eventually result in the liquid falling out of equilibrium to form an amorphous solid, or glass. The temperature T_{g} at which the glass transition occurs depends on the cooling protocol.

most important dynamical changes that take place when a liquid is cooled below its melting temperature in a manner that prevents it from crystallizing.

Super-Arrhenius Relaxation

The structural relaxation time τ gives the timescale over which microscopic reorganization occurs in a liquid. At temperatures above the melting temperature T_m, τ grows exponentially with temperature

$$\tau \propto \exp(E/k_\mathrm{B}T) \tag{1.1}$$

where E is the energetic barrier to relaxation and k_B is Boltzmann's constant. Below T_m, the time to reorganize a microscopic region of the liquid grows significantly faster with decreasing temperature [1, 6]. The temperature-dependence becomes super-Arrhenius

$$\tau \propto \exp(A[1/k_\mathrm{B}T - 1/k_\mathrm{B}T_\mathrm{o}]^2) \tag{1.2}$$

where A is a constant that incorporates the energy scale for facilitating new dynamics, and $T_\mathrm{o} \approx T_\mathrm{m}$ is the onset temperature of glassy dynamics. Fig. 1.2 shows a representative plot of structural relaxation time as a function of inverse temperature, where the onset of glassy dynamics is indicated.

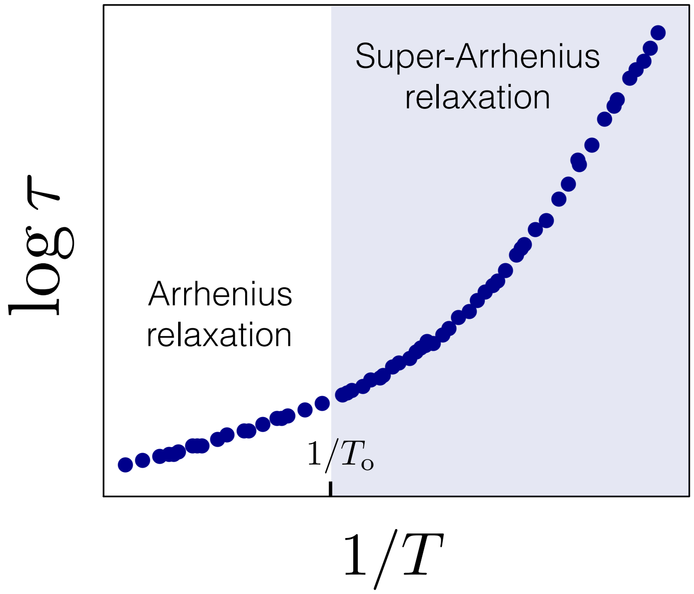

Figure 1.2: Structural relaxation time as a function of temperature. The logarithm of the structural relaxation time of boron oxide [7] is plotted as a function of inverse temperature. At temperatures above T_o, relaxation is Arrhenius. Below T_o, reorganization in the liquid becomes increasingly sluggish, and relaxation occurs over significantly longer timescales.

The full form of Super-Arrhenius relaxation at temperatures $T < T_\mathrm{o}$ is known as the "parabolic law" [8, 9], which is introduced in Section 1.2.2 and is the subject of Chapter

2. The parabolic law collapses structural relaxation and viscosity data from a diverse set of experimental and numerical systems, demonstrating a universality in supercooled liquid dynamics.

Heterogeneous Dynamics

At temperatures above the onset of glassy dynamics, microscopic reorganization of liquid particles occurs relatively unhindered throughout the spatial extent of the liquid. However, upon supercooling the liquid, spatial regions of mobility and immobility emerge; specifically, different spatial regions of the liquid relax over different timescales [10]. Dynamics is said to be "heterogeneous." Fig. 1.3 shows a visualization of a two-dimensional supercooled liquid, where particles are colored based on how far they have displaced over a time interval Δt. Relatively immobile particles are colored dark blue, and particles that have displaced at least a particle diameter are colored red.

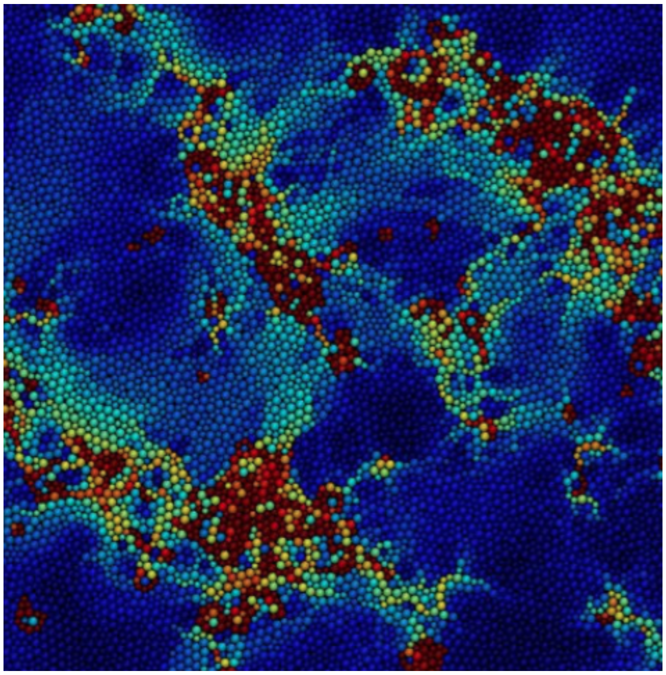

Figure 1.3: Heterogeneous dynamics in a supercooled liquid. Supercooled liquid particles in a 2D-68:32 system [11] are colored from dark blue to dark red depending on how far they have displaced over a time window Δt. Dark red particles have traveled at least one particle diameter; the darkest blue particles are immobile. This figure was originally published as Figure 1 in Ref. [10] under the terms of the *Creative Commons Attribution 3.0 License* (https://creativecommons.org/licenses/by/3.0/). The original figure was cropped for inclusion in this dissertation.

Fig. 1.3 clearly reveals clustering of mobile and immobile regions. Each mobile region of the supercooled liquid emerges from an "excitation," a small region of the liquid where, due to underlying structural features, microscopic reorganization is possible. Above T_{o}, excitations exist throughout the liquid and so all particles are free to reorganize. The concentration of excitations decreases as the temperature decreases and so mobile regions become sparse [10], as illustrated in Fig. 1.3.

Temporal Correlations

It is clear from Fig. 1.3 that particle mobility in a supercooled liquid is correlated in space. Particles that were very mobile over Δt tend to be clustered together, while the least mobile particles are surrounded by other immobile particles. In addition to exhibiting correlations in space, supercooled liquid dynamics are also correlated in time [12]. This is intuitive when we consider that particles in a mobile region of the liquid will likely experience many relaxation events over a relatively short period of time, while particles in a region of immobility may wait for a long time to relax. In other words, a relaxation event is indicative of a particle's presence in a mobile region, and so subsequent relaxation events are likely to follow.

Exchange and persistence times [13, 14, 12] are frequently used to quantify the degree to which time-correlated dynamics exists in systems with glassy dynamics. Exchange and persistence times are defined mathematically and discussed in more detail in Chapters 3 and 5; here, we give a qualitative description of these metrics and what they reveal about correlated dynamics at low temperatures.

A "persistence time" for a particle in the liquid is defined as the waiting time until that particle relaxes, and an "exchange time" is the time between subsequent relaxation events. In a system without temporal correlations, distributions of persistence and exchange times for all particles in the system will be the same. In a system where relaxation events are correlated in time, the persistence distribution will be dominated by long waiting times from spatial regions of immobility. The exchange and persistence distributions will therefore appear decoupled, with mean persistence and mean exchange times differing by up to several orders of magnitude. Decoupling is a key indicator of heterogeneous dynamics.

1.1.2 Theories of the Glass Transition

The nature of the glass transition is a rich and controversial subject, and significant effort has been devoted to understanding the underlying physics [1]. Several prominent theories exist in the literature, including mode-coupling theory (MCT) [15], Adam-Gibbs theory [16], random first order transition theory (RFOT) [17], and dynamical facilitation theory [18, 19]. While MCT, Adam-Gibbs theory, and RFOT are concerned with free energy landscapes of configurations, dynamical facilitation theory is unique in that it focuses on microscopic dynamics. Dynamical facilitation theory has been successful in predicting a universal collapse of transport properties of glass-forming materials [8, 9], as well as explaining heat capacity behavior when cooling and warming through the glass transition [20], and so is the only theory discussed here. The dynamical facilitation theory of the glass transition is described below and motivates work in subsequent chapters.

1.2 Dynamical Facilitation Theory

The dynamical facilitation theory of the glass transition [18, 19] is motivated by a microscopic view of particle dynamics. Specifically, supercooled liquid particles moving in a specific direction facilitate mobility of neighboring particles, which displace in that same general direction. In this sense, dynamics is both *facilitated* and exhibits *directionality*. Fig. 1.4 shows a close-up view of simulated particle dynamics in the system shown in Fig. 1.3, with color once again indicating how far each particle has displaced, and arrows indicating the directions of displacement.

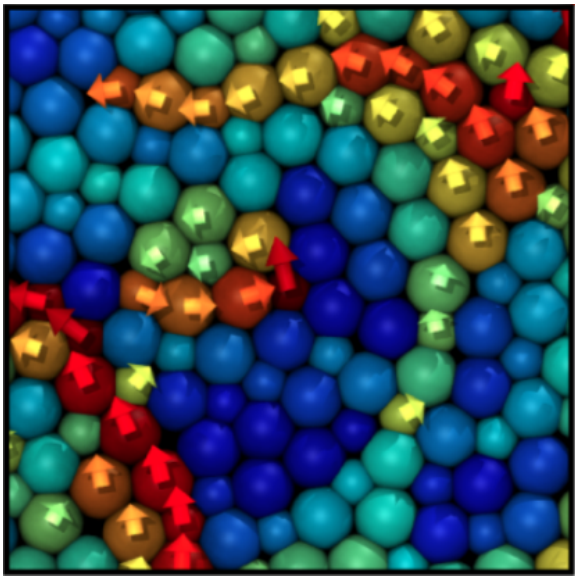

Figure 1.4: Facilitated, directed dynamics in a supercooled liquid. Supercooled liquid particles in a 2D-68:32 system [11] are colored from dark blue to dark red depending on how far they have displaced after a time window Δt. Dark red particles have traveled at least one particle diameter; dark blue particles are immobile. Arrows indicate the directions of displacement for individual particles. This figure was originally published as Figure 1 in Ref. [10] under the terms of the *Creative Commons Attribution 3.0 License* (https://creativecommons.org/licenses/by/3.0/). The original figure was cropped for inclusion in this dissertation.

1.2.1 Kinetically-Constrained Models

The dynamical predictions of dynamical facilitation theory are captured by a class of lattice models with kinetic constraints. These kinetically-constrained models (KCMs) incorporate the key phenomena of dynamical facilitation and directionality observed in atomistic systems. The one-dimensional East model is one of the simplest and most utilized of these KCMs and is described below.

East Model

The East model [21, 22] is a simple kinetically-constrained lattice model with the thermodynamics of a lattice gas [3]. While typically implemented as a one-dimensional model, higher-dimension implementations exist [23, 24, 18], and generalizations can be made to apply East model results to two and three dimensions [20].

The one-dimensional East model has N sites with labels $i = 1, 2, \ldots, N$. Each lattice site has an occupation variable $n_i \in \{0, 1\}$, where sites with $n_i = 1$ correspond to "excitations." As in atomistic systems, excitations facilitate dynamics (and therefore relaxation) in neighboring regions. The energy of the system is dependent only on the lattice occupation variables

$$\mathcal{H} = \sum_{i=1}^{N} n_i \tag{1.3}$$

and so there are no energetic interactions between sites. While the Hamiltonian is simple, the imposed dynamical constraints allow for non-trivial behavior. Dynamics at site i can only be facilitated (or destroyed) by the site to its "east," site $i-1$, and only if site $i-1$ is itself active. The rates of interconversion between active (1) and inactive (0) states are generally implemented as

$$\begin{aligned} k_{0\to1} &= e^{-\beta} n_{i-1} \\ k_{1\to0} &= n_{i-1} \end{aligned} \tag{1.4}$$

though any rates that satisfy the condition $k_{0\to1}/k_{1\to0} = e^{-\beta}$ are acceptable, where $\beta = 1/k_{\mathrm{B}}T$ is the inverse temperature of the model. Consequently, not all states are allowed to undergo a dynamical change at a time t. Dynamics is therefore facilitated and directional. Fig. 1.5 shows both the creation and destruction of excitations in a one-dimensional East model lattice.

The equilibrium concentration of excitations is

$$c = \langle n_i \rangle = \frac{1}{1 + e^{\beta}} \tag{1.5}$$

at an inverse temperature β. As in atomistic systems, the concentration of excitations decreases with decreasing temperature, and domains of inactivity therefore grow larger. An East model site is said to relax if it undergoes a transition $0 \to 1$ or $1 \to 0$, and so the structural relaxation time τ grows larger at low temperatures due to the presence of large domains of immobile sites. When structural relaxation time is plotted against inverse temperature as in Fig. 1.2, the East model also shows super-Arrhenius growth, as elaborated on in Section 1.2.2. However, it is important to establish that with its kinetic constraints, East model dynamics are facilitated at all temperatures. The East model is thus only relevant as a model of atomistic dynamics below the onset temperature.

While not utilized in the research presented in this dissertation, the Fredrickson-Andersen (FA) model [21] is closely related to the East model and shares the same Hamiltonian.

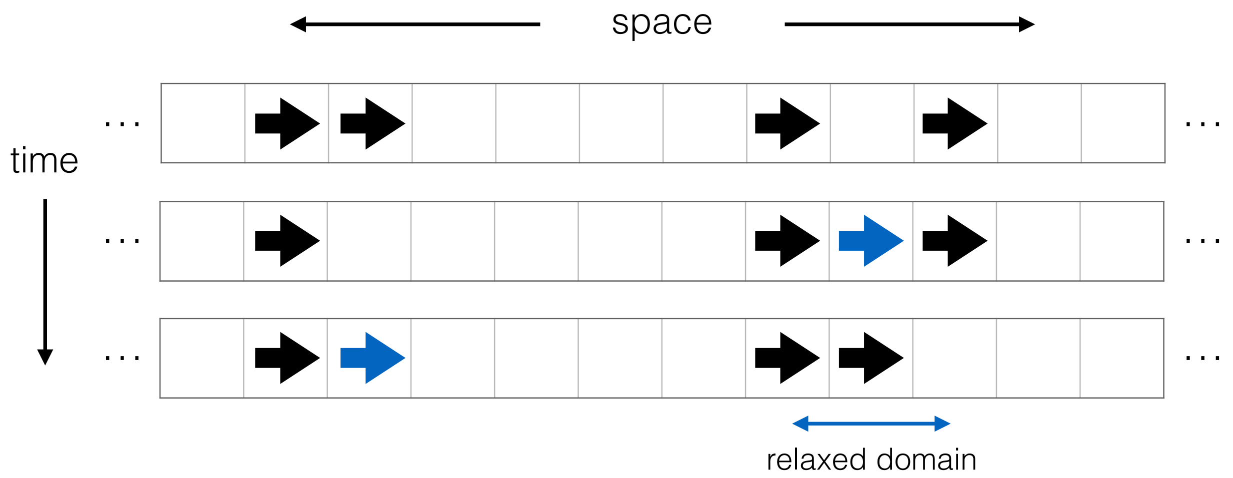

Figure 1.5: Schematic of East model dynamics. A segment of a one-dimensional East model lattice is shown at three subsequent times during a simulation. Arrows indicate sites with an excitation (i.e., "active" sites) and point in the direction of facilitation. Excitations are created and destroyed in the second and third time frames; blue arrows denote new excitations. Note that the process of creating and destroying dynamics can relax domains in the East model, as indicated.

However, the dynamical constraints are less strict. In the one-dimensional model, both excitations to the "east" and to the "west" of the site of interest may facilitate or suppress dynamics. The Arrow model [18] is a high-dimensional generalization of the one-dimensional East model (or FA model) and is the topic of Chapter 3.

1.2.2 East Model Scaling and the Parabolic Law

Kinetically constrained models, and the East model in particular, incorporate the fundamental features of glass-forming material phenomenology: facilitation and directionality. Despite their simplicity, KCMs exhibit behavior observed in glassy atomistic systems, such as decoupling of persistence and exchange times. Remarkably, KCMs also successfully predict the universal collapse of atomistic relaxation data to a super-Arrhenius form known as the parabolic law [8, 9, 10].

In the context of atomistic glass-formers, dynamical facilitation theory seeks to explain how a particle in the liquid displaces a distance a between two enduring (i.e., relatively long-lived) states. When a is on the order of a particle diameter σ, displacements that persist are indicative of an underlying excitation. Excitations consist of a handful of particles at all temperatures, and are distributed spatially as an ideal gas [10]. The equilibrium concentration of excitations for a displacement length a has a Boltzmann dependence on temperature

$$c_a \propto \exp[-J_a(1/T - 1/T_\mathrm{o})], \qquad T < T_\mathrm{o} \tag{1.6}$$

where J_a is the energy barrier to a displacement of length a. From the one-dimensional East model [23], we know that this energy scale grows logarithmically with a

$$(J_a - J_{a'})/J_{a'} = \gamma \ln(a/a') \tag{1.7}$$

where a' is a second length scale and γ is a material-dependent parameter of order unity.[1] Using transition state theory, we express the rate at which an excitation of displacement a connects to neighboring excitations as

$$1/\tau_a \approx \nu \exp[-(J_{\ell_a} - J_a)(1/T - 1/T_\mathrm{o})], \qquad T < T_\mathrm{o} \tag{1.8}$$

where the energy required to connect excitations is the activation energy of displacements. The typical distance between excitations depends on the total concentration of excitations, and so

$$\ell_a/a = (c_a a^d)^{-1/d_\mathrm{f}} \tag{1.9}$$

is the distance between neighboring pairs of excitations with displacement a. The fractal dimension d_f is a measure of the linearity of paths connecting excitations and is typically close to the physical dimension d. For the one-dimensional East model, $d_\mathrm{f} = 1$; for two- and three-dimensional atomistic systems, the fractal dimension is approximately 1.8 and 2.6, respectively [10]. Combining Eqns. 1.8, 1.9 and 1.7, we have

$$\tau_a \nu = \exp[J_a^2(\gamma/d_\mathrm{f})(1/T - 1/T_\mathrm{o})^2], \qquad T < T_\mathrm{o} \tag{1.10}$$

We set the length scale $a = \sigma$ when computing the structural relaxation time, and so define

$$J = J_\sigma \sqrt{\frac{\gamma}{d_\mathrm{f}}} \tag{1.11}$$

where J_σ is the energy scale for a displacement of length σ, a particle diameter. As the temperature is lowered and excitations grow farther apart, the energy scale to relax domains of immobility also grows. Specifically, combining Eqns. 1.10 and 1.11, we arrive at

$$\tau = \tau_\mathrm{o} \exp[J^2(1/T - 1/T_\mathrm{o})^2], \qquad T < T_\mathrm{o} \tag{1.12}$$

which gives the growth in structural relaxation time τ as a function of temperature. Eqn. 1.12 is known as the parabolic law and is the subject of Chapter 2.[2]

---

[1] The parameter γ measures the entropy of pathways between excitations.

[2] In Chapter 2, we introduce a modified form of the parabolic law, but the dominant behavior is captured by Eqn. 1.12.

Chapter 2

Corresponding States of Glass-forming Materials

2.1 The Parabolic Law

While all glass-forming materials exhibit a drastic slowing of dynamics below their melting temperatures, their respective material properties can differ greatly. Despite this diversity, the temperature-dependent transport properties of glass-forming materials can be neatly collapsed using the parabolic form

$$\log\left(\frac{\tau}{\tau_{\mathrm{o}}}\right) = J^2\left(\frac{1}{T} - \frac{1}{T_{\mathrm{o}}}\right)^2 \tag{2.1}$$

for temperatures $T < T_{\mathrm{o}}$, where T_{o} is the material-specific onset temperature for glassy dynamics [8, 9]. The parameter J sets the energy scale for excitations of correlated dynamics, and τ_{o} is the structural relaxation time at the onset temperature T_{o}. The onset temperature is typically commensurate with the melting temperature T_{m} and marks a crossover from Arrhenius liquid dynamics to the hierarchical super-Arrhenius dynamics characteristic of fragile glass-formers. There exists a separate crossover temperature $T_{\mathrm{x}} < T_{\mathrm{o}}$. Below T_{x}, dynamic constraints of glassiness can be avoided at a constant energy cost E_{x}, yielding a structural relaxation time

$$\tau = \tau_{\mathrm{x}} \exp\left(\frac{E_{\mathrm{x}}}{T}\right) \tag{2.2}$$

where τ_{x} is the relaxation time at T_{x} [1]. In this chapter, we consider temperatures $T > T_{\mathrm{x}}$ unless explicitly noted.

Eqn. 2.1—the "parabolic law"—is used to fit temperature-dependent transport properties, specifically viscosity η and structural relaxation time τ. These quantities are proportional

$$\eta = G^{\infty}\tau \tag{2.3}$$

where G^{∞} is the instantaneous shear modulus, which varies little with temperature [25]. This relationship allows us to simply replace τ and τ_{o} in Eqn. 2.1 with η and η_{o} when working with viscosity measurements. In addition to viscosities and relaxation times, diffusion measurements are also frequently used to monitor the slowdown of dynamics and are related to viscosity measurements via the Stokes-Einstein relation. This relationship is known to break down at low temperatures, however, and a fractional version of the Stokes-Einstein relation is used in its place [26, 13, 27]. Treatment of diffusivity data and conversion between diffusivities and viscosities is discussed later in this chapter.

A recent modification of the parabolic law as expressed in Eqn. 2.1 is the explicit consideration of an Arrhenius contribution to supercooled liquid dynamics. Arrhenius relaxation characteristic of temperatures $T > T_{\mathrm{o}}$ can be thought of in terms of a mean-field (MF) picture. Excitations facilitating motion are present throughout the system, and thus regions of the system do not wait long to relax. Below T_{o}, however, the dynamics becomes hierarchical such that correlated, cooperative dynamics is necessary for relaxation. This low-temperature mechanism is fundamentally different from the MF picture, and relaxation is dominated by the super-Arrhenius term. With this in mind, we alternatively express the parabolic law as

$$\begin{aligned} \log \tau_{\mathrm{MF}} &= E\left(\frac{1}{T} - \frac{1}{T_{\mathrm{o}}}\right) + \log \tau_{\mathrm{o}}, \qquad && T > T_{\mathrm{o}} \\ \log\left(\frac{\tau}{\tau_{\mathrm{MF}}}\right) &= J^2\left(\frac{1}{T} - \frac{1}{T_{\mathrm{o}}}\right)^2, \qquad && T_{\mathrm{x}} < T < T_{\mathrm{o}} \end{aligned} \tag{2.4}$$

where E is the activation energy for Arrhenius dynamics, and the remaining parameters assume the same meaning as in Eqn. 2.1. The Arrhenius term is typically far outweighed by the super-Arrhenius dynamics at supercooled temperatures, but we include it nonetheless.

For convenience, we refer to temperatures $T > T_{\mathrm{o}}$ as the "high-temperature" or "linear" regime, and to temperatures $T_{\mathrm{x}} < T < T_{\mathrm{o}}$ as the "low-temperature" or "parabolic" regime.[1] Whereas fitting datasets to Eqn. 2.1 requires only temperature points below the onset of glassy dynamics, fitting to Eqn. 2.4 requires data at temperatures in both the linear and parabolic regimes.

2.2 Fitting Procedure

In this section, we detail the procedure used to fit Eqn. 2.4 to experimental and numerical datasets. Note that the fitting procedure outlined below closely resembles the method described in Refs. [8, 9]. However, additional steps are necessary when considering temperatures both above and below the onset of glassy dynamics and are included here. The steps used to fit datasets with sufficient data both above and below the onset are as follows:

---

[1] Note that temperatures $T < T_{\mathrm{x}}$ also constitute an Arrhenius, "linear" regime. To avoid confusion, we refer to these temperatures explicitly as the low-temperature Arrhenius regime.

1. Visually inspect $\log\tau$ vs. $1/T$ and identify the general linear and parabolic regimes, thereby obtaining an approximate location of the onset separating the two.
2. Fit the high temperature data to the linear equation $\log\tau_{\mathrm{MF}} = E/T + b$, where b is the y-intercept. Starting at the highest temperatures, gradually add points until the values of E and b appear to have converged.
3. With E and b set, fit the low temperature data to $\log\tau = J^2(1/T - 1/T_{\mathrm{o}})^2 + \log\tau_{\mathrm{MF}}$. Starting at the lowest temperatures, gradually add points until the values of J and T_{o} appear to have converged.
4. For some datasets, following steps 1-3 will result in a value of T_{o} that doesn't properly separate the points used in the linear fit from the points used in the parabolic fit. In this case, repeat steps 1-3, adjusting the number of points included in the linear and parabolic fits, until T_{o} lies between these two sets of points.
5. Once we have values for J, T_{o}, E, and b, the value of $\log\tau_{\mathrm{o}} = E/T_{\mathrm{o}} + b$ is easily obtained.

Fig. 2.1 illustrates the series of steps to fit the linear and parabolic regimes of boron oxide (B_2O_3) data [7].

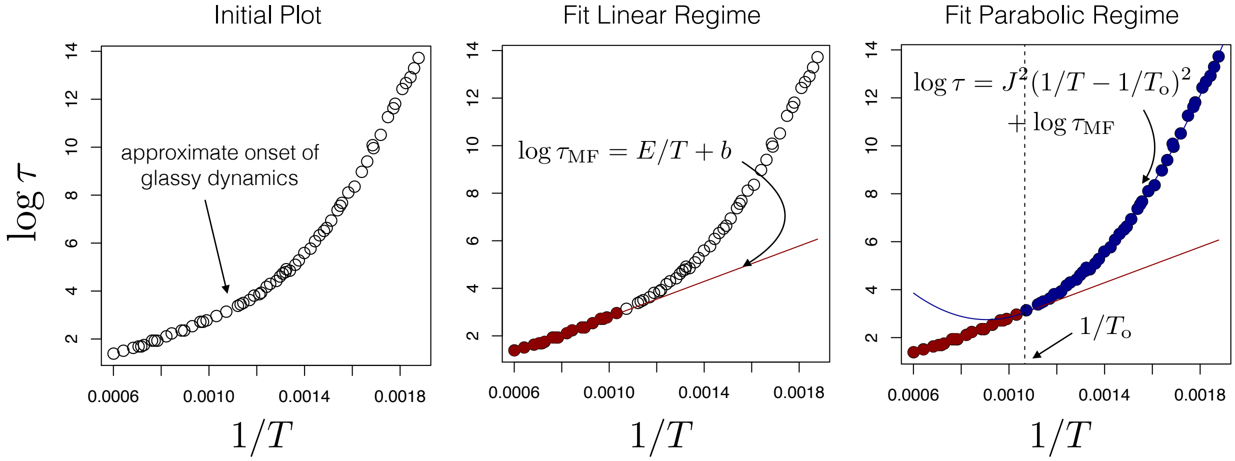

Figure 2.1: Fit to Eqn. 2.4 illustrated for boron oxide (B_2O_3) data. In the first panel, the logarithm of the relaxation time $\log\tau$ is plotted over the full temperature range so that the approximate onset of glassy dynamics can be determined. This is Step 1 of the fitting procedure. In the middle panel, the high-temperature ($T > T_{\mathrm{o}}$) regime is fit to a linear equation, as detailed in Step 2. The third panel shows the fit to the parabolic regime with the linear fit fixed; this is Step 3 of the fitting procedure. The vertical dashed line indicates the value of $1/T_{\mathrm{o}}$ determined by the fit, which separates the subsets of data points included in the Arrhenius and super-Arrhenius fits.

For some datasets, it is difficult to reach convergence with all parameter values, particularly when there are few data points available in one or both temperature regimes. The

Arrhenius contribution to the low-temperature fit tends to improve the fit at intermediate temperatures $T \approx T_\mathrm{o}$, allowing all temperature points in the dataset to be included in either the linear or the parabolic fit. We find that there is typically a single fit (and therefore, set of parabolic law parameters) where all data points are utilized and T_o lies between the points included in the linear fit and those in the parabolic fit. Even if visual inspection of parameter values for convergence is inconclusive, this single fit is taken to be the ideal fit to the available data. If more than one fit exists that satisfies the necessary conditions, the fit that minimizes the standard deviations to the linear and quadratic forms (Σ_L and Σ_Q in Tables 2.1 and 2.2) is chosen.

A feature that distinguishes the fitting procedure presented here from that utilized by Elmatad et al. is the use of only two free fit parameters in the parabolic regime. In Refs. [8, 9], only the super-Arrhenius regime ($T_\mathrm{x} < T < T_\mathrm{o}$) is considered, for which there are three fit parameters: T_o, J, and τ_o. Here, using Eqn. 2.4, the Arrhenius regime ($T > T_\mathrm{o}$) is fit first with two free parameters: E and b. With E and b fixed, the super-Arrhenius regime is then fit to obtain T_o and J. There are two free parameters for each temperature regime, as opposed to three free parameters for a fit to Eqn. 2.1. However, using Eqn. 2.4 requires sufficient data at temperatures both above and below the onset of glassy dynamics. In some cases, high temperature data is unavailable and so Eqn. 2.1 must be used.

2.3 Collapse of Liquid Relaxation Data

In the following sections, we demonstrate a universal collapse to the parabolic law (Eqn. 2.4) for both experimental and numerical liquid datasets. Values of the onset temperature T_o, the energy scale J, the relaxation time at the onset τ_o, and the Arrhenius energy barrier E resulting from these fits are included in accompanying tables. In general, the parameter values obtained from fitting with Eqn. 2.4 are commensurate with parameter values obtained with Eqn. 2.1 [8, 9] for the same material. However, there are some differences, which will be discussed in the following sections. It is important to specify that all fits to Eqn. 2.4 in the following sections use base 10 logarithms; the choice of base does not change T_o but does affect the values obtained for J, E, and $\log \tau_\mathrm{o}$.

2.3.1 Experimental Data

Fig. 2.2 shows a universal collapse of 13 experimental liquid datasets to Eqn. 2.4. The corresponding fit parameters are shown in Table 2.1.[2]

With the exception of methanol and toluene, all of the datasets featured in Fig. 2.2 and Table 2.1 were also studied by Elmatad et al. [8]. However, a significant number of the datasets included in Ref. [8] cannot be studied here because they include only temperature points below the onset temperature. For datasets with temperatures both above and below

---

[2] Datasets that are also featured in Refs. [8, 9] have the same labels here for ease of comparison. For instance, salol is labeled “Sal-1” here even though we only consider one salol dataset.

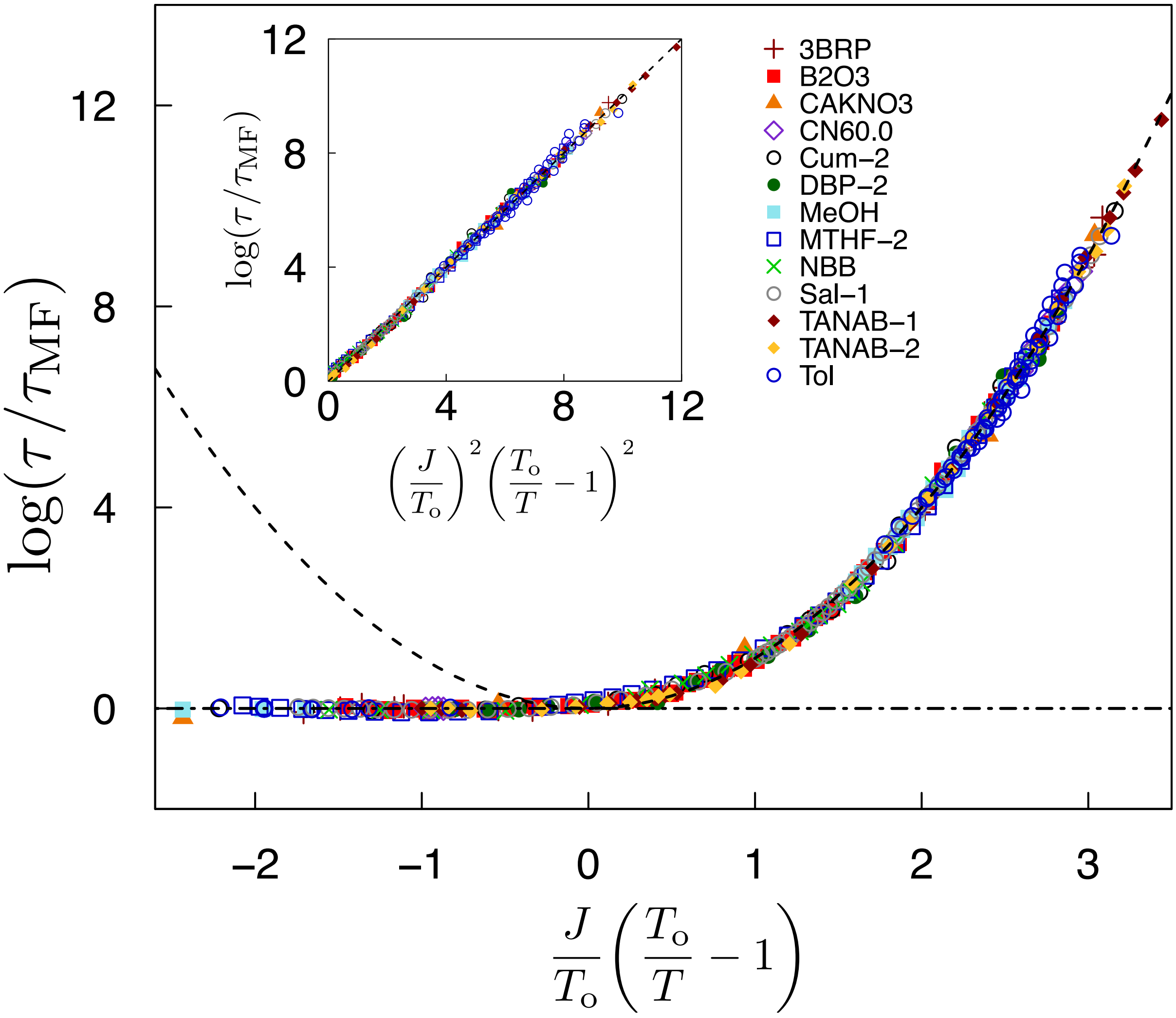

Figure 2.2: Collapse to a parabolic form of the structural relaxation times, τ, and viscosities, η, as functions of temperature T for fragile glass-forming liquids. Parameters T_o, J, and E are listed in Table 2.1. The inset shows data for temperatures $T < T_o$ graphed as a function of the square of the collapse variable. The key lists the 14 liquid data sets considered in the graphs. The meaning of each acronym is given in Table 2.1.

system[a]	full name	T_o/K[b]	J/T_o[c]	E/T_o[d]	$\log_{10}\tau_\mathrm{o}/\mathrm{s}$[e]	$\log_{10}\eta_\mathrm{o}/\mathrm{P}$[f]	$\sum_\mathrm{L}$[g]	$\sum_\mathrm{Q}$[h]	T_m/K[i]	T_g/K[j]	range/K[k]
3BRP [28]	3-bromopentane	180	4.5	3.6	-9.5		0.046	0.13	147	108	107 – 289
B2O3 [7]	boron oxide (B_2O_3)	937	3.7	4.0		3.0	0.042	0.1	723	544	533 – 1665
CaKNO3 [29]	$\mathrm{Ca{-}K{-}NO_3}$	432	11.3	5.4		0.4	0.23	0.35		334	341 – 668
CN60.0 [30]	soda lime silicate glass.0	1501	6.1	6.3		2.1	0.0064	0.046		1030	1012 – 1809
Cum-2 [7]	isopropylbenzene	191	6.7	3.5		-0.8	0.04	0.21	177	126	129 – 306
DBP-2 [7]	di-n-butylphthalate	285	4.7	4.4		-0.6	0.036	0.2		169	178 – 369
MeOH [31, 32, 33]	methanol	146	6.2	3.5		-0.3	0.023	0.093	176	95	100 – 328
MTHF-2 [34]	2-methyltetrahydrofuran	126	7.6	5.7	-9.4		0.069	0.14	137	90	94 – 179
NBB [7]	n-butylbenzene	202	5.3	3.9		1.3	0.059	0.15	185	128	135 – 306
Sal-1 [35]	salol	298	8.3	5.0	-8.4		0.028	0.058	315	220	218 – 382
TANAB-1 [36]	tri-α-naphtylbenzene	492	7.2	5.3		-0.8	0.029	0.081		335	332 – 584
TANAB-2 [7]	tri-α-naphtylbenzene	492	6.8	4.6		-0.6	0.034	0.1		329	333 – 588
Tol [37, 38]	toluene	183	5.1	2.6		-1.0	0.014	0.17	178	109	113 – 325

Table 2.1: Parabolic Law fits for experimental glass-formers.

[a] Numbered footnotes refer to references with numerical data. [b] T_o is the fitted onset temperature in K. [c] J is the fitted energy scale over k_B. [d] E is the fitted relaxation energy barrier over k_B. [e] τ_o is the fitted onset relaxation time in seconds. [f] η_o is the fitted onset viscosity in Poise. [g] Σ_L is the standard deviation of the linear fit given by: $\left(1/(N-n)\sum_i\left(\log_{10}\tau_{\mathrm{linFit},i}-\log_{10}\tau_{\mathrm{data},i}\right)^2\right)^{1/2}$. N is the number of fitted data points, $n = 2$ is the number of degrees of freedom. $i = \{1, N\}$ indexes the fitted points. [h] Σ_Q is the standard deviation of the quadratic form given by: $\left(1/(N-n)\sum_i\left(\log_{10}\tau_{\mathrm{quadFit},i}-\log_{10}\tau_{\mathrm{data},i}\right)^2\right)^{1/2}$. N is the number of fitted data points, $n = 2$ is the number of degrees of freedom. $i = \{1, N\}$ indexes the fitted points. [i] T_m is the melting temperature. [j] T_g is the glass transition temperature i.e., where $\eta = 10^{13}$ P or $\tau = 10^2$ s. [k] The range of temperature for data reported in K.

the onset, comparison of fit parameters in Table 2.1 with parameters listed in Ref. [8] reveals only slight differences. Fig. 2.3 shows this comparison, where we plot values of T_o and J for the "previous" ("P") fits to Eqn. 2.1 against values from the "new" ("N") fits to Eqn. 2.4. Each point corresponds to one of the 11 systems included in Ref. [8] that was fit here. Typically, including the Arrhenius term for temperatures below the onset results in a slightly lower onset temperature, while the J parameter remains largely unchanged. This is true for the majority of the datasets in Fig. 2.3. However, the data points representing J values for MTHF-2 and NBB appear to be exceptions and deviate from the dashed line representing an unchanged J value.

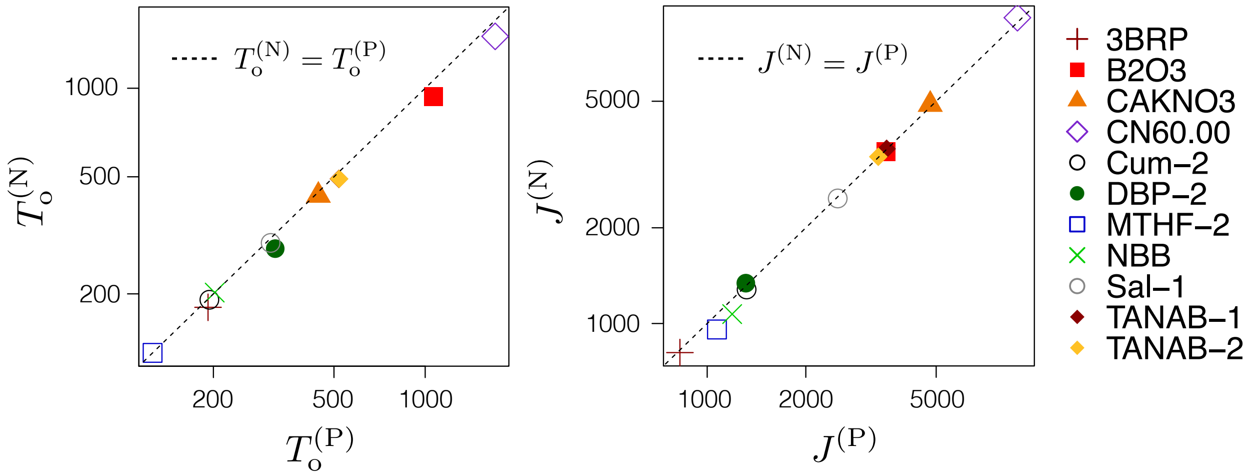

Figure 2.3: Comparison of parameter values obtained from fits to Eqn. 2.1 with values from fits to Eqn. 2.4 for experimental glass-formers. The 11 datasets that were both studied in Ref. [8] and featured in this chapter are included in the plot; the same colors and symbols are associated with each material as in Fig. 2.2. The diagonal dashed lines indicate that $T_\mathrm{o}^{(\mathrm{N})} = T_\mathrm{o}^{(\mathrm{P})}$ in the left plot and $J^{(\mathrm{N})} = J^{(\mathrm{P})}$ in the right plot. Note the logarithmic scale on both axes.

2.3.2 Numerical Data

Fig. 2.4 shows a collapse of 4 numerical datasets[3] to Eqn. 2.4. Fit parameters are listed in Table 2.2. All four numerical datasets featured here were also studied in Ref. [8]. Fig. 2.5 presents a comparison, where values of T_o and J for the "previous" ("P") fits to Eqn. 2.1 are plotted against values from the "new" ("N") fits to Eqn. 2.4. The fit to the Lennard-Jones 50:50 mixture data appears to be an outlier, as T_o actually increases and J decreases significantly from the previous fit to the new fit.

---

[3] The numerical datasets considered here were obtained from Monte Carlo and Molecular Dynamics simulations. See Appendix A for general information on these simulation methods.

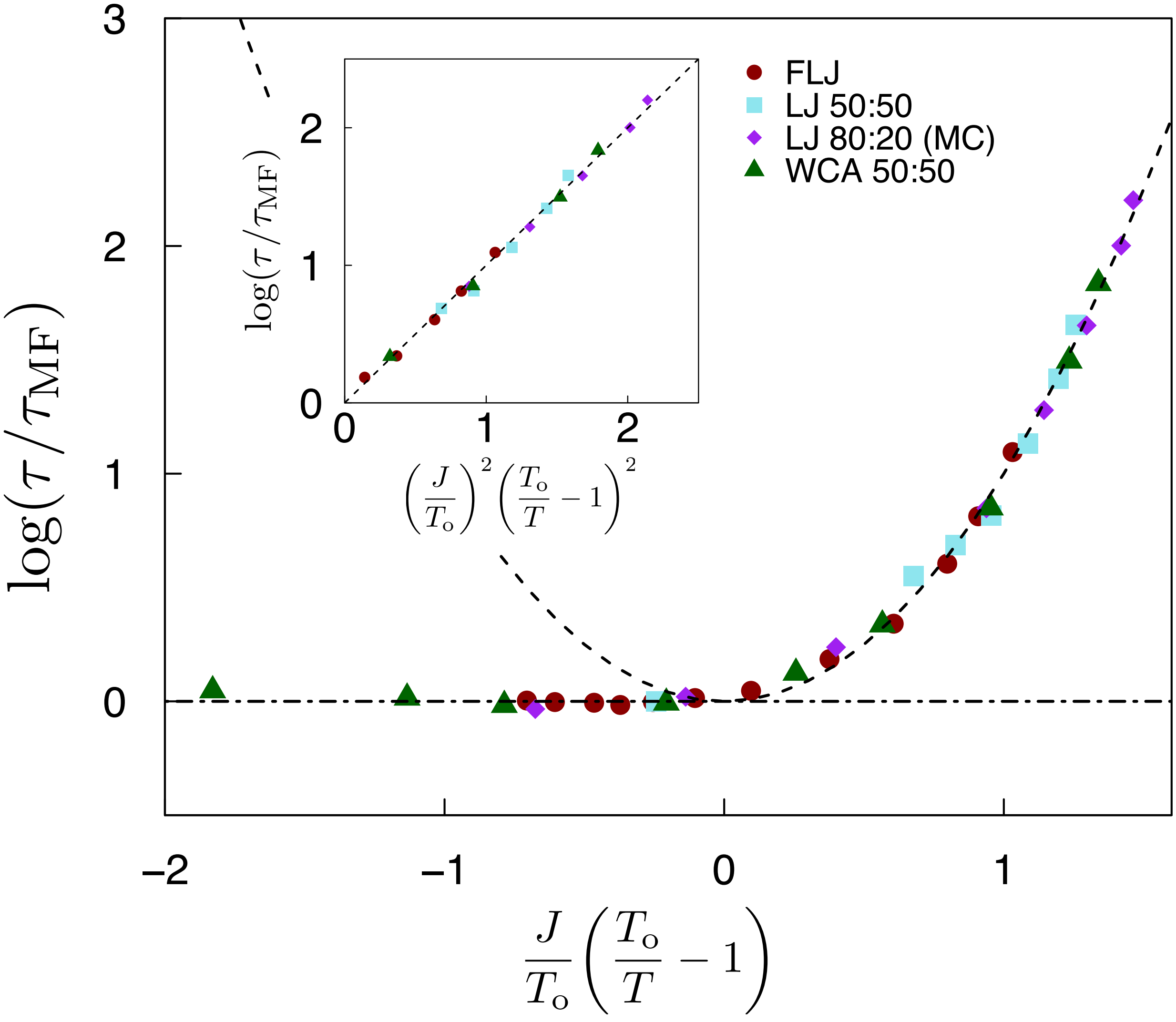

Figure 2.4: Collapse to a parabolic form of the structural relaxation times, τ, as a function of temperature T for simulations of models of fragile glass-forming liquids. Parameters T_{o}, J, and E are listed in Table 2.2. The inset shows data for temperatures $T < T_{\mathrm{o}}$ graphed as a function of the square of the collapse variable. The key lists the 4 simulation data sets considered in the graphs. The meaning of each acronym is given in Table 2.2.

system[a]	description	$T_o k_B/\epsilon$[b]	J/T_o[c]	E/T_o[d]	$\log_{10}[\tau_o/(m\sigma^2/\epsilon)^{1/2}]$[e]	$\sum_L$[f]	$\sum_Q$[g]	range (k_B/ϵ)[h]
FLJ [39]	Frustrated Lennard-Jones	0.3	1.3	2.0	1.2	0.011	0.039	0.18 – 0.8
LJ 50:50 [40]	Lennard-Jones 50:50 mixture	0.9	2.7	1.2	0.5	-	0.081	0.59 – 2
LJ 80:20 [41]	Lennard-Jones 80:20 mixture (MC)	0.7	2.3	1.7	2.7	0.041	0.056	0.43 – 2
WCA 50:50 [12]	Weeks-Chandler-Andersen 50:50 mixture	0.6	2.5	1.5	0.7	0.039	0.057	0.36 – 5

Table 2.2: Parabolic Law fits for numerical glass-formers.

[a] Numbered footnotes refer to references with numerical data. [b] T_o is the fitted onset temperature in k_B/ϵ. [c] J is the fitted energy scale over k_B. [d] E is the fitted relaxation energy barrier over k_B. [e] τ_o is the fitted onset relaxation time in $\sqrt{m\sigma^2/\epsilon}$. [f] Σ_L is the standard deviation of the linear fit given by: $\left(1/(N-n)\sum_i\left(\log_{10}\tau_{\mathrm{linFit},i}-\log_{10}\tau_{\mathrm{data},i}\right)^2\right)^{1/2}$. N is the number of fitted data points, $n=2$ is the number of degrees of freedom. $i=\{1,N\}$ indexes the fitted points. [g] Σ_Q is the standard deviation of the quadratic form given by: $\left(1/(N-n)\sum_i\left(\log_{10}\tau_{\mathrm{quadFit},i}-\log_{10}\tau_{\mathrm{data},i}\right)^2\right)^{1/2}$. N is the number of fitted data points, $n=2$ is the number of degrees of freedom. $i=\{1,N\}$ indexes the fitted points. [h] The range of temperature for data reported in units of k_B/ϵ.

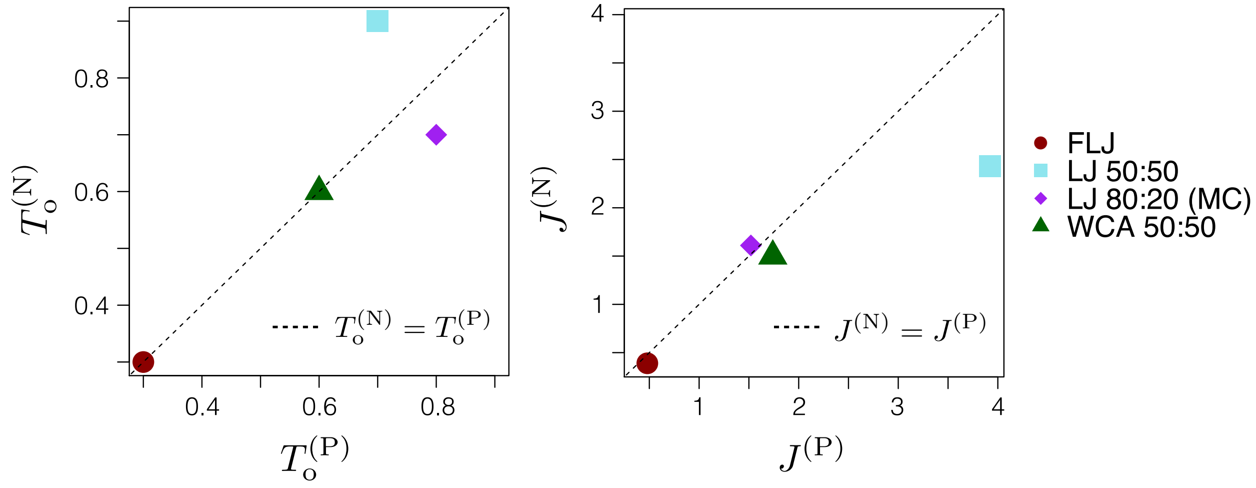

Figure 2.5: Comparison of parameter values obtained from fits to Eqn. 2.1 with values from fits to Eqn. 2.4 for numerical glass-formers. The 4 datasets that were both studied in Ref. [8] and featured in this chapter are included in the plot; the same colors and symbols are associated with each material as in Fig. 2.4. The diagonal dashed lines indicate that $T_o^{(N)} = T_o^{(P)}$ in the left plot and $J^{(N)} = J^{(P)}$ in the right plot.

2.3.3 Comment on the Crossover Regime

The inclusion of an Arrhenius contribution to the parabolic law (Eqn. 2.4) typically improves the fit to temperature points in the crossover regime from simple liquid dynamics to hierarchical glassy dynamics. However, it is clear in Fig. 2.2 that some of the the glass-forming materials studied here (e.g., MTHF-2 and NBB) deviate from the parabolic form in this moderately supercooled regime. The parabolic law assumes an abrupt crossover to hierarchical dynamics at the onset temperature, but fits for the aforementioned materials may instead be consistent with a broader crossover.

Currently, there is no theory that satisfactorily explains the physics of the onset of glassy dynamics. Such a theory would help elucidate the crossover from simple liquid dynamics to glassy dynamics, and could reveal whether certain materials are expected to have broader crossovers than others. Further study is required.

2.4 Breakdown of the Stokes-Einstein Relation

Along with measurements of viscosities and structural relaxation times, diffusion measurements quantify the drastic slowing in dynamics that occurs at supercooled temperatures. Diffusion and viscosity are related and can be easily interconverted via the Stokes-Einstein relation (SER). The methanol and toluene datasets in Fig. 2.2 and Table 2.1 were converted from diffusivities to viscosities using the SER. In this section, we begin with a general discussion of the SER and the fractional form that becomes relevant at supercooled temperatures. Finally, we detail the conversion process for methanol and toluene datasets.

The SER relates the diffusion constant D for a material to its viscosity η

$$D \propto \frac{T}{\eta^{1-\omega}} \tag{2.5}$$

at a temperature T, where $\omega = 0$ at temperatures above the onset of glassy dynamics T_o. Below T_o, when dynamics becomes correlated, this relation with $\omega = 0$ no longer holds [26, 13, 27]. The viscosity η increases faster than the self diffusion constant D decreases. At supercooled temperatures, $\omega > 0$, and we therefore refer to Eqn. 2.5 as the fractional SER. From simulation studies of high-dimensional East models [4] with probe particles to measure diffusion, we find $\omega \approx 0.17$ for $d = 3$ [42]. The switch from the SER ($\omega = 0$) to the fractional SER ($\omega > 0$) is not instantaneous at the onset temperature. Ref. [37] plots toluene diffusivities against the corresponding ratio of viscosities to temperatures in order to empirically determine the value of ω across a temperature range $113 - 325$ K. They find that $\omega \approx 0$ through the melting temperature $T_\mathrm{m} \approx T_\mathrm{o}$, but the SER breakdown does not occur until much lower temperatures are reached.

Although we include only viscosity and structural relaxation time values in Figs. 2.2 and 2.4 and Tables 2.1 and 2.2, we can also fit diffusion data to the parabolic law. We use a

---

[4] If unfamiliar with the East model, see Section 1.2.1 for a brief overview.

modified form

$$\begin{aligned}\log\left(\frac{D}{D_\mathrm{o}}\right) &= (\omega-1)\left[J^2\left(\frac{1}{T}-\frac{1}{T_\mathrm{o}}\right)^2+E\left(\frac{1}{T}-\frac{1}{T_\mathrm{o}}\right)\right], \qquad T_\mathrm{x}<T<T_\mathrm{o}\\ \log\left(\frac{D}{D_\mathrm{o}}\right) &= -E\left(\frac{1}{T}-\frac{1}{T_\mathrm{o}}\right), \qquad T>T_\mathrm{o}\end{aligned} \tag{2.6}$$

which takes into account this breakdown at supercooled temperatures. At temperatures above the onset of glassy dynamics, ω is always equal to zero and thus is not included explicitly in Eqn. 2.6. Diffusivity at temperature T and onset diffusivity are represented by D and D_o, respectively; all other parameters maintain their previous definitions.

For a small number of the systems included in Fig. 2.2 and Table 2.1, neither viscosity nor relaxation time data is available. Instead, diffusivities are provided over a range of temperatures above and below T_o. Using the SER and fractional SER, we convert these diffusivity values to viscosities.

Converting Toluene and Methanol Diffusivities to Viscosities

The toluene data from Refs. [37, 38, 43] consists of diffusivity measurements over a combined temperature range 113 − 325 K. Diffusivities at the lowest temperatures (113 − 135 K) were measured by depositing a layer of inert gas (Argon, Krypton, and Xenon) beneath an amorphous solid toluene layer at an even colder temperature [37]. As the system is warmed and the amorphous solid toluene melts into a supercooled liquid, the inert gas begins to permeate the liquid, with a desorption rate related to the toluene diffusivity. This method allows measurements at temperatures much lower than can be accessed by simply cooling liquid toluene from its melting temperature.

The onset temperature $T_\mathrm{o} = 183$ K for toluene can be determined by fitting the diffusivity data to Eqn. 2.6.[5] The temperature points over 219 − 325 K [38] are decidedly above the onset temperature for toluene, so the diffusivity values are converted to viscosities using the full form of the SER

$$D = \frac{k_\mathrm{B}T}{6\pi r\eta^{1-\omega}} \tag{2.7}$$

with $\omega = 0$. Ref. [37] provides the hydrodynamic radius of the diffusing species $r = 0.1$ nm. The low-temperature points over 113 − 135 K [37] are significantly below the onset temperature, so we convert the diffusivities to viscosities via Eqn. 2.7 with $\omega = 0.17$. Fig. 2.6 shows the toluene diffusivity data, where temperature points have been colored according to the values of ω used for their conversion to viscosities. The intermediate data, for which the appropriate value of ω is unclear, is omitted from our analysis.

We follow the same procedure when converting methanol diffusivities. The methanol data [31, 32, 33] consists of diffusivity measurements over the temperature range 100 − 328 K. Similar to the toluene measurements [37], the lowest temperature data (100 − 117 K)

---

[5] The choice of ω for a fit to Eqn. 2.6 does not affect the value for T_o.

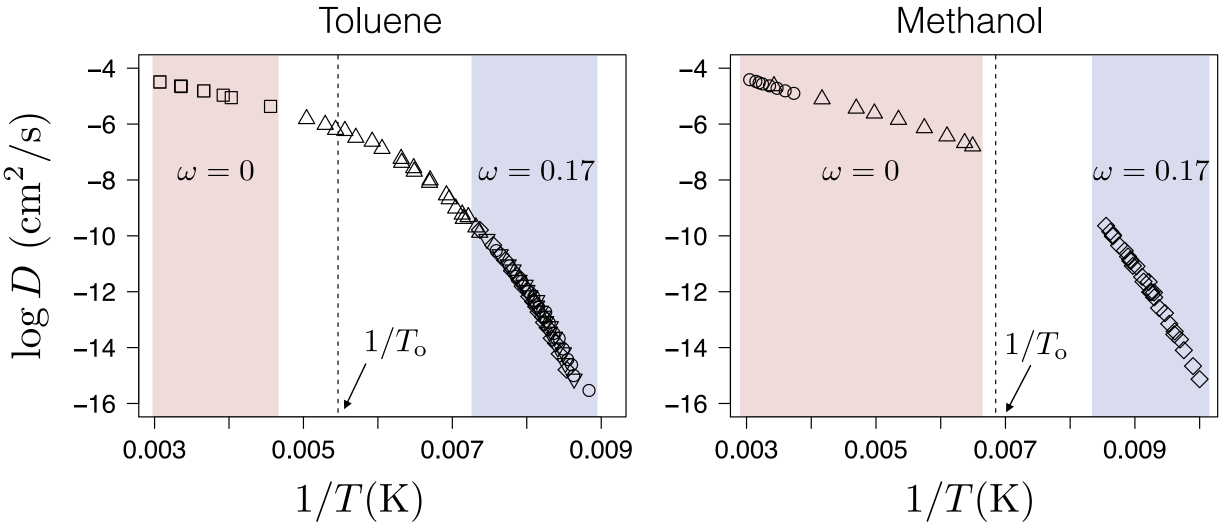

Figure 2.6: Toluene and methanol diffusivity datasets. Red shaded regions indicate high-temperature regimes where the SER with $\omega = 0$ is used to convert to the appropriate viscosity values. Blue shaded regions indicate low-temperature regimes where the fractional SER with $\omega = 0.17$ is used to convert to viscosities. Temperature points outside these shaded regions are excluded from our analysis and did not contribute to the fits reported in Fig. 2.2 and Table 2.1. Onset temperatures for toluene and methanol (183 K and 146 K, respectively) are denoted with dashed lines. For both materials, at least three datasets were combined to cover the full temperature range; these separate datasets are plotted with different symbols.

was obtained using the method of inert gas permeabilities. Fitting Eqn. 2.6 to the data yields an onset temperature $T_o = 146$ K. High temperature diffusion data $(154 - 328$ K$)$ is converted to viscosities using the SER with $\omega = 0$, and low temperature data $(100 - 117$ K$)$ is converted using the fractional SER with $\omega = 0.17$. This is illustrated in Fig. 2.6.

2.5 Challenges of Fitting Water Data

Due to a lack of low-temperature data in the literature, it is difficult to conclusively determine the value of the energy scale for hierarchical dynamics in supercooled water. As we saw in previous sections for different materials, measurements at sufficiently low temperatures—such that relaxation times or viscosities span several orders of magnitude—are essential for an accurate determination of J. It is relatively straightforward to measure transport properties for water cooled from its melting temperature of 273 K down to temperatures around 240 K. Below this temperature, liquid water is no longer stable and it becomes exceedingly difficult to avoid crystallization. However, diffusion at significantly lower temperatures has been measured by first preparing amorphous solid water at an even colder temperature and then warming it to a supercooled liquid state. Ref. [44] uses this method to measure supercooled water diffusivities at temperatures between 150 and 157 K. In this section, we present several representative supercooled water datasets available in the literature and discuss the corresponding parabolic fit parameters, elaborating on any conflicting values. We also comment on the data required to conclusively determine the value of J, the energy scale for excitations of correlated dynamics.

2.5.1 Simulated Water Models

Water has a variety of unique properties and is essential for life, making it a popular subject of study in both lab and computer experiments. A variety of simulated models have been developed to study water on a computer, each with different features and optimized for specific purposes. Simulated models can allow us to explore a larger range of temperatures for supercooled water, where crystallization can be more easily avoided. For close agreement between the behavior of transport properties in experimental and simulated water, fits to the parabolic law should yield roughly the same parameters.

Ref. [45] fits structural relaxation time data from a variety of simulated (explicit) water models—including TIP5P, mW, and ST2—to the parabolic law.[6] Overall, these models show marked agreement of fit parameters. For each of the five models, $T_o \approx 0.99 T_{\max}$, where $T_{\max}$ is the temperature of maximum density for the specific model,[7] and $J/T_o \approx 7.5$. If experimental water and simulated water indeed exhibit similar transport property behavior with decreasing temperature, these are the values we hope to confirm for liquid water.

---

[6] Ref [45] fits data to the parabolic law as expressed in Eqn. 2.1.

[7] Each model has a unique temperature scale, so we normalize temperatures by the temperature at which the specific model is at its maximum density. For experimental water, this value is 277 K.

2.5.2 Experimental Water

Here, we evaluate several existing water datasets in the literature and present fits to the parabolic law with corresponding parameter values. For all fits, we fix the onset temperature $T_\mathrm{o} = 271$ K, which we know to be the approximate true value. We are primarily interested in determining the value of J. Note that for some fits in this section, we revert to the version of the parabolic law in Eqn. 2.1 for diffusivities

$$\log\left(\frac{D}{D_\mathrm{o}}\right) = (\omega - 1)J^2\left(\frac{1}{T} - \frac{1}{T_\mathrm{o}}\right)^2, \quad T < T_\mathrm{o} \tag{2.8}$$

if the dataset considered does not include suitable high-temperature data for determination of the Arrhenius activation energy E. Because we are only interested in determining whether data is consistent with a specific parabolic form, any small changes in J/T_o between fits to Eqn. 2.1 and Eqn. 2.4 will not affect our conclusions.

1. Reported parabolic law parameter values in Ref. [45] (Limmer et al.)

We begin with the parabolic law fit parameters for experimental water presented in Ref. [45]. The reported values are $T_\mathrm{o} = 0.98T_\mathrm{max} = 271$ K and $J/T_\mathrm{o} = 7.4$, which are in very good agreement with the simulated water models. For experimental water, we know $T_\mathrm{max} = 277$ K, so $T_\mathrm{o} = 271$ K; this onset temperature is commensurate with the melting temperature, as expected. These values are supported by a combination of data sources. Viscosity data is reported in Ref. [46, 6] for a range of moderately supercooled temperatures $244 - 265$ K. Fig. 2.7 shows a plot of this dataset alongside the parabolic form with $T_\mathrm{o} = 271$ K and $J/T_\mathrm{o} = 7.4$. We see that the dataset is in good agreement with this choice in J, and thus with the simulation values. However, the temperature range is narrow (all data is in the "moderately supercooled" temperature regime) and viscosities span only an order of magnitude, and so our fit to the parabolic law is less than satisfying. We show Eqn. 2.8 with $\omega = 0$ because the data is close enough to the onset temperature that we would expect this form to fit better than the $\omega = 0.17$ parabola.[8]

Experimental confined water data reported in Ref. [47] also supports the value $J/T_\mathrm{o} = 7.4$. Water confined in nanopores can avoid crystallization at lower temperatures with help from the disorder introduced by the nanopore walls, which destabilizes ordered water structure. Measurements of the energy scale J are reported for a range of cavity radii [48, 49, 50, 51, 52]; extrapolating the value of J to infinite nanopore radius gives a value $J/T_\mathrm{o} = 7.4$.

2. Diffusion data in Ref. [44] (Smith et al.)

While the viscosity data in Fig. 2.7 only includes measurements in the moderately supercooled regime, Ref. [44] reports diffusion data at highly supercooled temperatures $150 - 157$

---

[8] This is analogous to our previous conversion of moderately supercooled methanol and toluene diffusivities to viscosities using the SER (Eqn. 2.5 with $\omega = 0$).

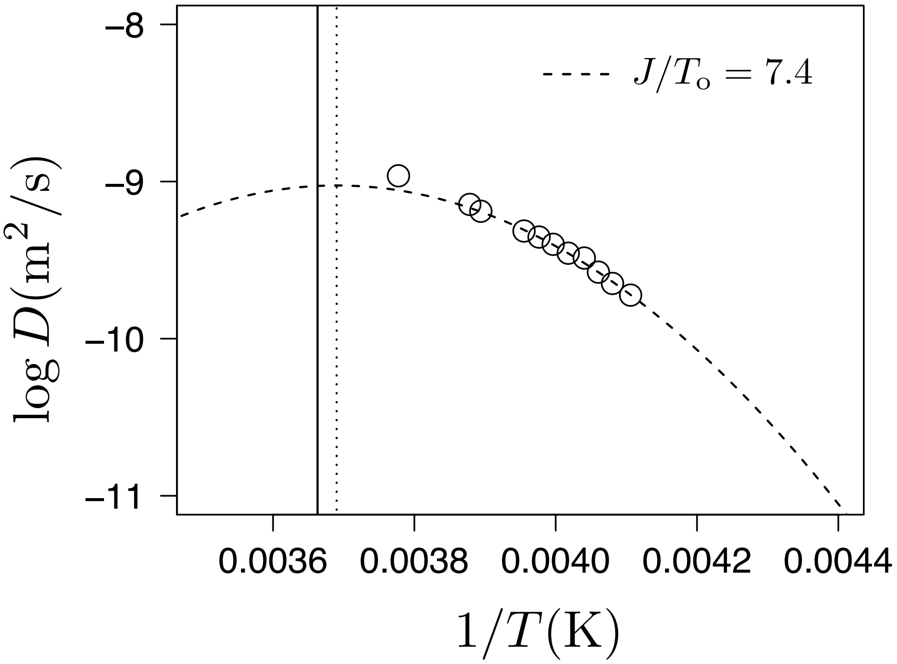

Figure 2.7: Water diffusivities at moderately supercooled temperatures from Ref. [6]. The dashed parabola corresponds to the parabolic law (Eqn. 2.8 with $\omega = 0$) with $J/T_o = 7.4$ and $T_o = 271$ K is fixed. The solid vertical line indicates $1/T_m$, where $T_m = 273$ K. The dashed vertical line marks $1/T_o$.

K. To obtain measurements at such low temperatures, Smith et al. deposit water isotopes $H_2\,^{16}O$ and $H_2\,^{18}O$ on a cold substrate (< 140 K) to form an amorphous solid phase, which is metastable with respect to crystalline ice. When the substrate is warmed above 150 K, the amorphous solid melts to form a supercooled liquid, and diffusivities can be determined by studying isotope mixing. The sample crystallizes above 157 K, so Ref. [44] provides diffusivities over the temperature range $150 - 157$ K, in addition to high-temperature and moderately supercooled data (243 – 498 K) [53, 54, 55] measured by cooling liquid water. Fig. 2.8 shows supercooled water and ice diffusion data [56, 57] featured in Ref. [44], along with a parabolic fit to Eqn. 2.6 with $T_o = 271$ K fixed. We use $\omega = 0$ for the high temperature and moderately supercooled data and use $\omega = 0.17$ only for the data at temperatures $150 - 157$ K. This fit yields $J/T_o = 4.1$, significantly smaller than the ratio of 7.4 reported for simulated water systems. The parabolic form with $T_o = 271$ K and $J/T_o = 7.4$ is also included in Fig. 2.8 to illustrate that the lowest temperature data is clearly inconsistent with the higher value of J.

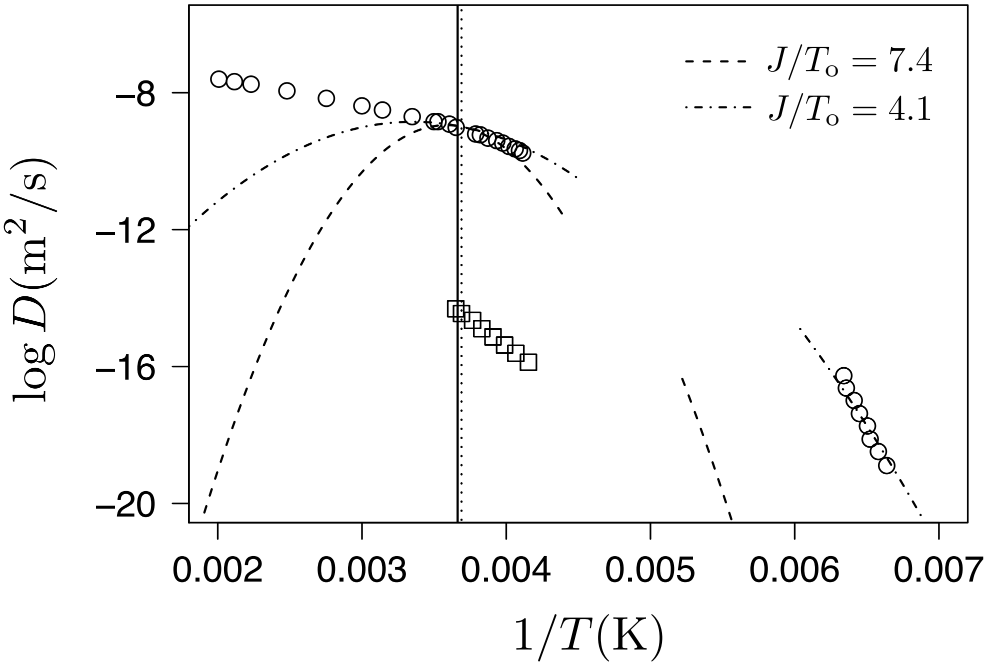

Figure 2.8: Water diffusivities at deeply supercooled temperatures from Ref. [44]. Parabolas corresponding to two distinct parameterizations of the parabolic law (Eqn. 2.8 with $\omega = 0$ for high-temperature and moderately supercooled data [53, 54, 55] and $\omega = 0.17$ for deeply supercooled data) are given by dashed lines; in both cases $T_o = 271$ K is fixed. The parabola pieces corresponding to $J/T_o = 4.1$ is a fit to the supercooled liquid data; the parabola pieces with $J/T_o = 7.4$ is shown to demonstrate incompatibility with the values reported for simulated water models. Ice diffusion data (open squares) [56, 57] are shown for reference.

3. Diffusion data in Ref. [58] (Dehaoui et al.)

Ref. [58] reports water diffusivities measured over temperatures 239 − 293 K.[9] All temperatures in this range are decidedly in the high temperature and moderately supercooled regimes. Fig. 2.9 shows a best fit to Eqn. 2.6 with $\omega = 0$, $T_\mathrm{o} = 271$ K fixed, and $J/T_\mathrm{o} = 4.4$. For reference, we also include the parabola with $J/T_\mathrm{o} = 7.4$ to demonstrate the incompatibility of the data with the higher value of J.

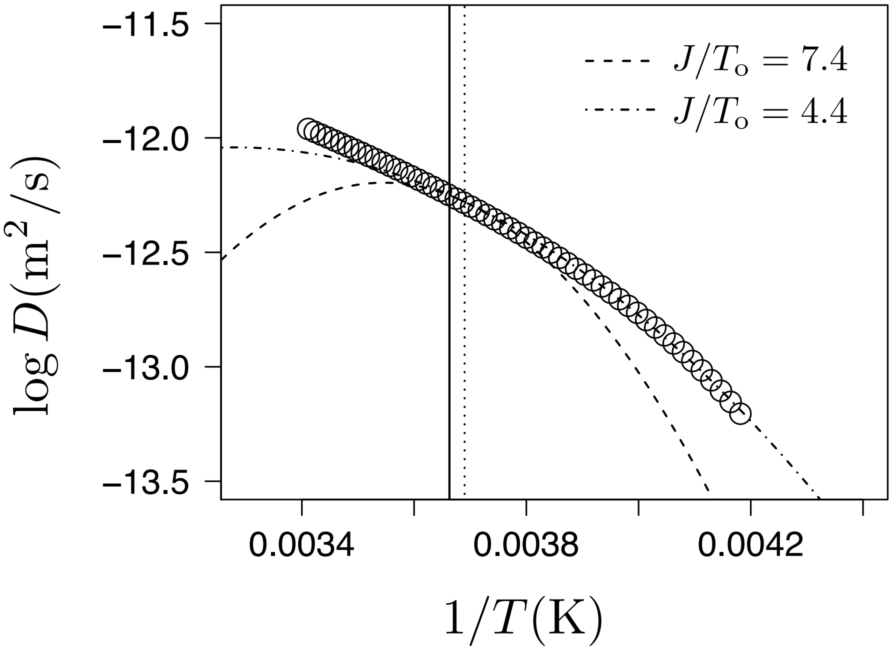

Figure 2.9: Water diffusivities at moderately supercooled temperatures from Ref. [58]. The dashed parabola corresponds to the parabolic law (Eqn. 2.6 with $\omega = 0$) with $J/T_\mathrm{o} = 7.4$ and $T_\mathrm{o} = 271$ K is fixed. The solid vertical line indicates $1/T_\mathrm{m}$, where $T_\mathrm{m} = 273$ K. The dashed vertical line indicates $1/T_\mathrm{o}$. The fit parameters $E/T_\mathrm{o} = 4.3$ and $\log D_\mathrm{o} = -12.3$; for clarity, we have not plotted the high-temperature Arrhenius fit.

The authors of Ref. [58] present their own fit to the parabolic law. However, they obtain a clearly incorrect value of 305 K for the onset temperature, which corresponds to water well above the melting temperature. It should be noted that Ref. [58] fit viscosity data using an incorrect version of the parabolic law,[10] though this has no effect on the resulting values of T_o and J/T_o.

---

[9] Although Ref. [58] reports viscosity data in the corresponding Supplementary Information, it is clear from the methods section that diffusivity is the measured quantity. Diffusivities were converted to viscosities using the proportionality $\eta(T) = \eta(T_0)[T/T_0][D(T_0)/D(T)]$ with reference temperature $T_0 = 293.15$ K. Viscosities in the SI were back-calculated to diffusivities for inclusion in this chapter.

[10] The form of the parabolic law used to fit water viscosity data, as written in Ref. [58], is equivalent to the expression in Eqn. 2.4 without the $-E/T_\mathrm{o}$ term for temperatures both above and below the onset.

4. Diffusion data in Ref. [59] (Price et al.)

Ref. [59] reports water diffusivities measured over temperatures 238 – 298 K. All temperatures in this range are decidedly in the high temperature and moderately supercooled regimes. Fig. 2.10 shows a best fit to Eqn. 2.6 with $\omega = 0$, $T_o = 271$ K fixed, and $J/T_o = 4.0$. For reference, we also include the parabola with $J/T_o = 7.4$ to demonstrate the incompatibility of the data with the higher value of J.

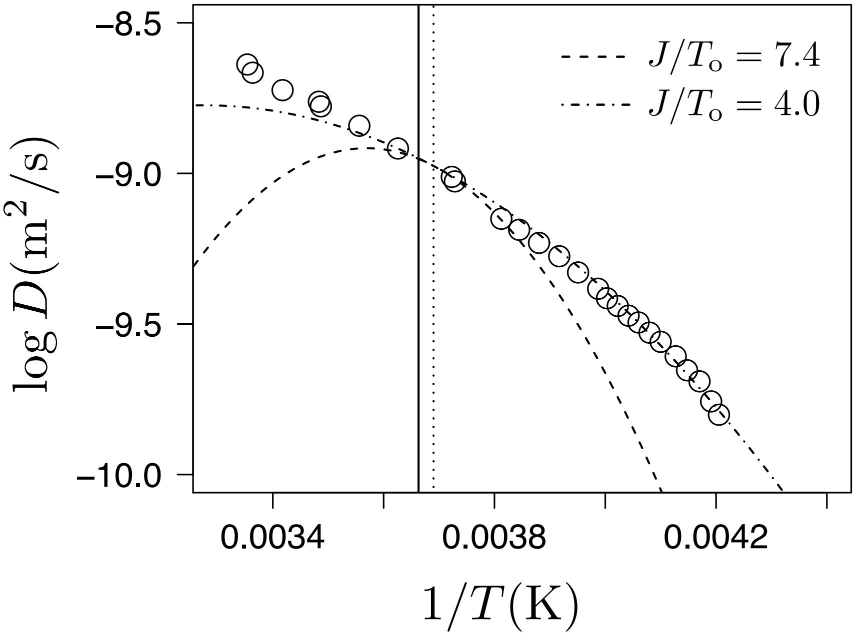

Figure 2.10: Water diffusivities at moderately supercooled temperatures from Ref. [59]. The dashed parabola corresponds to the parabolic law (Eqn. 2.6 with $\omega = 0$) with $J/T_o = 7.4$ and $T_o = 271$ K is fixed. A second dashed parabola corresponds to a fit to the parabolic law (Eqn. 2.6 with $\omega = 0$) with $J/T_o = 4.0$; $T_o = 271$ K is fixed. The solid vertical line indicates $1/T_m$, where $T_m = 273$ K. The dashed vertical line indicates $1/T_o$. The fit parameters $E/T_o = 3.6$ and $\log D_o = -9.0$. For clarity, we have not plotted the high-temperature Arrhenius fit.

2.5.3 Concluding Remarks

In the previous sections, we attempt to determine the true value of the hierarchical energy scale J for experimental supercooled water. Fits to data from Ref. [58], Ref. [59], and Ref. [46, 6] lead to two distinct values, $J/T_o \approx 4.2$ and $J/T_o = 7.4$, respectively. However, fitting only moderately supercooled data cannot reliably determine the curvature of the parabolic form; data at much colder temperatures is required. To our knowledge, Ref. [44] is the only source of data at sufficiently low temperatures ($T \ll 240$ K). Analysis of this dataset suggests $J/T_o = 4.1$, a ratio significantly lower than that reported for simulated water models. The current lack of data at temperatures below 240 K makes it impossible to verify this value. There is a clear need for more experimental data at deeply supercooled temperatures if we hope to confidently determine J/T_o for supercooled water.

2.6 Fitting High-Dimensional Hard Sphere Models

In previous sections, we detail fits to the parabolic law with data from experimental liquids and from numerical liquid models, specifically Lennard-Jones mixtures. These numerical models balance accuracy of intermolecular potentials with computational efficiency, and include both repulsive and attractive terms to describe interactions between particles. Hard sphere (HS) liquids provide a further simplification of the actual intermolecular forces experienced by including only a rigid repulsive term. The intermolecular pair potential between spheres i and j at coordinates $\mathbf{r}_i$ and $\mathbf{r}_j$, respectively, is simply

$$U(|\mathbf{r}_i - \mathbf{r}_j|) = \begin{cases} \infty, & |\mathbf{r}_i - \mathbf{r}_j| < \sigma \\ 0, & |\mathbf{r}_i - \mathbf{r}_j| \geq \sigma \end{cases} \tag{2.9}$$

where σ is the particle diameter. Like Lennard-Jones mixtures, systems of hard spheres can exhibit sluggish dynamics and crystallize under certain conditions. When the goal is to study dynamics under glassy conditions, binary mixtures of hard spheres with diameters σ_1, σ_2, where $\sigma_1 > \sigma_2$, are typically required to avoid crystallization. An alternative approach to preventing crystallization at high packing fractions is to modify the potential in Eqn. 2.9 such that a disorder incompatible with ordered structure is introduced. In this section, we fit relaxation time measurements from simulations of such a modified HS model in dimensions $d = 3 - 6$ [60] to the parabolic law. We then comment on the relationship between liquid dimension and the packing fraction at the onset of glassy dynamics, and we explore how this onset is related to a presumed dynamical transition in mode-coupling theory.

2.6.1 The Mari-Kurchan Model

The Mari-Kurchan (MK) model [61] is a modified HS model that greatly simplifies the liquid structure in high dimensions. The MK hamiltonian introduces an additional quenched random shift to the intermolecular potential in Eqn. 2.9

$$\mathcal{H} = \sum_{i<j}^{N} U(|\mathbf{r}_i - \mathbf{r}_j + \mathbf{\Lambda}_{ij}|) \tag{2.10}$$

where $\mathbf{\Lambda}_{ij}$ is a random uniformly distributed vector over the volume of the system. (In the standard HS model, $\mathbf{\Lambda}_{ij} = 0$.) Incorporating the random shift eliminates higher-order correlations in the liquid, particularly important for high d. For example, two particles can each be close to a third particle, but it is unlikely they are also close to each other because their distance is shifted by $\mathbf{\Lambda}$, which is of the order of the system size.[11]

Several features of the MK model distinguish it from the standard HS model and make it particularly well-suited for studying high-dimensional supercooled liquids. The most significant implication for studying glassy dynamics is that the crystal phase is suppressed by the quenched disorder introduced by random shifts. A second consequence of using the MK model is related to the equation of state. Whereas the equation of state for a standard HS system must be approximated [62], the absence of higher-order correlations in the MK model allows for a simple expression that holds for all d [60]. This simplification aids us in our fit of the data to the parabolic law, as described in the following section. The pressure equation of state is

$$\frac{\beta P}{\rho} = 1 + B_2 \rho \tag{2.11}$$

where $B_2 = V_d(1)\sigma^d/2$ is the second virial coefficient for d-dimensional hard spheres, $V_d(R)$ is the volume of a d-dimensional ball of radius R, ρ is the number density, and the inverse temperature β is set to unity [60]. The packing fraction φ is expressed as

$$\varphi = \rho V_d(\sigma/2) \tag{2.12}$$

where $\sigma = 1$ is the particle diameter.

2.6.2 Collapse to the Parabolic Law

In order to fit relaxation data to the parabolic law, we must first specify the conjugate field that controls the mean value of the relevant local order parameter field. For experimental and numerical systems considered in Sections 2.3 and 2.5, we utilize inverse temperature $1/T$, which is conjugate to the energy density order parameter. For a hard sphere system, and the MK model in particular, the relevant order parameter is particle density. The variable conjugate to the particle density is P/T. The use of the MK model allows us to determine the value of P/T as a function of system density via an equation of state. From Eqn. 2.11, we have

$$\frac{P}{T} = \rho \left(1 + \frac{\rho V_d(1)\sigma^d}{2} \right) \tag{2.13}$$

For each dimension, we plot the values of $\log \tau_\alpha$ reported in Ref. [60] as a function of P/T and fit to Eqn. 2.4, where the ratio P/T takes the place of $1/T$. Fig. 2.11 shows the collapse of all dimensions to the parabolic law, with the corresponding fit parameters listed in Table 2.3. We see that the onset value of $(P/T)_\mathrm{o}$ (and therefore the value of the onset packing fraction) decreases with increasing dimension. This agrees with the results of a previous study [63], which found that the packing fraction required to freeze hard spheres

---

[11] The addition of the random shift affects the degree to which dynamics is facilitated in the MK model. While in a standard HS system a displaced particle makes room for a neighboring particle to displace, this may not happen in the MK model due to allowed overlapping of particles.

is lower than that required to freeze hard discs. Recall that the freezing point is generally commensurate with the onset of glassy dynamics.

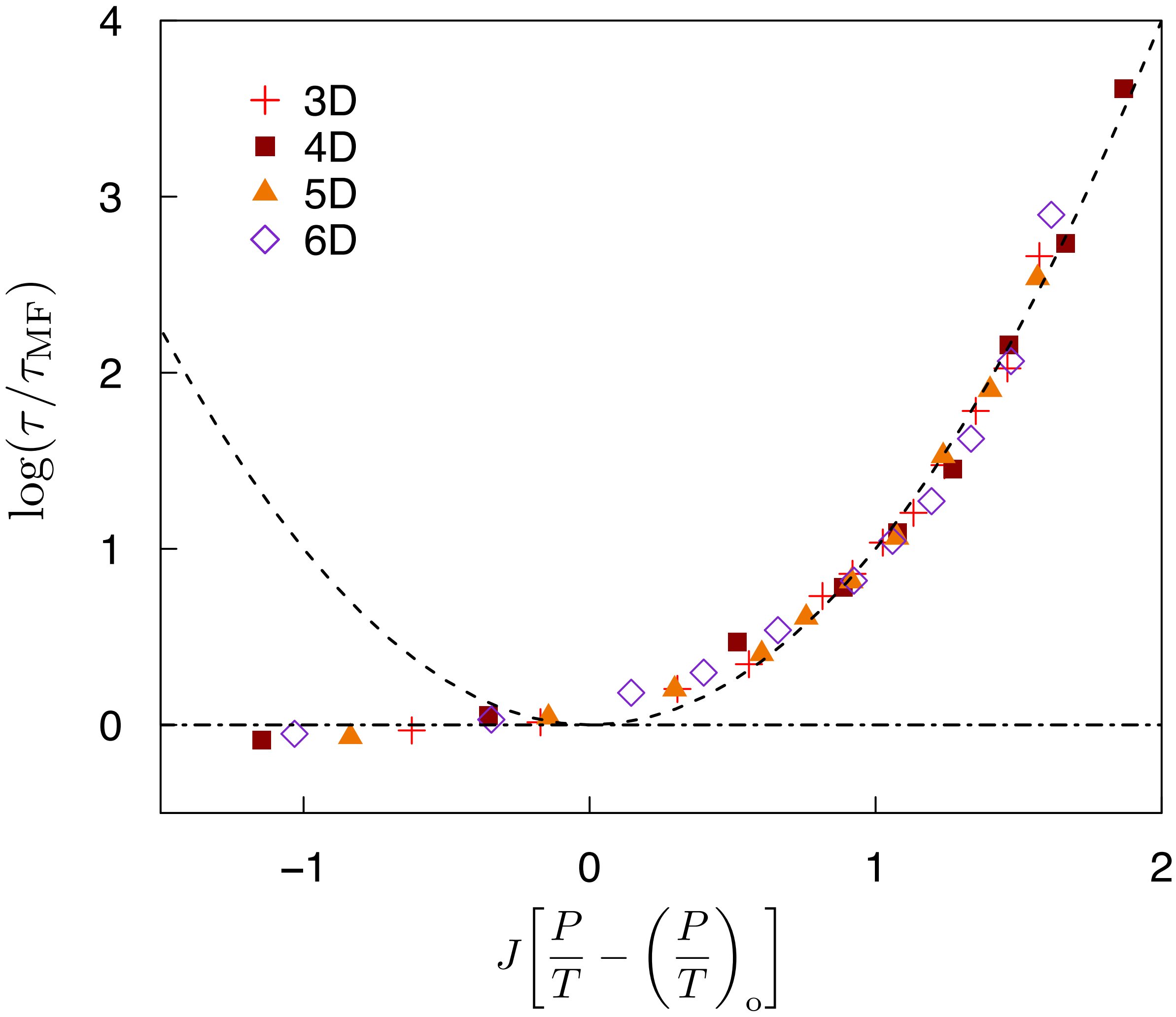

Figure 2.11: Collapse to a parabolic form of the structural relaxation times τ as a function of P/T for Mari-Kurchan systems in dimensions 3-6 [60]. Parameters $(P/T)_{\mathrm{o}}$, J, and E from Eqn. 2.4 are listed in Table 2.3. The legend gives the dimension of each dataset.

2.6.3 Comparison with East Model Results

Here we elaborate on what seems to be an inconsistency between the MK model results shown in Fig. 2.11 and Table 2.3 and high-dimensional East model results reported in Ref. [42]. In the MK model, the onset packing fraction clearly decreases with increasing liquid dimension. However, the East model must become progressively colder—analogous to a more densely packed hard sphere liquid—in higher dimensions in order to reach the onset of glassy

dimension[a]	$(T/P)_{\text{o}}$[b]	$J(P/T)_{\text{o}}$[c]	$E(P/T)_{\text{o}}$[d]	$\log_{10}\tau_{\text{o}}$[e]	$\sum_{\text{L}}$[f]	$\sum_{\text{Q}}$[g]	range[h]
3	0.048	3.923	0.172	3.489	0.03832	0.09867	0.034-0.065
4	0.032	4.756	0.091	3.334	0.1066	0.13394	0.023-0.067
5	0.022	5.033	0.068	3.466	0.08392	0.07664	0.016-0.037
6	0.015	5.053	0.044	3.389	0.06231	0.17202	0.011-0.025

Table 2.3: Parabolic Law fits for the Mari-Kurchan model in dimensions 3-6.

[a]Data for all dimensions is found in Ref. [60]. [b]$(T/P)_{\text{o}}$ is the fitted onset. [c]J is the fitted energy scale. [d]E is the fitted relaxation energy barrier. [e]τ_{o} is the fitted onset relaxation time. [f]Σ_{L} is the standard deviation of the linear fit given by: $\left(1/(N-n)\sum_i \left(\log_{10}\tau_{\text{linFit},i} - \log_{10}\tau_{\text{data},i}\right)^2\right)^{1/2}$. N is the number of fitted data points, $n = 2$ is the number of degrees of freedom. $i = \{1, N\}$ indexes the fitted points. [g]Σ_{Q} is the standard deviation of the quadratic form given by: $\left(1/(N-n)\sum_i \left(\log_{10}\tau_{\text{quadFit},i} - \log_{10}\tau_{\text{data},i}\right)^2\right)^{1/2}$. N is the number of fitted data points, $n = 2$ is the number of degrees of freedom. $i = \{1, N\}$ indexes the fitted points. [h]The range of values of T/P for data.

dynamics.[12] This East model trend can be understood by recognizing that with increasing dimension, there are more relaxation pathways by which one spin can relax another.

In order to understand the inconsistency between MK model and East model relaxation trends, we consider the the effects of fluctuations and local rigidity in glass-forming materials. In low dimensions, liquid dynamics are dominated by fluctuations, and liquid configurations are locally rigid. As the dimension increases, liquid dynamics becomes increasingly mean-field in nature, while local configurations become more rigid. The MK model experiences both fluctuations and rigidity, and so the increase in dimension causes a decrease in the packing fraction for the onset of collective behavior. In the East model, dynamics is fluctuation-dominated in all finite dimensions [42], but there is no concept of local structural rigidity. The increase in relaxation pathways between spins in high dimensions is responsible for the decrease in onset temperature. While qualitative, this argument provides an intuitive explanation for the seemingly contradictory results.

---

[12] Hierarchical, facilitated dynamics are present in the East model at all temperatures, and so there is no true onset of glassy dynamics. The onset temperature T^* considered in Ref. [42] is the temperature at which the energy scale for hierarchical dynamics in the East model crosses some finite threshold. Specifically, T^* is defined as the temperature at which the slope of the relaxation time τ versus inverse temperature $1/T$ is equal to 2. This metric is a reasonable way to compare East model dynamics to that of real glasses.

Chapter 3

Supercooled Liquid Dynamics on a Lattice

3.1 Introduction

Studies of atomistic systems reveal that dynamics in jammed-up materials proceeds via a complex and highly correlated mechanism [10]. Central to this mechanism are the dynamical principles of facilitation and directionality. A mobile particle, displacing in a specific direction, can facilitate the dynamics of its neighbors in the same general direction. However, simulations of atomistic systems are computationally expensive and can be unfeasible for large system sizes or very low temperatures. A model with additional coarse-graining could provide a solution to these bottlenecks and therefore contribute to computational studies of glassy physics. Kinetically constrained lattice models such as the East and FA models [21, 22] have been used successfully to model the fundamental mechanisms of motion in supercooled systems and understand the calorimetric glass transition [20]. These models are simple and relatively fast to simulate, but their original formulations are in one dimension. A more natural lattice model to represent a supercooled atomistic system should be isotropic in two and three dimensions, while still including the essential ingredients of facilitated dynamics and directionality of particle flow.

In this chapter, we characterize the dynamical behavior of the Arrow model, a kinetically constrained lattice model for atomistic glass formers that incorporates both dynamical facilitation and directionality of particle flow [18]. The Arrow model can be thought of as a higher-dimensional generalization of the East model with the advantage of being isotropic for all parameter choices. We begin by introducing the dynamical rules associated with the Arrow model, which enforce the facilitated and directional dynamics. We then explore a variety of dynamical features, comparing them to what is observed in atomistic systems. Finally, we present a mapping between the Arrow model and atomistic models that allows us to parameterize the Arrow model to describe a specific experimental supercooled liquid.

3.2 The Arrow Model

In dimension d, the Arrow model consists of a d-dimensional lattice with N lattice sites labeled $i = 1, 2, \ldots, N$, each in one of two dynamical states, $n_i = 0$ or 1. The former represents an inactive state, and the latter an active or "excited" state. Excited states have a direction of facilitation associated with them, a d-dimensional unit vector $\mathbf{v}_i$ pointing along the diagonal of the lattice site. The number of possible directions for a given arrow is $g = 2^d$, and site i can therefore exist in one of $g + 1$ states which we denote as $\mathbf{n}_i = n_i \mathbf{v}_i$.

The Arrow model has the Hamiltonian

$$\mathcal{H} = J_0 \sum_{i=1}^{N} n_i \tag{3.1}$$

where J_0 is the fundamental energy scale for creating a new excitation (we set $J_0 = 1$ unless otherwise noted). There are no energetic interactions between neighboring sites, and thermodynamics is trivial. However, like the East and FA models, the Arrow model incorporates dynamical facilitation rules that result in nontrivial dynamics. An active site can facilitate (or eliminate) activity in one of d neighboring sites located in its specific direction of facilitation. A site must be dynamically facilitated in order to undergo a change in state. The schematic in Figure 3.1 illustrates these dynamical rules.

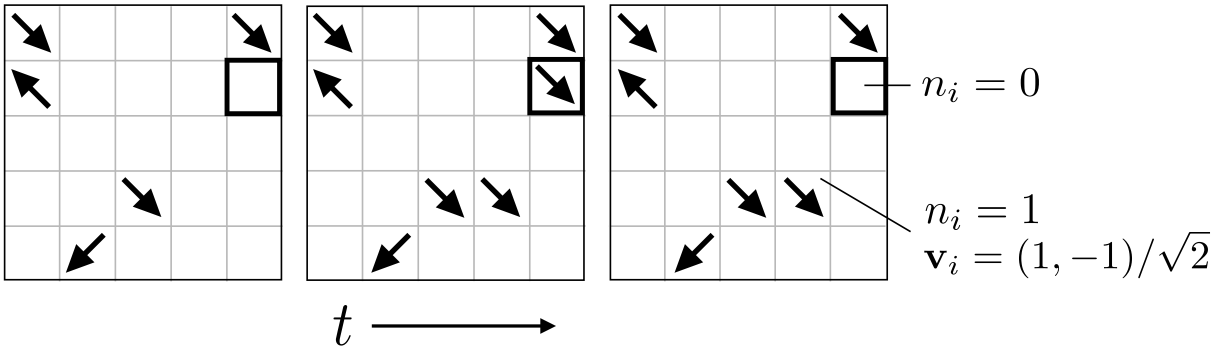

Figure 3.1: Schematic of $f = 0$ Arrow model dynamics in two dimensions. An inactive site i has $n_i = 0$, and an excited state has $n_i = 1$ with an associated direction of facilitation described by $\mathbf{v}_i$, a unit vector in one of $g = 2^d$ directions. This direction of facilitation is denoted with an arrow. The three frames are subsequent points in time, and a site at which dynamical changes take place is outlined in black. The outlined site in the leftmost frame is facilitated by the site above it and becomes activated (i.e., an arrow is created) in the center frame. In the final frame, the arrow in the outlined site has been destroyed; this dynamical change is once again facilitated by the site directly above it. Note that the facilitation direction of the created and then destroyed excitation matches the facilitation direction of the facilitating site.

The facilitated nature of this model is implemented by setting the rates between active and inactive states as

$$\mathbf{n}_i = 0 \quad \underset{C_i[\mathbf{v}_i](1-c)}{\overset{C_i[\mathbf{v}_i]c/g}{\rightleftharpoons}} \quad \mathbf{n}_i = \mathbf{v}_i \tag{3.2}$$

where c is the equilibrium concentration of excitations and

$$C_i[\mathbf{v}_i] = f\left[1 - \prod_{\langle j,i\rangle}(1 - \delta_{\sqrt{d}(i-j)\cdot\mathbf{n}_j,1})\right] + (1-f)\left[1 - \prod_{k=1}^{d}(1 - \delta_{\mathbf{n}_{i-\sqrt{d}\mathbf{v}_k},\mathbf{v}_i})\right] \tag{3.3}$$

enforces the kinetic constraints and depends only on the states of site i's neighbors. Nearest neighbor sites are denoted by $\langle j, i\rangle$. The Arrow model incorporates a parameter $f \in [0, 1]$ analogous to the directional persistence of atoms or molecules in a real system. The value of f sets the probability $\mathrm{P}(f)$ that a newly created arrow will have the same direction as its facilitating arrow

$$\mathrm{P}(f) = [1 + f(g-1)]^{-1}. \tag{3.4}$$

In the $f = 1$ limit, this probability is equal to $1/g$, and excitations of any direction can be created or destroyed if facilitated by a neighbor. In the $f = 0$ limit, this probability is equal to 1, and excitations can be created or destroyed only if their direction of facilitation matches that of its facilitating neighbor.[1] In this chapter we consider the $f = 0$ limit of the model, unless stated otherwise.

The temperature of the lattice sets the equilibrium concentration of excitations

$$c = \langle n_i\rangle = \frac{g}{g + e^{\beta J_0}} \tag{3.5}$$

where $\beta = 1/T$ is the inverse temperature. The concentration in Eqn. 3.5 includes excitations in all directions. As in a real liquid, the system is isotropic, and $\langle \mathbf{v}_i\rangle = 0$. Distinct sites on the lattice are uncorrelated, and so the equilibrium distribution for the field of vectors is

$$\mathrm{P}(\{\mathbf{n}_i\}) = \prod_{i=1}^{N} \rho(\mathbf{n}_i) \tag{3.6}$$

where

$$\rho(\mathbf{n}) \equiv g^{-n}(1-c)^{1-n}c^{n}. \tag{3.7}$$

Dynamical events within the Arrow model are defined below.

Mathematical Description of Dynamical Events

For mathematical convenience, we express Arrow model dynamics in terms of "kinks," or dynamical events, occurring at specific lattice sites. A kink corresponds to the creation or destruction of an excitation at a lattice site. We define a kink operator

$$\kappa_i(t) = |n_i(t) - n_i(t - \delta t)| \tag{3.8}$$

---

[1] Arrow model relaxation in the $f = 0$ ($f = 1$) limit is analogous to that of a "fragile" ("strong") glass-former.

for a lattice site i at time t, where δt is an elementary time step. As defined in the previous section, $n_i(t)$ is an arrow occupation variable denoting the activity of the lattice site; note that direction of facilitation has no effect on the kink operator. When $\kappa_i(t) = 1$, we say that a kink has occurred at site i at time t.

3.3 Super-Arrhenius Relaxation

We say that a lattice site has "relaxed" if a kink occurred during a time interval of interest. On average, lattice sites behave identically, so we can express an overall structural relaxation time for the system. We use Metropolis Monte Carlo simulations to compute the structural relaxation time, as well as all subsequent Arrow model calculations.[2]

The relaxation time τ of the Arrow model at a specific temperature is defined as the $1/e$ decay of the persistence function, a correlation function expressing the probability that a site has not had a kink up until that time [64, 65, 66]. To define the persistence function, we first measure the binary immobility value for lattice site i in terms of the kink operator in Eqn. 3.8

$$p_i(t) = \prod_{t'=0}^{t} [1 - \kappa_i(t')] \tag{3.9}$$

which is 0 if site i has undergone at least one dynamical event before time t and is 1 otherwise. When $p_i(t)$ is summed over all N lattice sites, we obtain a function

$$P(t) = \sum_{i=1}^{N} p_i(t) \tag{3.10}$$

that decays from N to zero over time as more sites undergo dynamical events. The decay of the time average of $P(t)$

$$\langle P(t) \rangle = \frac{1}{t_{\text{obs}}} \sum_{t'=0}^{t_{\text{obs}}} P(t') \tag{3.11}$$

is shown in Fig. 3.2a, along with an illustration of how the relaxation time τ is defined. Fig. 3.2b shows the resulting values of the relaxation time τ for $d = 2$ and $d = 3$ as a function of inverse temperature $\beta = 1/T$. We see that the relaxation behavior of the $f = 0$ Arrow model is super-Arrhenius, as is the case for atomistic glass-formers at temperatures below the onset of glassy dynamics T_{o} and above the crossover to Arrhenius relaxation T_{x}.

The specific definition of τ detailed above has historically been used for similar kinetically-constrained models like the East and FA models. However, there is nothing inherently special about the choice of $1/e$ as the decay threshold. The important feature to consider when choosing the threshold is how the shape of the persistence function changes with temperature in the neighborhood of that threshold value. For example, Fig. 3.8a (to be discussed in a

---

[2] See Appendix A for a general discussion of Monte Carlo methods.

later section) shows persistence functions for the $d = 3$ Arrow model for the temperature range $T = 0.19 - 0.38$. As the temperature decreases, the short-time shape of the curves (on a logarithmic scale) changes due to evolving relaxation mechanisms. However, these changes in form do not affect how the persistence functions decay around $\langle P(t) \rangle / N = 1/e \approx 0.37$, and $1/e$ is therefore a suitable choice for our decay threshold.

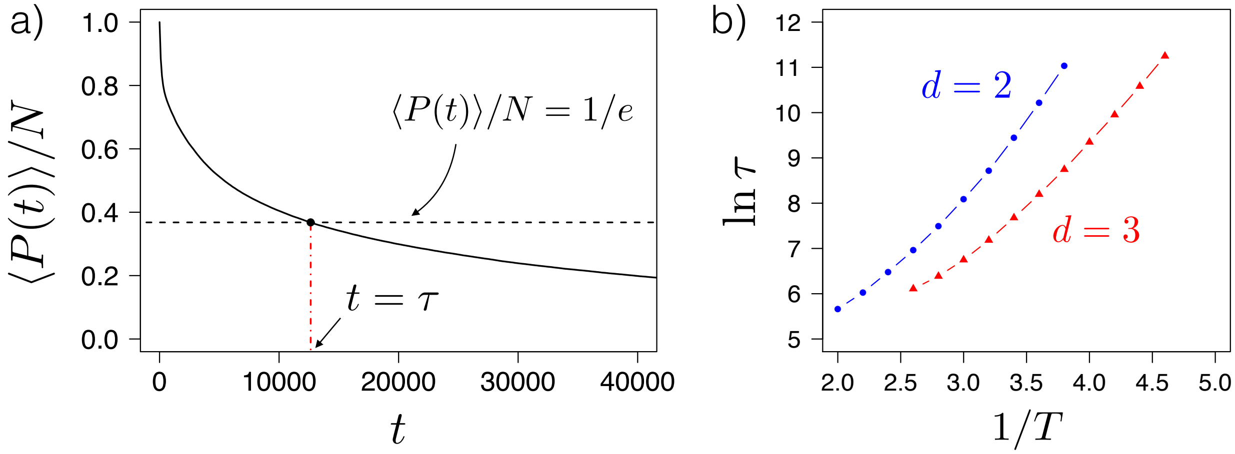

Figure 3.2: Super-Arrhenius relaxation in the $f = 0$ Arrow model. (a) Decay of the time-averaged persistence function $\langle P(t) \rangle$ over time as more sites have a chance to relax. We define the relaxation time τ, denoted by the intersection of the red dashed line with the time axis, as the time at which the persistence function decays to $1/e$ (black dashed line). (b) Relaxation times plotted as a function of inverse temperature for the $d = 2$ and $d = 3$ Arrow model. All times are expressed in units of Monte Carlo sweeps.

3.4 Dynamical Heterogeneity

At temperatures above the onset of glassy dynamics, essentially all regions of the liquid are mobile. At supercooled temperatures, however, the mechanism for liquid relaxation changes such that dynamical facilitation is critical for particle motion [19]. Dynamical facilitation refers to local rearrangements of liquid structure that make motion possible nearby in space. As a result, distinct regions of mobility and immobility emerge within the same liquid system; this is known as “dynamical heterogeneity” [65].

As the temperature is lowered further below the onset, heterogeneous dynamics persists, but the concentration of excitations (i.e., mobile regions) decreases. The typical distance between any two regions of mobility in the system grows as a result. The nature of dynamical heterogeneity is well-characterized in atomistic liquids [10]. Here, we explore heterogeneous dynamics in the Arrow model to see if the same complex dynamical behavior is present in a much simpler lattice model.

3.4.1 Exchange and Persistence Times

In a supercooled liquid exhibiting heterogeneous dynamics, both mobile and immobile regions exist within the system. A particle in a mobile region is likely to experience a period of high mobility, characterized by many dynamical transitions. This mobile period may be followed and preceded by relatively long periods of immobility if the particle is no longer found in a mobile region of the liquid. In this sense, dynamical events are correlated in time, and a time series of kinks for a particular particle will appear clustered.

Exchange and persistence times [14, 12] allow us to quantify the observed clustering of kinks for a particle or lattice site in a glassy system. Here, we express these quantities mathematically in terms of dynamical events at lattice sites. A persistence time t_p is the waiting time until the next dynamical event at the same lattice site, and an exchange time t_x is the time between two consecutive events. Persistence and exchange functions can be expressed in terms of the kink operator defined in Eqn. 3.8, where

$$P_i(t', t) = \kappa_i(t' + t) \prod_{t''=t'+\delta t}^{t'+t-\delta t} [1 - \kappa_i(t'')] \tag{3.12}$$

indicates a persistence time $t_\mathrm{p} = t$ given a time origin t', and

$$X_i(t', t) = \kappa_i(t')\kappa_i(t' + t) \prod_{t''=t'+\delta t}^{t'+t-\delta t} [1 - \kappa_i(t'')] \tag{3.13}$$

gives an exchange time $t_\mathrm{x} = t$ for a time origin t'. The difference between these expressions is that the persistence function considers all possible time origins, whereas the exchange function only considers starting times coinciding with dynamical events. In general, decoupling of persistence and exchange distributions is characteristic of heterogeneous dynamics. Decoupling implies that if a dynamical event occurs at a lattice site, more are likely to follow. In the case of uncorrelated dynamics, the distributions will be very similar to each other and appear to be drawn from a Poisson process.

Fig. 5.6 shows distributions of exchange and persistence times for the two-dimensional Arrow model at temperatures $T = 1.0$, $T = 0.5$, and $T = 0.33$. At low temperatures, the exchange and distributions exhibit a multi-peak structure. This phenomenon is described for the East and FA models by Jung et al. [14] and is shown to arise from the presence of multiple relaxation processes.

3.4.2 Enduring Transitions

A particle in a supercooled liquid may undergo displacements over a range of distances. The majority of displacements are small and quickly reversed, however, resulting only in fleeting changes in the underlying configuration of excitations. Displacements that result in a lasting reorganization are more rare, particularly in very cold systems, and are said to

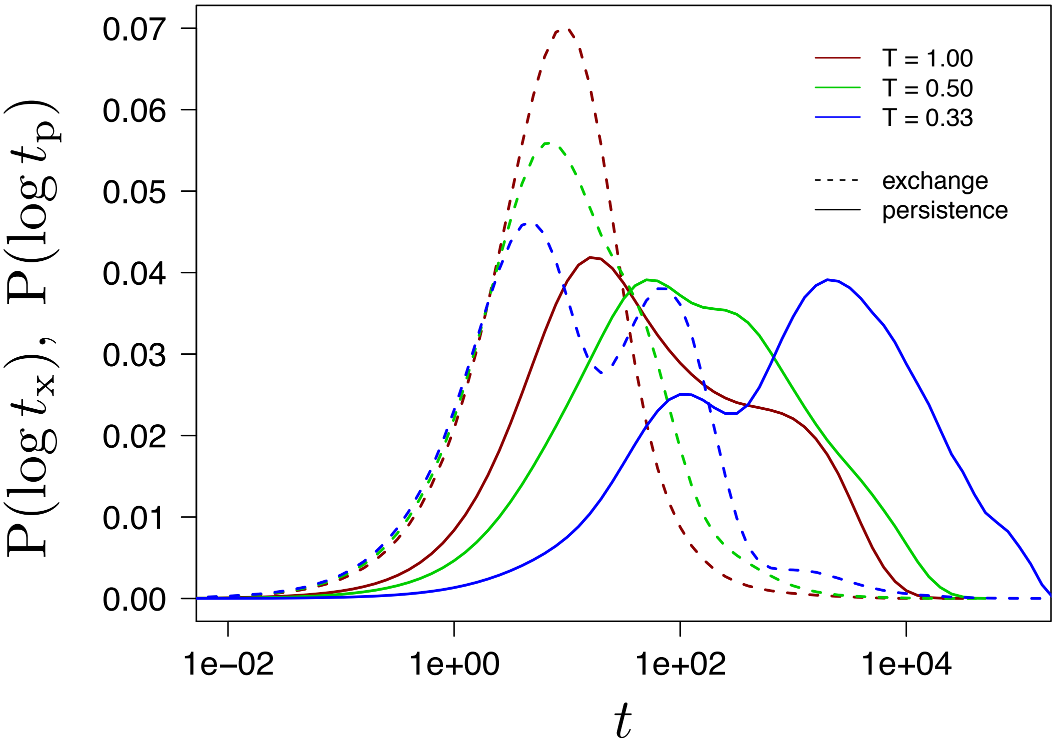

Figure 3.3: Distributions of exchange (dashed) and persistence (solid) times for the Arrow model in two dimensions for temperatures $T = 1.0$ (red), $T = 0.5$ (green), and $T = 0.33$ (blue). A system size of $N = 10,000$ was used for this calculation. Exchange and persistence times are expressed in units of Monte Carlo sweeps.

"endure." These enduring transitions are the significant dynamical events we wish to study. In atomistic systems, we therefore coarse-grain away displacements that do not endure for a chosen sojourn time t_s in order to resolve heterogeneous dynamics [10]. Similarly, for the Arrow model and other lattice models, the majority of kinks at a lattice site are short-lived, and do not contribute to the overall reorganization of the lattice. We consider the enduring kinks to resolve significant dynamics [67].

To find the enduring kinks in an Arrow model trajectory, we follow the procedure in Ref. [67] for identifying enduring kinks in the East model. For a site i, we can define a set of enduring kinks occurring at times t that endure for a sojourn time t_s. Enduring kinks must satisfy the following three conditions:

- Kinks must occur at both the beginning and the end of the enduring kink event.
- No kinks may be present within a time t_s of either the beginning or end of the enduring kink event.
- The initial state (before the enduring kink event) and the final state (after the enduring kink event) of the lattice site in question must be opposite, i.e. go from "excited" to "unexcited," or vice-versa.

This final condition requires that there be an odd number of kinks contained in any enduring kink event. When the number of such kinks is greater than one, the midpoint of the enduring kink event is chosen as the enduring kink time. Fig. 3.4 illustrates these rules for a time trajectory of a single lattice site.

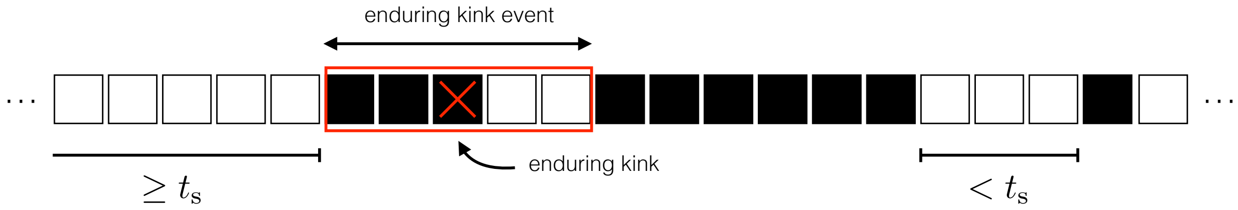

Figure 3.4: Enduring kink schematic for a single Arrow model lattice site. The series of squares represent dynamical states of the lattice site at consecutive points in time; black squares denote the $n_i(t) = 1$ state, and empty squares denote $n_i(t) = 0$. The arrows and corresponding direction of facilitation are omitted for simplicity. Kinks occur whenever the dynamical state changes, but the majority of these kinks do not endure. We set $t_\mathrm{s} = 5$. The red outlined region contains three kinks that constitute a single enduring kink event, with a red "X" marking the enduring kink time.

In Ref. [67], this procedure is used to find the enduring kinks for a one-dimensional East model, where the sojourn time $t_\mathrm{s} = \tau_\mathrm{x}$, the average time scale for dynamical exchange events. Here, for the $d = 2$ and $d = 3$ Arrow models, we also set $t_\mathrm{s} = \tau_\mathrm{x}$. Fig. 3.5 shows exchange time distributions for the Arrow model in two and three dimensions over a range of temperatures; the mean exchange time at each temperature (our chosen sojourn time) is indicated by a vertical dashed line.

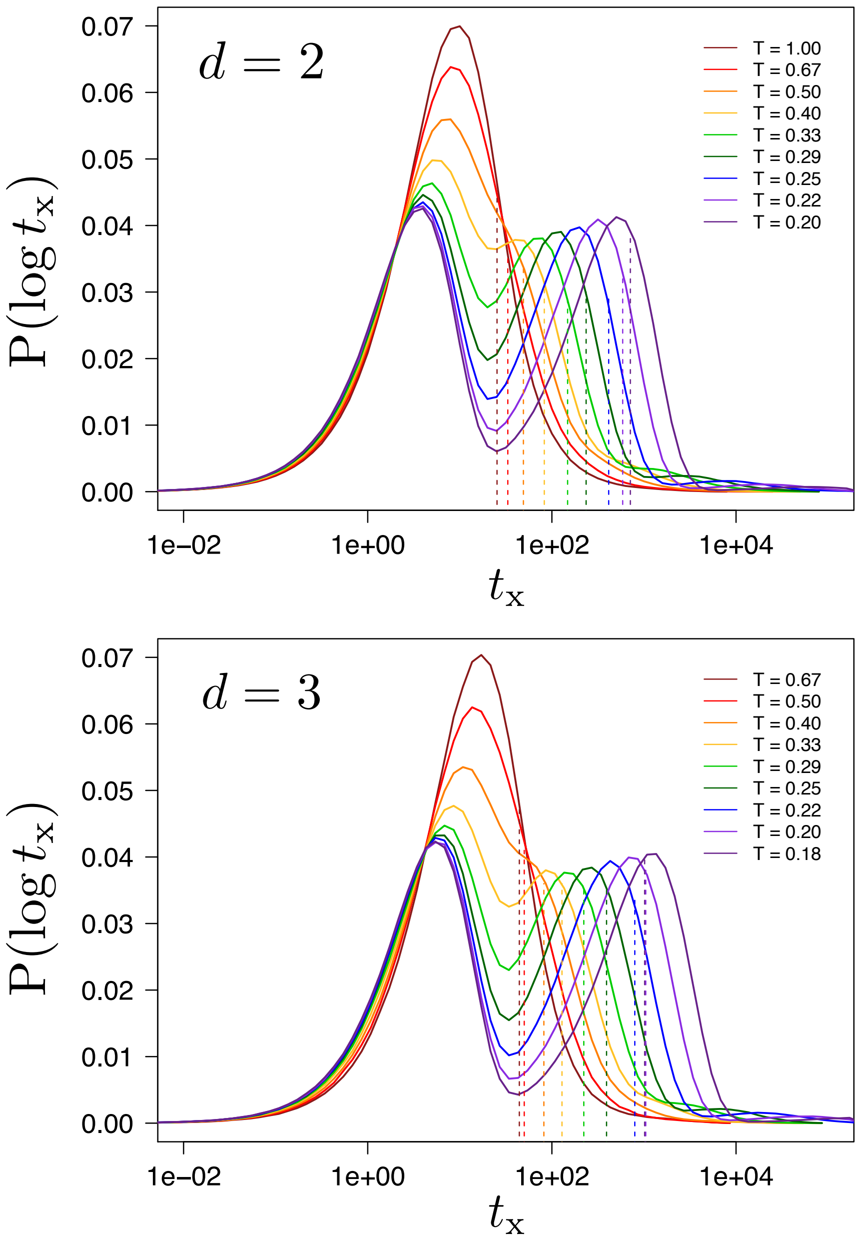

Figure 3.5: Distributions of exchange times for the Arrow model in two (top figure) and three (bottom figure) dimensions for a range of temperatures T. Each vertical dashed line indicates the mean of the exchange time distribution τ_{x} of the same color; these mean times are used for the sojourn time t_s at each temperature. The system sizes used for these calculations are $N = 10,000$ lattice sites for $d = 2$, and $N = 9261$ for $d = 3$. Exchange times t_{x} are expressed in units of Monte Carlo sweeps.

3.4.3 Visualizing Heterogeneous Dynamics

Heterogeneous dynamics in supercooled liquids can be visualized by coloring regions of the liquid according to their mobilities. For atomistic systems, a particle's displacement is measured simply as the Euclidean distance between its initial and final coordinates over some time window. For the Arrow model lattice, displacements are measured in terms of kinks. However, we do not wish to resolve the lattice equivalent of trivial atomistic vibrations, so we consider only kinks that endure.[3] The "displacement" associated with a lattice site i over a time window $\Delta t = t' - t$ can be expressed as the sum of enduring kinks

$$h_i(t, t') = \sum_{t''=t}^{t'} \bar{\kappa}_i(t'') \tag{3.14}$$

occurring during Δt [67], where the overbar in $\bar{\kappa}_i(t)$ denotes an enduring kink. Fig. 3.6 shows a series of three snapshots from a single simulation at increasing Δt, where lattice sites have been colored according to Eqn. 3.14. Blue sites indicate very few or no enduring kinks over Δt; red sites indicate many enduring kinks. This coloring protocol clearly resolves regions of mobility and immobility within the system, reflective of facilitated Arrow model dynamics.

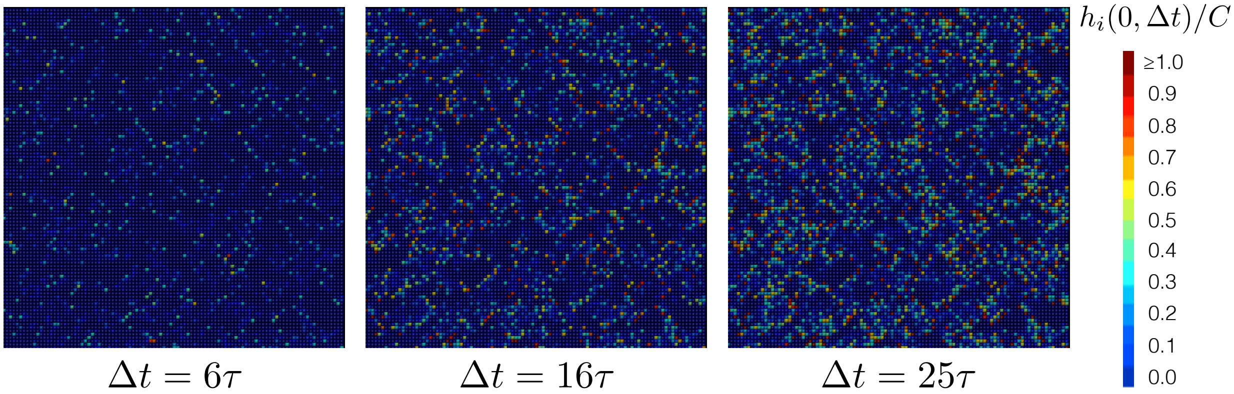

Figure 3.6: Visualization of Arrow model site displacements as a function of time. Sites are colored from blue to red depending on their mobility over a time interval Δt; the color key is shown to the right of the images. Displacements over Δt, $h_i(0, \Delta t)$, are normalized by a constant value $C = 30$ to better resolve mobile and immobile regions. The time intervals Δt are expressed in terms of the structural relaxation time τ corresponding to the temperature of the lattice; note that only enduring kinks are represented in the images, but τ is computed using all kinks. Significant regions of dark blue sites indicate immobile regions of the liquid, while brighter regions indicate higher liquid mobility. This is what is meant by dynamical heterogeneity. A single $N = 10000$, $d = 2$ Arrow model simulation at $T = 0.24$ was used to create this visualization.

---

[3] In atomistic systems, this effect is achieved by coarse-graining particle trajectories over time or computing inherent structures [10].

Resolving Fundamental Excitations

In atomistic systems, elementary excitations are resolved by running many independent trajectories from the same initial configuration and averaging over the resulting particle displacements.[4] This technique, called "isoconfigurational averaging" [68], highlights regions of the initial liquid configuration that consistently become mobile due to the underlying structure. However, we are only interested in significant, enduring displacements. Ref. [68] performed isoconfigurational averaging on short raw trajectories—analyzing trivial vibrations along with enduring displacements—therefore obscuring any information on meaningful dynamical events. Here, we adapt the technique as carried out by Ref. [10], where only enduring kinks are considered, for use with the Arrow model.

The isoconfigurational average displacement is the average displacement of each site i over M independent trajectories originating from the same initial configuration

$$I_i(t,t') = \frac{1}{M}\sum_{j=1}^{M} h_i^{(j)}(t,t') \tag{3.15}$$

where the superscript j indicates the specific trajectory from which the displacement is measured. We generate independent trajectories from an initial configuration by randomly selecting vectors $\mathbf{v}_i$ to reassign the facilitation directions for all lattice sites containing excitations ($n_i = 1$).[5] Each trajectory then has a distinct set of facilitation directions $\{\mathbf{v}_i\}$.

The visualization protocol detailed in Eqn. 3.14 and used to make Fig. 3.6 will still resolve the excitations featured by isoconfigurational averaging, but they will be more irregular. We return to this technique later in Chapter 5, in the context of side-chain motions in biomolecules.

3.4.4 Fractal Dimension

The shapes of dynamical heterogeneities in a glassy system can be quantified with the fractal dimension d_f. In general, the fractal dimension gives a measure of spatial complexity for an object, which in this case is a mobile region on the Arrow model lattice. The quantity d_f can be computed directly [69] by clustering neighboring lattice sites that have experienced at least one dynamical event, or kink, over a time window Δt. Here, we use $\Delta t = \bar{\tau}$, the structural relaxation time computed using only enduring kinks. The fractal dimension can then be computed as

$$d_\mathrm{f} = \frac{\mathrm{d}\ln(n)}{\mathrm{d}\ln(r)} \tag{3.16}$$

---

[4] In atomistic systems, independent trajectories are obtained by randomly drawing particle velocities for each trajectory (originating from the same initial configuration) from the appropriate Maxwell-Boltzmann distribution.

[5] Vectors are drawn from a uniform distribution of the g discrete directions.

where n is the number of relaxed lattice sites over Δt contained within a spherical volume of radius r positioned at the cluster centroid. Fig. 3.7a demonstrates this procedure for a $d = 2$ Arrow model at $T = 0.31$.

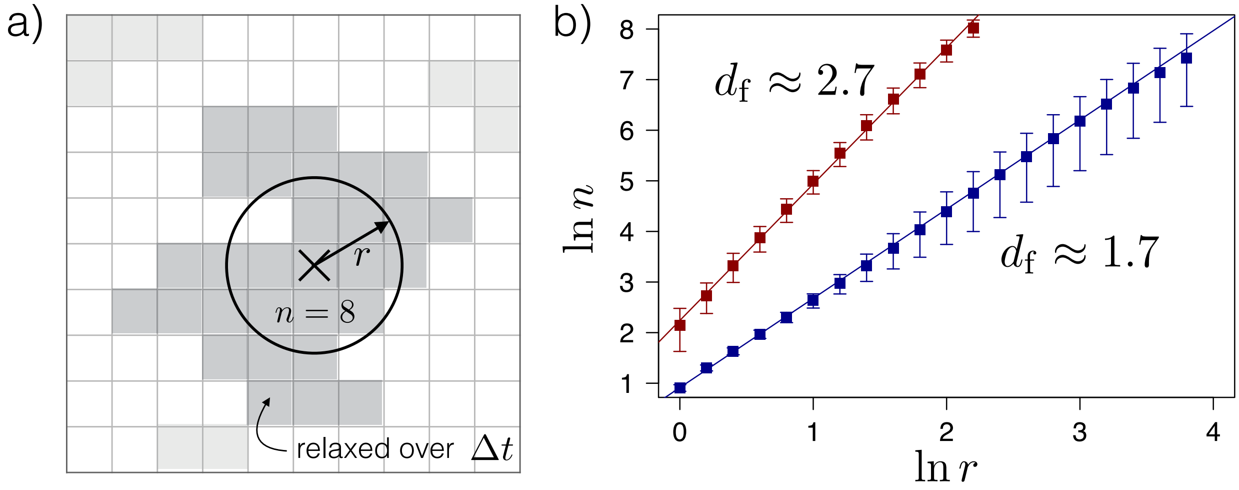

Figure 3.7: Computing fractal dimension for the Arrow model. (a) A schematic illustrating how the fractal dimension is computed for a hypothetical configuration of relaxed sites on a $d = 2$ Arrow model. The dark shaded sites have relaxed over time Δt via enduring kinks and compose the cluster of interest; the cluster centroid is marked with an "X." The quantity n is the number of relaxed sites within a radius r of the cluster centroid (in this case, $n = 8$). (b) Plots of $\ln n$ vs. $\ln r$ for 2 (blue squares) and 3 (red squares) dimensions with error bars obtained from averaging independent configurations. The slopes of these lines are the computed fractal dimensions d_{f}, as expressed in Eqn. 3.16.

This procedure is carried out for $d = 2$ ($N = 1 \times 10^4$ sites) and $d = 3$ ($N = 9261$ sites) Arrow models simulated at $T = 0.31$ and $T = 0.28$, respectively.[6] In both cases, $\Delta t = \bar{\tau}$ for the specific model dimension and temperature. We run independent realizations of the Arrow model and compute n vs. r for the final configuration of each simulation; we then average the results from all samples and compute the standard deviation.[7] Fig. 3.7b shows plots of $\ln n$ vs. $\ln r$, with error bars equal to a single standard deviation from the mean. We find $d_{\mathrm{f}} = 1.74 \pm 0.01$ and $d_{\mathrm{f}} = 2.65 \pm 0.03$ for dimensions $d = 2$ and $d = 3$, respectively, values comparable to those reported for atomistic systems [10]. This result implies that the general shapes of mobile regions within atomistic systems and the Arrow model are the same. In the following sections, we use $d_{\mathrm{f}}(d) = 1.8(2), 2.6(3)$ unless otherwise noted.[8]

---

[6] We find that the temperature at which we run the system does not significantly affect our values for d_{f}.

[7] We consider 100 independent simulations for $d = 3$ and 1000 for $d = 2$.

[8] These values for d_{f} have been used in atomistic system calculations [10] and are commensurate with our results from the Arrow model, so we choose to use them here.

3.4.5 Mobility Susceptibility

In Section 3.4.4, we compute the fractal dimension of the Arrow model in order to demonstrate that the general shapes of its dynamical heterogeneities are commensurate with those of atomistic systems. Here, we utilize a quantitative measure of how the spatial fluctuations in mobility change with temperature. The specific correlation function computed in this section is motivated by susceptibilities measured for static thermodynamic phase transitions and is a generalization for transitions in space and time.

As a system approaches a general thermodynamic phase transition, namely one that occurs in configuration space and is not dynamical in nature, the growth of a linear response function, or "susceptibility," is observed [3]. For a first-order transition, growing susceptibilities are associated with increased fluctuations in an order parameter. For instance, the Ising model—a lattice model consisting of "up" and "down" spins that is often invoked to study phase transitions—experiences a growth in the size of domains of sites with the same spin orientation as the model approaches a first-order phase transition.[9] The magnetization of the Ising lattice is defined as the difference between the number of "up" spins and number of "down" spins and serves as an order parameter. A susceptibility is computed by measuring the degree to which this order parameter changes in response to small perturbations by an external field coupling to the magnetization. This susceptibility diverges at the phase transition.

While the susceptibility described above corresponds to a standard thermodynamic phase transition, the glass transition as described in Section 1.1 is instead a transition in space and time [70, 19, 2]. That is, a supercooled liquid approaching the glass transition is characterized by a growth in dynamical heterogeneities and thus requires consideration of both space and time. Quantities typically used to characterize standard thermodynamic transitions have been generalized to describe space-time transitions [71, 72] such that dynamics is included. In the case of a supercooled liquid, an analogous susceptibility is the $\chi_4(t)$ function [40, 73], which measures the variance in lattice site mobilities and reflects the presence of large domains of mobility and immobility.

To calculate $\chi_4(t)$ for the Arrow model, we simply compute the variance in the persistence function defined in Eqn. 3.10

$$\chi_4(t) = \langle P(t)^2 \rangle - \langle P(t) \rangle^2 \tag{3.17}$$

where the angled brackets denote a time average as in Eqn. 3.11. The variance in $P(t)$ resolves spatial correlations among lattice sites and peaks at the time of maximum dynamical heterogeneity. Fig. 3.8a shows the decay in $\langle P(t) \rangle$ for a range of temperatures, and Fig. 3.8b plots the corresponding $\chi_4(t)$, with curves ranging from red to dark purple as the temperature is lowered. As expected, the peak of $\chi_4(t)$ gets larger with decreasing temperature as domains of immobility grow larger. Additionally, the time at which this peak occurs is pushed out to longer timescales.

---

[9] For a summary of the Ising model and its associated phase transitions, see Section 4.2.2.

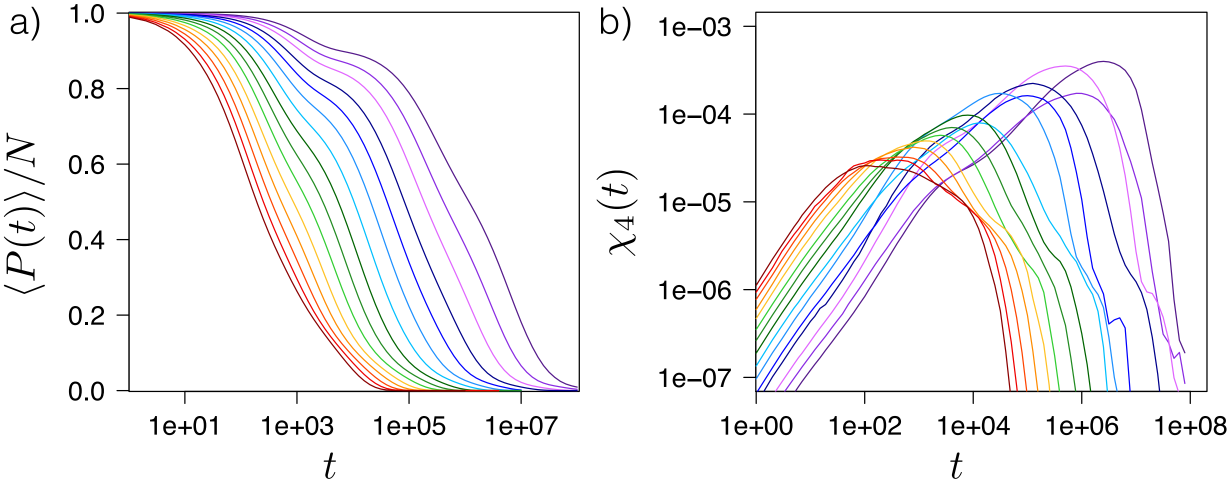

Figure 3.8: Mobility susceptibilities for the $d = 3$ Arrow model over a range of temperatures. (a) The decay of the persistence function $\langle P(t)\rangle/N$ as a function of time, where N is the total number of lattice sites. Temperatures range from $T = 0.38$ (dark red) to $T = 0.19$ (dark purple). (b) The variance $\chi_4(t)$ for the same range of temperatures. Times are expressed in units of Monte Carlo sweeps.

3.5 Mapping to Atomistic Systems

The previous sections demonstrate that the Arrow model exhibits super-Arrhenius relaxation and heterogeneous dynamics similar to that of atomistic supercooled liquids. However, in order to simulate the Arrow model to correspond to a specific atomistic system, generalization is required to account for differing energy scales of characteristic excitations. To illustrate this, we perform a mapping derived from East-like scaling to determine the energetics and lattice length scale of the Arrow model corresponding to a specific atomistic system.

The mapping analysis with the scaling equations described in this section was originally formulated for the East model [20], but it is straightforward to extend it to the Arrow model. The East model exhibits logarithmic scaling of activation energy required to relax domains of length ℓ [10]

$$J_\ell = J_\sigma[1 + \gamma \ln(\ell/\sigma)] \tag{3.18}$$

where J_σ is the activation energy to relax domains of a fundamental length scale σ, and γ accounts for entropy of relaxation pathways. For the one-dimensional East model, these material properties take the values $J_\sigma = 1$, $\sigma = 1$, and $\gamma = (\ln 2)/2$ [74, 75]. Here, we wish to relate the fundamental energy scaling of an atomistic system to the Arrow model. We denote the material parameters for the atomistic system as σ, J_σ, and γ; and choose ℓ_0, J_0, and γ_0 to refer to these same material properties for the Arrow model. Treating σ and ℓ_0 as distinct length scales, each with a corresponding energy scale J_σ and J_0, we obtain

$$J_0 = \frac{J_\sigma}{1 + \gamma_0 \ln(\sigma/\ell_0)} \tag{3.19}$$

and

$$\gamma = \frac{\gamma_0}{1 + \gamma_0 \ln(\sigma/\ell_0)} \tag{3.20}$$

from Eqn. 3.18. These scaling relations allow us to determine the correct Arrow model energy scale J_0 that corresponds to the set of specific material properties J_σ and γ for an atomistic system. The parameter γ_0 can be determined empirically from Arrow model relaxation data.

We can also express the corresponding equilibrium Arrow model excitation concentration in units of lattice length ℓ_0 as

$$c_{\text{eq}}\ell_0^d = \frac{g}{g + \exp(\tilde{\beta} J_0)} \tag{3.21}$$

where

$$\tilde{\beta} = 1/T - 1/T_{\text{o}} \tag{3.22}$$

corresponds to inverse temperatures for the atomistic system, and $g = 2^d$.[10]

3.5.1 Determination of Parameter Values

Application of Eqns. 3.19 and 3.20 requires values for several material parameters, as well as a measure of the entropy of relaxation pathways in the Arrow model. In this section, we discuss how these values are computed.

Atomistic Material Parameters

The value of σ is a particle diameter for all systems studied here, as is done in Ref. [10], but the values of γ and J_σ are unique to each material. In simulated liquids, the value of J_σ can be determined by considering the Boltzmann temperature dependence of the excitation concentration and fitting data to

$$c_\sigma \propto \exp\left[-J_\sigma\left(\frac{1}{T} - \frac{1}{T_{\text{o}}}\right)\right] \tag{3.23}$$

where c_σ is the concentration of particles displacing at least a distance σ over a window of time [10]. The parameter γ is of order unity and can be computed using the relationship

$$J = J_\sigma \sqrt{\frac{\gamma}{d_{\text{f}}}} \tag{3.24}$$

where J is the fit parameter from the parabolic law in Eqn. 2.4. Values of J_σ and γ are material-specific but are typically of order unity for three-dimensional liquids (J_σ is typically of order 10 in two-dimensional systems).

---

[10] In an earlier section, we defined the equilibrium concentration similarly (Eqn. 3.5), where $1/T$ for the Arrow model is representative of $\tilde{\beta}$ (Eqn. 3.22) in atomistic systems. In this earlier definition, expressing the concentration in terms of $\ell_0 = 1$ is implied.

Arrow Model Parameter

To calculate the value of γ_0 for the Arrow model, we use Eqn. 3.24, substituting γ_0 for γ and J_0 for J_σ. In order to distinguish between values of the curvature parameter J for atomistic and Arrow models, we represent this value as "J_A" for the Arrow model. The value of J_A is determined by fitting temperature-dependent structural relaxation data as plotted in Fig. 3.2b; however, we do not fit relaxation data to the parabolic law as expressed in Eqn. 2.4. Hierarchal dynamics is an essential component of the Arrow model at all temperatures, and so there is no defined onset temperature. Instead, we fit the data to a general quadratic equation as is done for the East model in Ref. [75], where the coefficient of the quadratic term is equal to J^2. When we follow this procedure, we obtain a value $\gamma_0 = 1.1$.

3.5.2 Mapping Procedure

Given the measured values of J_σ and γ for the atomistic system and the value of γ_0 for the Arrow model, we can map Arrow model simulations with specific concentrations of excitations to the corresponding temperature in the atomistic system. From Eqns. 3.19 and 3.20, we see that the energy scale J_0 for the Arrow model which corresponds to the energetics of the specific atomistic system is given by

$$J_0 = J_\sigma \left(\frac{\gamma}{\gamma_0} \right) \tag{3.25}$$

Combining Eqn. 3.21 with Eqn. 3.24 and rearranging, we obtain

$$\beta = \beta_\mathrm{o} + \left(\frac{\gamma_0}{J_\sigma \gamma} \right) \ln\left(\frac{g[1 - c_\mathrm{eq}\ell_0^d]}{c_\mathrm{eq}\ell_0^d} \right) \tag{3.26}$$

where $\beta = 1/T$ and $\beta_\mathrm{o} = 1/T_\mathrm{o}$ denote the inverse temperature and the onset inverse temperature for the atomistic system, respectively, that correspond to the specific values of J_σ, γ, γ_0, and the equilibrium Arrow model concentration. From here, we simply plug in the concentration of excitations for a specific Arrow model simulation to find the corresponding atomistic system temperature.

The ratio between the length scales of the atomistic system and the Arrow model can be obtained by considering either Eqns. 3.19 or 3.20 with our measured parameters. We find

$$\frac{\sigma}{\ell_0} = \exp\left(\frac{1}{\gamma} - \frac{1}{\gamma_0} \right). \tag{3.27}$$

We consider the 12 atomistic model and density combinations studied in Ref. [10]. Table 3.1 summarizes the systems used in our study with their corresponding material parameters as reported in Table 2 of Ref. [10]. For all of the two and three dimensional atomistic systems considered , we find that the Arrow model lattice length is roughly half to one-fifth the size of the fundamental length scale of the atomistic system. In order words, multiple Arrow

model [10]	ρ	J_σ	γ	T_o	J_0	σ/ℓ_0
2D-68:32	0.7	11.3	0.62	1.36	5.6	1.81
	0.75	21.8	0.57	2.13	9.9	2.09
KA	1.15	4.0	0.55	0.67	2.2	2.23
	1.2	5.3	0.41	0.87	2.2	4.14
	1.25	7.4	0.39	1.06	2.9	4.69
	1.3	8.4	0.39	1.34	3.3	4.69
W	1.2	4.5	0.59	0.66	2.7	1.97
	1.25	6.9	0.42	0.78	3.0	3.91
	1.296	9.4	0.36	0.88	3.5	5.81
WCA3D	1.2	2.1	0.51	0.32	1.1	2.57
	1.25	3.5	0.51	0.45	1.8	2.57
	1.296	5.0	0.47	0.58	2.4	3.03

Table 3.1: Table of atomistic systems and corresponding model parameters [10] for Arrow model mappings. The 2D-68:32 model is two-dimensional; the rest of the models are three-dimensional.

model sites are needed to correspond to a single particle in an atomistic liquid. Table 3.1 summarizes these results.

Although we do not utilize this mapping between atomistic liquids and the Arrow model in the remainder of this chapter, we do revisit it later in this dissertation. In Chapter 4, we incorporate this Arrow model parameterization into the parameterization of a new lattice model, the “Arrow-Potts” model.

3.6 Cooling Experiments

Now that we have established a correspondence between Arrow model parameterizations and atomistic system energy and length scales, we can explore Arrow model experiments that have relevance for atomistic models. Ref. [10] presents results from cooling experiments for the materials listed in Table 3.1 and finds that the concentration of excitations, or mobile regions, within the liquid decreases as the temperature decreases along the cooling trajectory. They also find that the distribution of lengths for an equilibrium system is exponential and excitations are distributed as an ideal gas. Ref. [76] presents similar results from one-dimensional East model simulations, where spatial distributions of excitations are computed for both equilibrium and nonequilibrium configurations along a cooling trajectory. The nature of the nonequilibrium configurations is dependent on the temperature at which the East model fell out of equilibrium. In this sense, the specific cooling protocol is reflected in the resulting excitation structure out of equilibrium.

We carry out similar calculations for the two-dimensional Arrow model. The model is cooled from a temperature $T > T_\mathrm{o}$ through its onset temperature to $T = 0$ at a rate ν where we define

$$\nu = \frac{\Delta T}{\Delta t} \tag{3.28}$$

as the temperature decrease per time step (measured in Monte Carlo sweeps for the Arrow model). As long as the cooling rate is slow enough to allow the system to relax at each temperature, the system remains in equilibrium, and an equilibrium length is associated with the characteristic distance between nearest excitations for a specific temperature. At some point, however, the model will fall out of equilibrium. In the following sections, we explore the implications of falling out of equilibrium during a cooling trajectory and characterize Arrow model configurations from both equilibrium and nonequilibrium states.

3.6.1 The Glass Transition

As long as the cooling rate ν is slow enough to allow for microscopic reorganization at each temperature decrease, a supercooled liquid remains in equilibrium. The liquid goes through a glass transition—and therefore falls out of equilibrium—at temperature T_{g} when

$$\frac{1}{\nu} \approx \left| \frac{\mathrm{d}\tau}{\mathrm{d}T} \right|_{T=T_{\mathrm{g}}} \tag{3.29}$$

where τ is the temperature-dependent structural relaxation time for the model. The glass transition temperature is therefore dependent on the specific cooling rate used to prepare the system.

We carry out cooling experiments for the Arrow model where the model is cooled from $T = 0.7$ to $T = 0$ and then warmed to its initial temperature at different rates ν spanning several orders of magnitude. When excitation concentration is plotted as a function of temperature, we observe that the concentration remains essentially unchanged once the model falls out of equilibrium during a cooling trajectory. Fig. 3.9 shows data from cooling (solid lines) and subsequent warming (dashed lines) trajectories for values of ν that span four orders of magnitude, where the natural logarithm of excitation concentration

$$c = \frac{1}{N} \sum_{i=1}^{N} n_i \tag{3.30}$$

is plotted against inverse temperature. Initially, as the model is cooled but remains in equilibrium, the concentration decreases and $c \approx c_{\mathrm{eq}}$ for a given temperature. Once the model falls out of equilibrium, the concentration remains relatively constant at a value $c > c_{\mathrm{eq}}$ throughout the remainder of the cooling trajectory. This behavior is observed for the one-dimensional East model, where the space-time structure of excitations is more easily visualized [76]. While short-lived kinks may still occur, enduring kinks (which correspond to enduring displacements of approximately a particle diameter in atomistic systems) are exceedingly rare. The space-time excitation structure is therefore relatively static for temperatures below the glass transition, characteristic of frozen amorphous regions in a supercooled liquid.

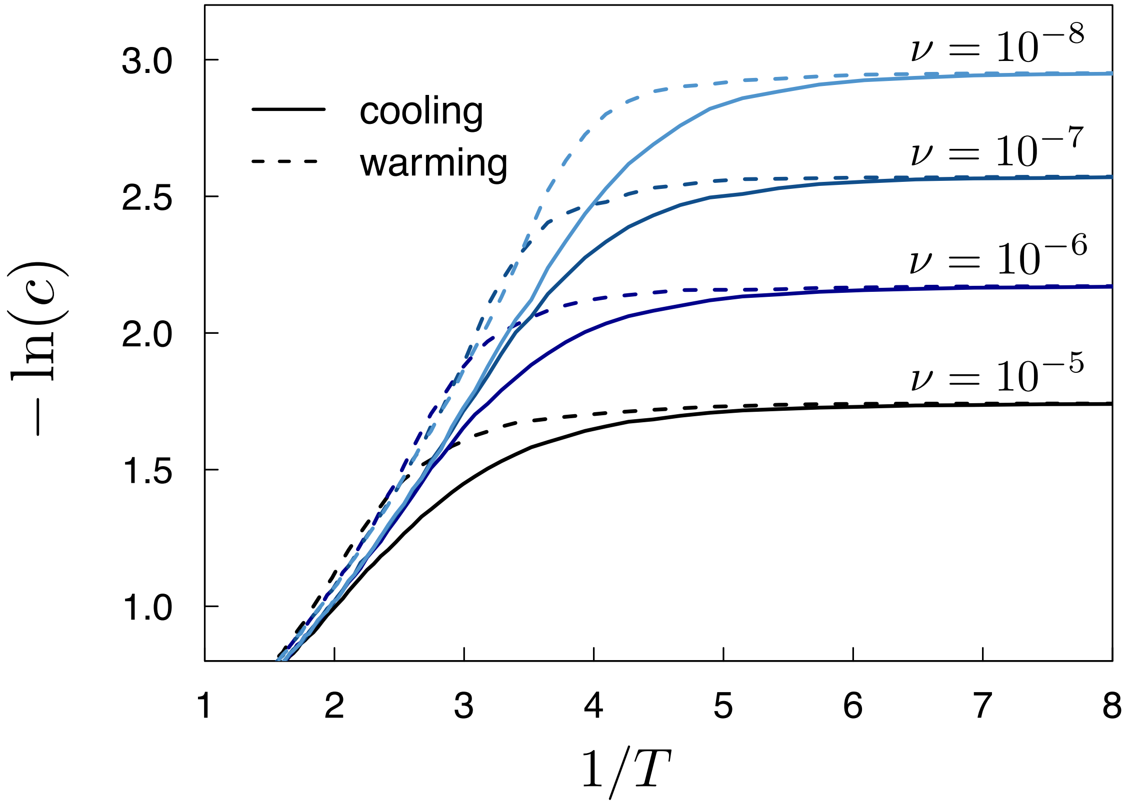

Figure 3.9: Cooling and warming trajectories for the $d = 2$ Arrow model to illustrate hysteresis. The natural log of excitation concentration c is plotted as a function of inverse temperature for trajectories with cooling/warming rates that span four orders of magnitude. The system is cooled from an equilibrated liquid configuration at $T = 0.7$ to $T = 0$ at a rate $-\nu$; the system is then warmed back to the initial temperature at rate ν. Each curve is the average over 16 independent cooling/warming runs for systems of size $N = 10000$ ($\nu = 10^{-5}, 10^{-6}, 10^{-7}$) and $N = 5000$ ($\nu = 10^{-8}$). For each rate ν, the warming and cooling curves do not lie on top of each other in the intermediate temperature regime; T_{g} is found in this region.

After cooling to $T = 0$, the Arrow model is warmed at the same rate from the final configuration of excitations. However, excitation concentrations at the same temperature along corresponding cooling and warming trajectories need not be the same; Fig. 3.9 resolves hysteresis in the neighborhood of T_{g}. Note that as the cooling/warming rate decreases, the glass transition occurs at lower temperatures due to increased time for structural reorganization to occur.

3.6.2 Equilibrium and Nonequilibrium Lengths

As a supercooled liquid is cooled, the concentration of excitations decreases. As long as the system is in equilibrium, there is a typical length scale ℓ_{eq} separating nearest excitations, where the subscript indicates that the length corresponds to an equilibrium liquid. This length scale is related to the concentration of excitations

$$\ell_{\mathrm{eq}} \propto c_{\mathrm{eq}}^{-1/d_{\mathrm{f}}} \tag{3.31}$$

where c_{eq} is the equilibrium concentration of excitations. Excitations are uncorrelated, and distributions $\mathrm{P}_{\mathrm{eq}}(\ell)$ of nearest-excitation distances ℓ are exponential. Lengths $\ell < \ell_{\mathrm{eq}}$ correspond to regions in which excitations can readily create and destroy neighboring excitations; lengths $\ell \gg \ell_{\mathrm{eq}}$ correspond to large immobile regions of the liquid [76].

As described in the previous section, a supercooled liquid falls out of equilibrium at the glass transition temperature T_{g}. The characteristic, or most probable, length separating neighboring excitations at a temperature $T < T_{\mathrm{g}}$ is the equilibrium length at T_{g}

$$\ell_{\mathrm{neq}} = \ell_{\mathrm{eq}}(T_{\mathrm{g}}) \tag{3.32}$$

where the subscript “neq” indicates that the length is a nonequilibrium length. The length ℓ_{neq} is therefore intimately related to the cooling protocol.

Out of equilibrium, distributions $\mathrm{P}_{\mathrm{neq}}(\ell)$ of distances ℓ between nearest excitations are no longer exponential. Excitations within close proximity have relaxed each other, and so the nonequilibrium structure is characterized by large regions of immobility. Excitations are no longer uncorrelated; there is a depletion of mobility surrounding each excitation, with ℓ_{neq} giving the most probable distance between excitations.

We compute distributions of lengths between neighboring excitations for Arrow model configurations taken along a cooling trajectory. Recall that in the Arrow model, an excitation is present at site i if the occupation variable $n_i = 1$, i.e. site i is occupied by an arrow. Fig. 3.10 shows three example Arrow model configurations for two different temperatures along cooling trajectories corresponding to two different rates. We see that decreased temperature and slower cooling rate correspond to greater distances between excitations. Below, we consider two different ways in which nearest neighbor distances between excitations in the Arrow model may be defined.

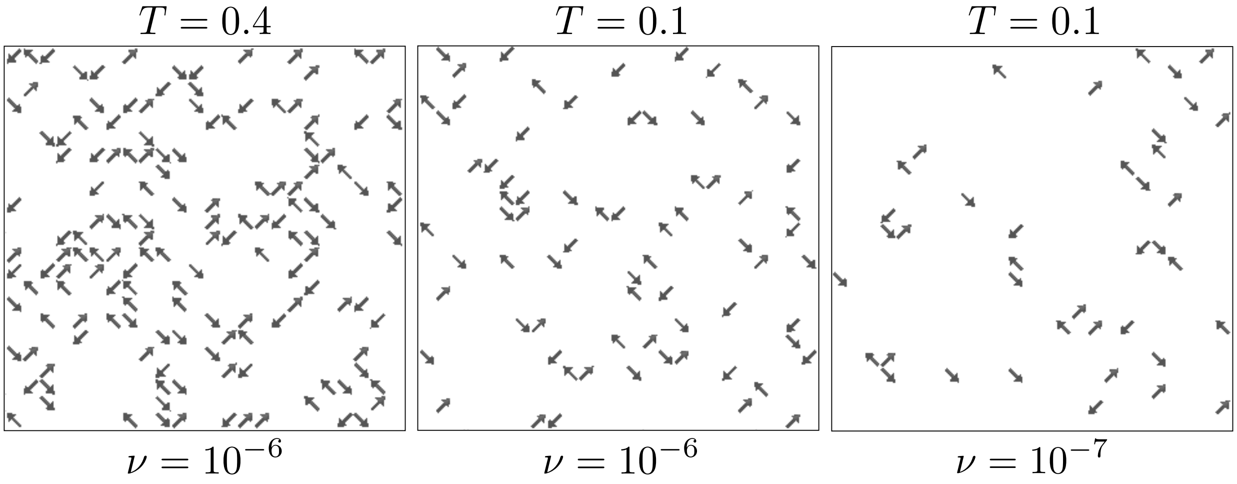

Figure 3.10: Configurations of excitations in a two-dimensional Arrow model. Three Arrow model configurations are shown for two cooling rates and two temperatures. The Arrow model is cooled at rate ν, and the configuration at temperature T is shown. As the temperature decreases, the typical distance between excitations increases. Similarly, a slower cooling rate results in an increased distance between excitations.

Importance of Directionality

The simplest way to compute distributions of nearest neighbor lengths for the Arrow model is to consider every other excitation on the lattice as a candidate nearest-neighbor for a given target excitation. This method gives no consideration to directions of facilitation. However, recall that in the hierarchical ($f = 0$) limit of the Arrow model, excitations may only interact with other excitations with the same facilitation direction. Specifically, excitations can be created or destroyed only by excitations pointing in the same direction. Thus, even if the target excitation is directly next to an excitation of a different direction, one cannot destroy the other and deplete the density of excitations in the surrounding area. The top panel of Fig. 3.11 shows probability distributions for the Arrow model over a range of temperatures as the system is cooled at a rate $\nu = 1 \times 10^{-6}$. The label "any vector" indicates that specific values of $\mathbf{v}_i$ were not considered when determining nearest neighbor excitations, and distributions are colored from red (high temperature) to dark purple (low temperature). While the model has clearly fallen out of equilibrium by the time it has been cooled to $T = 0.1$, there is no evidence of excitation depletion.

The plot in the top right of Fig. 3.11 plots an exponential distribution in dimension d

$$\mathrm{P}_d(\ell) = \frac{\ell^{d-1}}{\langle \ell \rangle^d} \exp[-(\ell/\langle \ell \rangle)^d] \tag{3.33}$$

where the angled brackets denote an average over all nearest excitation lengths for a configuration at a given temperature. If the distribution $P(\ell)$ is exponential, a plot of $\ln[\mathrm{P}(\ell)\langle \ell \rangle^d/\ell^{d-1}]$ versus $(\ell/\langle \ell \rangle)^d$ will yield a straight line. We therefore expect deviations

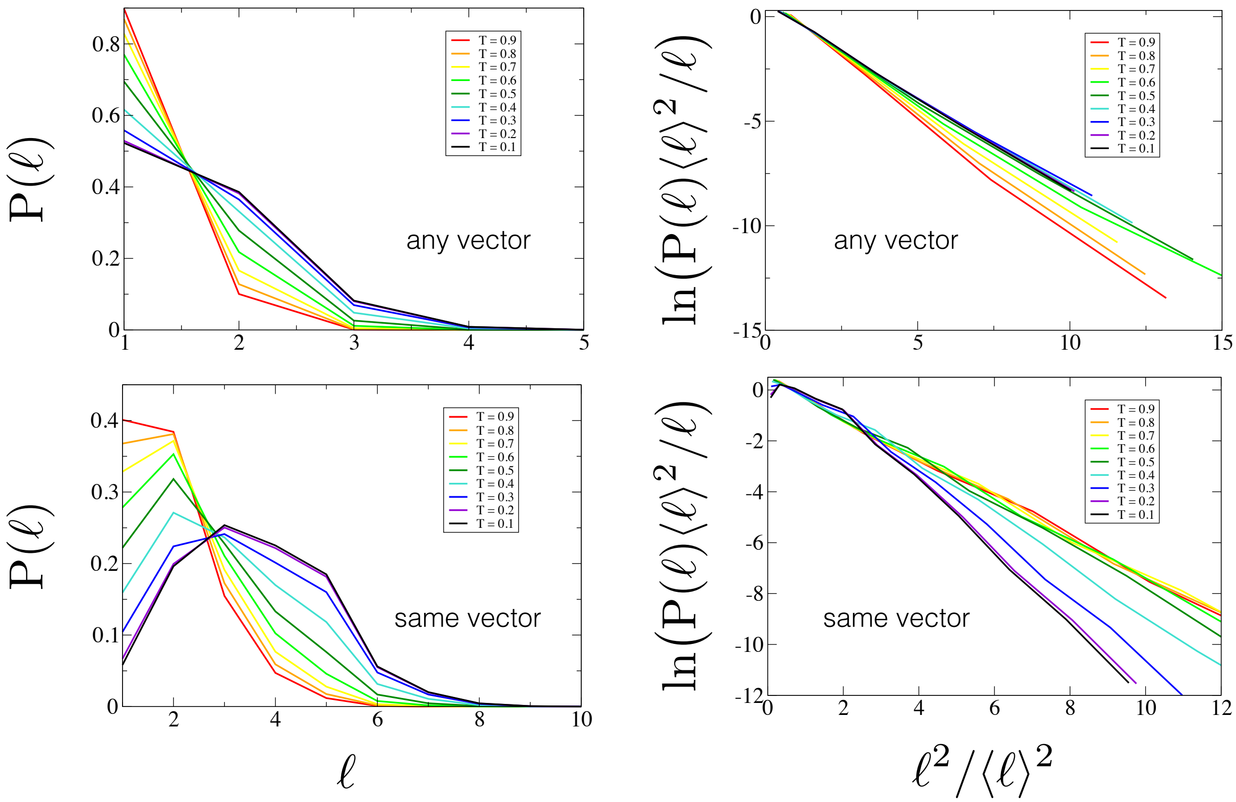

Figure 3.11: Distributions of distances to nearest excitations in the $d = 2$ Arrow model. The system is cooled from $T = 0.9$ (red) to $T = 0.1$ (dark purple) at a rate $\nu = 1 \times 10^{-6}$. At each of the nine temperatures shown, the distribution of distances between nearest excitations is computed, both with consideration of excitation direction and without. The top plots ("any vector") show distributions of distances between nearest excitations of any directionality, or Arrow model site vector. In the bottom plots ("same vector"), only excitations in the same direction are considered.

from linearity in the event of correlations between excitations. Curves for the “any vector” case appear linear at all temperatures and do not indicate the presence of correlations in the excitation structure.

Now, we choose to compute distributions of nearest neighbor lengths in the Arrow model by requiring that any nearest neighbor excitations have the same direction of facilitation. We obtain distributions of lengths like those in the lower panel of Fig. 3.11. Here we find that there is a clear depletion of excitations at small lengths. Furthermore, the plot on the right reveals marked deviations from linearity (and thus correlations between neighboring excitations) at low temperatures.

Consideration of excitation directionality is therefore required in order to resolve correlations between excitations in out-of-equilibrium configurations. This is not terribly surprising, as excitations of different orientations have no chance of relaxing each other in the hierarchical version of the Arrow model utilized here.

Emergence of Correlated Excitations

Recall that in Section 3.4.1 we utilized persistence and exchange times to resolve temporal correlations in relaxation events in the Arrow model. A persistence time was the time until the next excitation from a randomly chosen time origin, while an exchange time was the time between subsequent excitations. Here we use an analogous approach to resolve spatial correlations in configurations of excitations. For an Arrow model configuration at temperature T along a cooling trajectory, we compute distributions of lengths to nearest excitations from both random sites on the lattice and other excitations. As discussed above, we require that excitation-to-excitation lengths only be considered if the two excitations have the same direction of facilitation. Fig. 3.12 shows the resulting probability distributions for two different cooling rates, where dashed lines indicate distances from random sites, and solid lines indicate distances from other excitations. We observe a decoupling of distributions at low temperatures, when the system has fallen out of equilibrium and excitation structure is correlated. At high temperatures, when excitations are uncorrelated, these distributions are the same. Comparing the two different cooling rates $\nu = 1 \times 10^{-5}$ and $\nu = 1 \times 10^{-6}$, we see that the distributions become decoupled at higher temperatures when the model is cooled at the faster cooling rate.

3.7 Conclusions

In summary, we have characterized the dynamics and excitation structure of the Arrow model, a kinetically-constrained model for glassy dynamics. The Arrow model contains only facilitation and directionality of dynamics, and so captures the fundamental physics of particle motion according to the dynamical facilitation theory of the glass transition.[11] In the

---

[11] See Section 1.2 for more information on the dynamical facilitation theory of the glass transition.

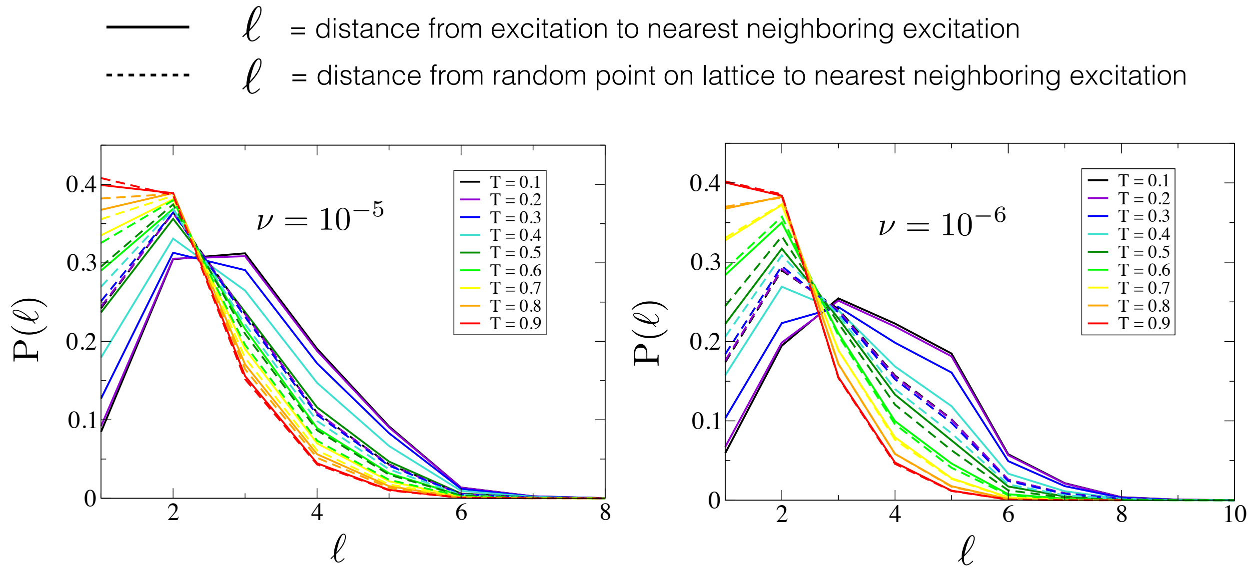

Figure 3.12: Distributions of distances to nearest excitations in the $d = 2$ Arrow model from both excitations and random points on the lattice. The system is cooled from $T = 0.9$ (red) to $T = 0.1$ (dark purple) at rates $\nu = 1 \times 10^{-5}$ (left) and $\nu = 1 \times 10^{-6}$ (right). At each of the nine temperatures shown, the distribution of distances between nearest excitations is computed (solid lines), where only excitations in the same direction as the origin excitation are considered. Distributions of distances from random points on the lattice to the nearest excitation are shown in dashed lines. These distributions become decoupled at low temperatures $T \approx T_{\mathrm{g}}$, which reflects correlations between excitations.

hierarchical ($f = 0$) limit of the model, relaxation is super-Arrhenius as is observed in experimental glass-formers. The nature of dynamical heterogeneities in the Arrow model is shown to be commensurate with that observed in atomistic systems, and so we can define a mapping between the two systems that takes into account differing energy scales of hierarchical dynamics. This mapping allows for direct correspondence between atomistic system temperatures and specific excitation concentrations at which the Arrow model is simulated.

In the next chapter, we explore an application of the Arrow model in a hybrid "Arrow-Potts" model. When combined with a Potts model—a lattice model capable of undergoing a first-order thermodynamic phase transition—the Arrow model captures the sluggish dynamics that slows crystal growth in a system cooled below its melting temperature. It also provides the kinetic constraints necessary for long-lasting polycrystalline structure as observed in experimental systems.

Chapter 4

A Coarse-grained Model for Crystallization, Vitrification, and Polycrystallinity

4.1 Introduction

In this chapter, we explore an application of the coarse-grained model for glassy dynamics characterized in the previous chapter. We join the Arrow model [18]—which is discussed at length in Chapter 3 and provides kinetic constraints fundamental to glassy dynamics—with a second lattice model that undergoes a first-order thermodynamic phase transition. With both glassy dynamics and the thermodynamics to crystallize, this model can simultaneously exhibit sluggish dynamics and the drive to the crystal state experienced by a material cooled below its melting temperature. We use this model to explore the competition between crystallization and vitrification inherent to the formation of polycrystalline materials, as well as the resulting material structure. We begin by describing the processes of crystallization and vitrification, as well as the characteristic features of polycrystalline materials. This work was done in collaboration with Kranthi Mandadapu.

4.1.1 Theory of Crystallization

The process of crystallization consists of two events: (1) nucleation of a nascent crystal and (2) subsequent growth of that crystal. The overall timescale for crystallization, τ_{xtl}, is dependent on the timescales of these events and has the approximate form

$$\tau_{\mathrm{xtl}} = \Gamma(V)\nu^{-1}(T)e^{\Delta F(T)/k_{\mathrm{B}}T} \tag{4.1}$$

where $\Delta F(T)$ is the free energy cost to grow a critical nucleus of the crystal at temperature T, and $\nu^{-1}(T)$ is the temperature-dependent timescale at which new material is added to the growing crystal [45]. This timescale ν^{-1} corresponds to molecular reorganization at small length scales. $\Gamma(V)$ is a system size correction dependent on liquid volume V, as discussed later in this section. k_B is Boltzmann's constant.

At moderately supercooled temperatures, the crystalline phase is separated from the metastable liquid phase by a free energy barrier $\Delta F(T)$ [77]. The form of $\Delta F(T)$ is motivated by classical nucleation theory (CNT), which has been used to successfully estimate nucleation rates at moderately supercooled temperatures [78]. The general form of the free energy term can be written as

$$\Delta F(T) = \Phi(\gamma/\Delta h)(T - T_\mathrm{m})^{-2} \tag{4.2}$$

where $\Phi(\gamma/\Delta h)$ is a function of surface energy γ and bulk energy Δh [45]. To lowest order, this quantity is independent of temperature [6]. The dependence on $(T - T_\mathrm{m})^{-2}$ ensures a free energy function that increases with temperature until the melting temperature T_m, where $\Delta F(T)$ goes to infinity.

The prefactor for the timescale for crystal growth, $\nu(T)^{-1}$, is related to how quickly material can reorganize and add to the burgeoning crystal. This reorganization time is approximately the time for molecules to diffuse a characteristic microscopic length. At high temperatures, there is little temperature dependence, as molecules can easily reorganize. At temperatures below the melting temperature T_m, however, the drastic slowing of liquid dynamics results in diffusion with a super-Arrhenius dependence on temperature

$$D \propto \exp\left[-\xi J^2 \left(\frac{1}{T} - \frac{1}{T_\mathrm{o}}\right)^2\right] \tag{4.3}$$

where the onset temperature T_o is commensurate with T_m, and $\xi \leq 1$ is a constant that reflects the extent to which the Stokes-Einstein relation $D \propto T/\eta$ is violated.[1]

For decreasing $T < T_\mathrm{m}$, the slowing of liquid dynamics relevant to crystal growth competes with the increasingly favorable free energy for crystal nucleation. The result is a non-monotonic curve for the crystallization timescale τ_xtl, an example of which is shown in Fig. 4.1. Contributions to Eqn. 4.1 from slowing liquid dynamics and increasing thermodynamic favorability of crystallization are shown in blue and red dashed lines, respectively.

In addition to the $\nu^{-1}(T)$ term in Eqn. 4.1, there is a second prefactor $\Gamma(V)$ that reflects the system size dependence of τ_xtl. At moderately supercooled temperatures, the process of crystallization is nucleation-limited; it can take awhile for a critical nucleus to form, but once it does, the entire system quickly crystallizes. As the size of the system increases, there are more opportunities for such nuclei to form. In this sense, an increase in system size contributes to a decrease in the crystallization timescale τ_xtl. At deeply supercooled temperatures, critical nuclei form readily, and crystallization is instead diffusion-limited. In this low-temperature regime, a larger system volume means that more material that has to be reorganized, contributing to a longer τ_xtl. The dependence on system size is thus non-monotonic with respect to volume, though its effect in Eqn. 4.1 is insignificant relative to the other two terms.

---

[1] The fractional Stokes-Einstein relation is $D \propto T/\eta^\xi$, where $\xi < 1$ at supercooled temperatures. See Section 2.4 for more information on the breakdown of the Stokes-Einstein relation at low temperatures.

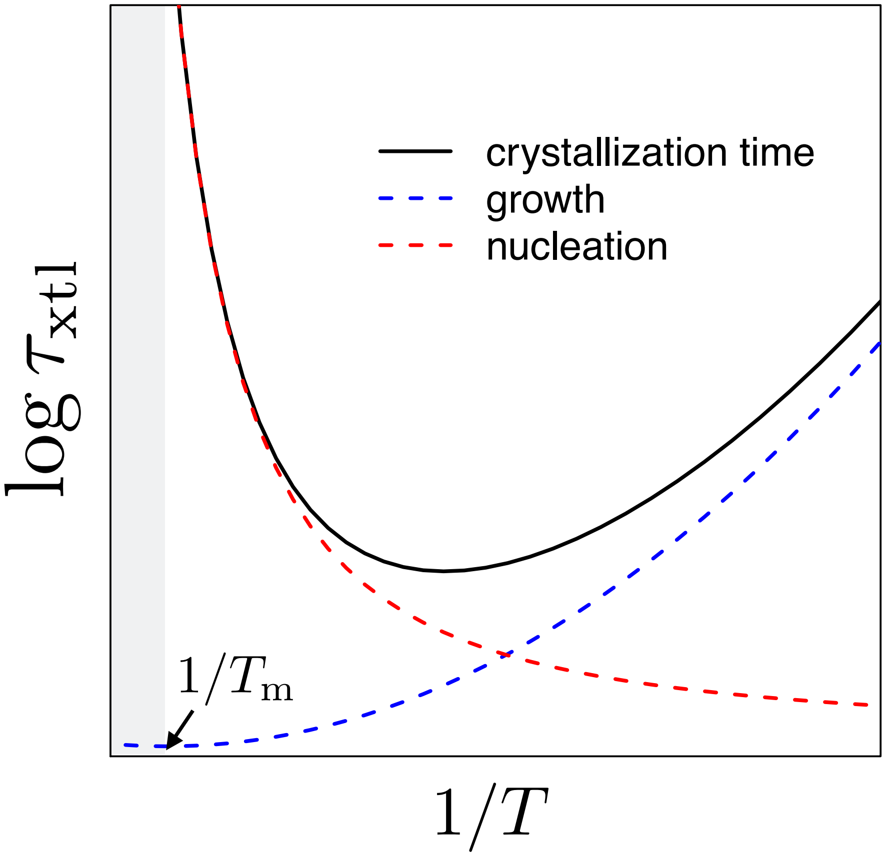

Figure 4.1: Illustration of timescales for crystallization. The black curve shows the non-monotonic temperature-dependence of τ_{xtl} in Eqn. 4.1. The dashed blue curve shows the contribution from liquid dynamics that slows down with decreased temperature. The dashed red curve shows the contribution from the decreasing nucleation time with decreasing temperature. The gray shaded region indicates temperatures above the melting temperature T_{m}; the approximate location of T_{m} is indicated. Forms for the three curves are taken from Ref. [45]. The system size correction $\Gamma(V)$ is not shown but is expected to be a non-monotonic contribution with respect to volume.

4.1.2 Vitrification

The form in Eqn. 4.1 (shown in Fig. 4.1) implies that even if the crystal state is thermodynamically favored at a particular temperature, sluggish liquid dynamics may drastically increase the time required to add to a nascent crystal, resulting in a longer timescale for crystallization. If the material is cooled or quenched such that molecules are unable to reorganize into a crystalline structure before liquid dynamics becomes prohibitively slow, the material may instead form a glass. The proximity in timescales between crystal formation and liquid dynamics influences whether the material crystallizes or forms an amorphous solid, a concept illustrated by time-temperature-transformation plots. Fig. 4.2 shows a time-temperature plot for the TIP5P water model featured in Ref. [45]. In a finite-sized system, the supercooled liquid state is metastable for some temperature range below T_m. The region of supercooled liquid instability—where there is no longer a free energy barrier between liquid and crystal—is shaded gray, and the gap between the liquid and crystal curves is given by the gap parameter Δ [45]. This parameter measures the difference in timescales between liquid dynamics and crystal formation at the temperature below which there is no barrier to crystallization. The magnitude of Δ differs depending on the material.

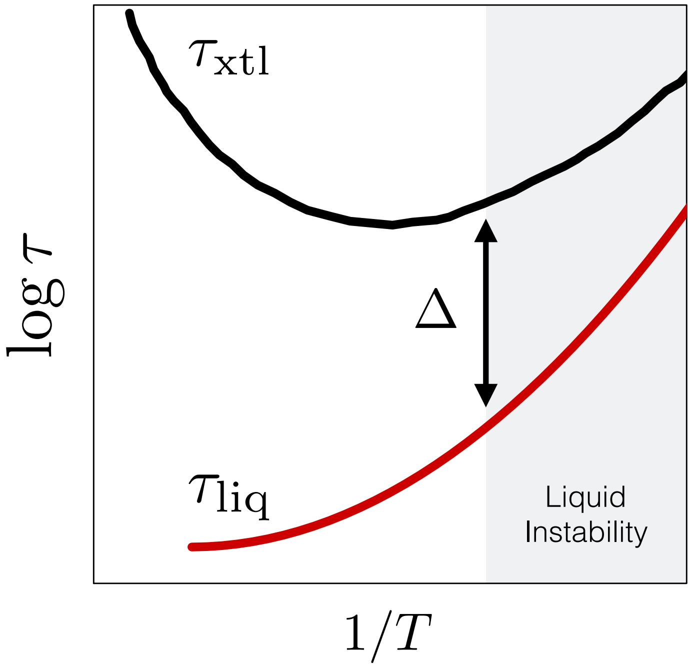

Figure 4.2: Timescale separation of liquid dynamics and crystallization. The red curve, τ_liq, gives the temperature-dependence of the structural relaxation time for the supercooled liquid. The black curve, τ_xtl, gives the temperature-dependence of the timescale for crystallization. The symbol Δ denotes the difference in timescales between liquid dynamics and crystal formation at the boundary temperature of liquid metastability. Temperatures at which the supercooled liquid state is no longer metastable are shaded gray.

4.1.3 Polycrystallinity

Materials such as ice, iron, and many other inorganic solids exist as polycrystalline solids in nature, meaning the solid does not consist of a single crystal. When a nascent crystal forms in a liquid, it is comprised of ordered molecules with a particular orientation. However, there can be many independent nucleation events throughout the liquid, and the orientations of the crystals need not be the same. When these crystals grow larger and approach other crystals, there is often a mismatch of orientations preventing them from growing together as a single crystal. As a result, numerous crystallites make up the solid, each with its own size and orientation. These crystallites are referred to as "grains," and the interfaces separating them are "grain boundaries," which typically have disordered structure. In this section, we explore the emergence and implications of polycrystallinity in greater detail.

We can think of grain growth in polycrystalline materials as occurring in three stages: (1) nucleation, (2) coarsening, and (3) grain boundary annealing. As discussed in an earlier section, nucleation involves the formation of a nascent crystal; in the case of polycrystalline materials, many nucleation events occur throughout the liquid. Once these nascent crystals form, coarsening takes place. The coarsening process involves the growth of nucleated crystals until they meet other crystallites, likely with mismatched orientations. As mentioned in the above section, the rate of grain growth is dictated by the timescale required for microscopic reorganization, $\nu^{-1}(T)$. At the end of the coarsening stage, the initial microstructure of the material is formed, complete with numerous crystallites in different orientations with the associated grain boundaries. The final stage of crystal growth is controlled by the motion or mobility of these grain boundaries. The crystallites have filled space, but molecules at grain boundaries can reorganize to smooth the boundaries between crystallites, resulting in only modest increases in grain size. Grain boundaries may move and merge with other grain boundaries to give rise to a particular microstructure. Fig. 4.4 illustrates the growth of average crystal size with respect to time for each of the three regimes.

Grain Boundary Structure

Until this point, we have made no mention of the types of orientation mismatch that can occur when grains grow together in the coarsening stage. Here we go into greater detail on the types of grain boundaries actually found in nature. Grain boundaries are typically classified as low-angle grain boundaries (LAGB) or high-angle grain boundaries (HAGB) [79, 80] depending on the degree of orientation mismatch of the grains. LAGBs are interfaces between crystals with small orientation mismatch ($<$ 15 degrees), while HAGBs are interfaces between crystals with large orientation mismatch ($>$ 15 degrees). LAGBs are considered to be interfaces with an array of dislocations, where the energy of the grain boundary is a property of the extent of mismatch of orientations [81]. However, the energy associated with a HAGB is found to be independent of grain orientation, with the grain boundary highly disordered in nature [79].

The mechanical properties of a polycrystalline material are intimately related to the ma-

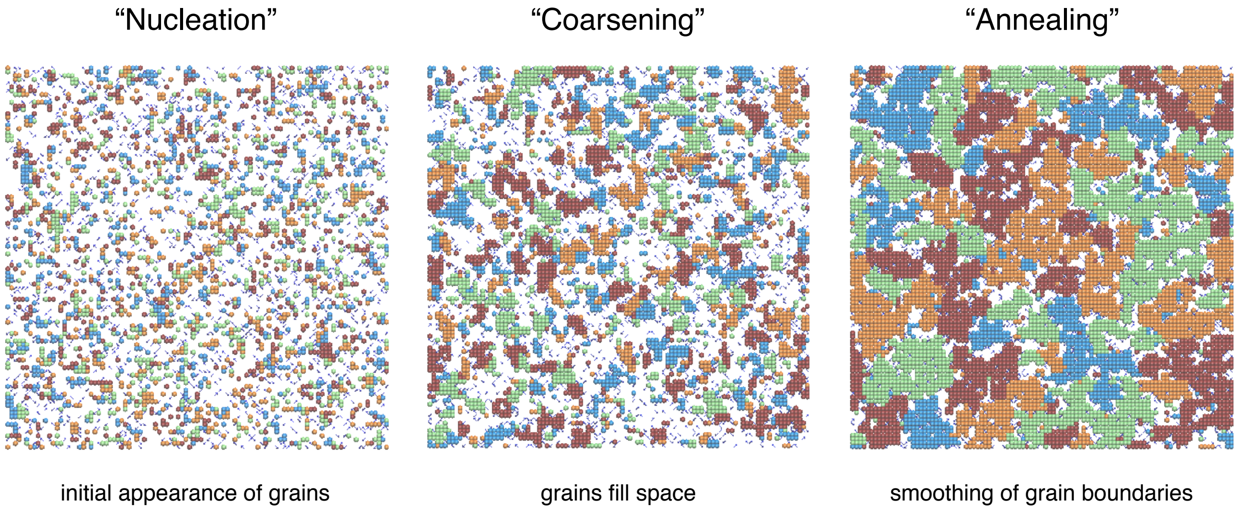

Figure 4.3: Stages of grain growth in a polycrystalline material. The first stage, "nucleation," involves the initial appearance of grains with a variety of orientations throughout the system. The second "coarsening" stage involves the growth of the nascent grains to fill the volume of the system. Once the grains have grown to fill the system, the final "annealing" stage takes place. Molecules at the grain boundaries are able to reorganize such that the grains can continue to grow.

terial's grain structure. One such property is the material-specific yield strength, the amount of stress required to deform the polycrystalline material. Dislocations in a crystal increase the propensity for permanent deformation. Grain boundaries impede the propagation of these dislocations, as there is an energy cost associated with reorienting to align with the adjacent grain [82, 83]. Yield strength therefore increases with decreasing grain size, as a material with smaller constituent crystallites necessarily has more grain boundaries. The Hall-Petch equation [84] relates the average grain size and yield stress of a material

$$\sigma_y = \sigma_0 + \frac{k_y}{\sqrt{d}} \tag{4.4}$$

where σ_y is the yield stress, σ_0 is a material-specific constant, k_y is a material-specific strengthening coefficient, and d is the average grain diameter. Many materials can be made stronger by preparing them in a way that ensures smaller grains. A deeper understanding of how cooling and quenching protocols influence average grain size could prove helpful in the design of materials with specific mechanical properties.

Grain Boundary Dynamics

While the nucleation and coarsening stages of polycrystalline growth are straightforward, the annealing stage warrants further discussion. The mobility of grain boundaries is dependent on the nature of the grain boundaries (for instance, HAGB vs. LAGB), temperature, and stress state. For example, grain boundaries have been found to exist in both smooth

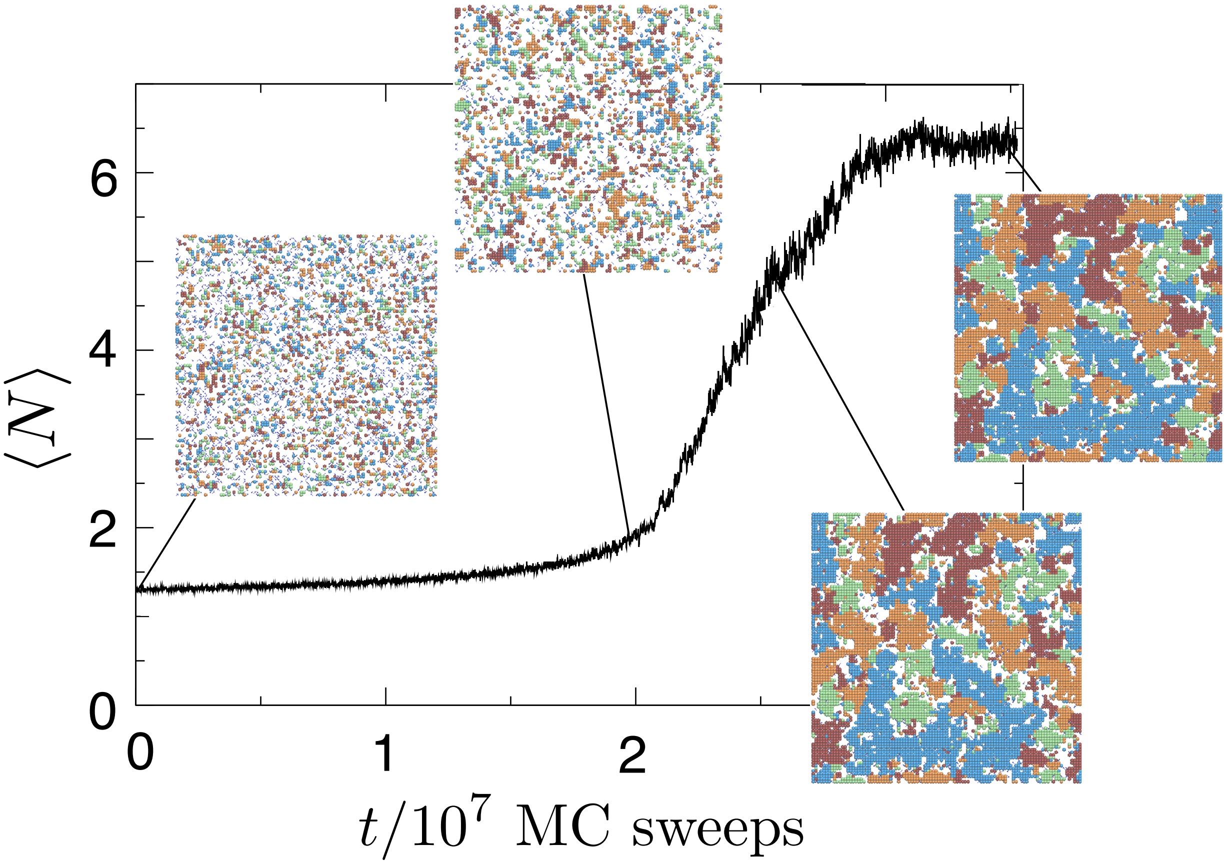

Figure 4.4: Grain growth regimes for a polycrystalline material. The material is cooled at a constant rate from a liquid state to well below its melting temperature. The average grain size $\langle N \rangle$ is plotted over time to illustrate the three grain growth regimes considered in this chapter. Initially, the increase in $\langle N \rangle$ is very gradual, as nascent crystals form during the "nucleation" regime. During the "coarsening" regime, the size of clusters increases relatively quickly, and grains overtake the system. Once the system is polycrystalline, the average cluster size is relatively constant, as regions near grain boundaries rearrange and smooth the grain edges.

and rough states and undergo a roughening transition; the nature of this transition can influence the mobility of the interfaces [85]. It has been suggested that the presence of smooth boundaries significantly impedes the overall grain boundary annealing process in a mesocrystal, such that grain growth stops, and a polycrystalline microstructure is formed [86]. These grain boundaries—particularly HAGBs—can also exhibit glassy dynamics akin to bulk glassy dynamics [87, 88]. Relaxation is then super-Arrhenius, resulting in a significant slowdown of the grain boundary mobility. As in the case of smooth vs. rough grain boundaries, the presence of glassy boundaries can again affect the grain growth significantly, resulting in polycrystalline forms of the material. In this chapter, we consider the effects of glassy grain boundaries on the overall crystal growth process.

4.2 The Arrow-Potts Model

A microscopic model to describe the process of crystallization should incorporate the slowing of liquid dynamics below the melting temperature and should also exhibit polycrystallinity. We utilize the Arrow model as a coarse-grained lattice model of glassy dynamics and combine it with a Potts model, which is capable of forming polycrystalline domains. Coarse-grained lattice models have been used previously to understand liquid-crystal phase transitions [3], as well as the self-assembly of nanoparticle domains [89]. Here we incorporate kinetic constraints of glassy dynamics. We refer to our hybrid model as the "Arrow-Potts model." In the following sections, we detail the components of the basic model and discuss the general types of phenomena our model can exhibit.

4.2.1 The Arrow Model

As a coarse-grained model for supercooled liquid dynamics, the Arrow model [18] incorporates facilitation and directionality, and thus exhibits the same super-Arrhenius growth in relaxation times observed in atomistic liquids.[2] The Arrow model is characterized in Chapter 3 and is briefly summarized here, with minor changes in notation to allow for easier inclusion in our hybrid model.

Each lattice site i in the system has an occupation variable n_i indicating whether the site contains an excitation and is therefore considered "mobile." Each excitation also has an associated direction of facilitation. For a lattice in d dimensions, there are 2^d possible facilitation directions for an excitation, corresponding to the number of corners in a lattice site. In Chapter 3, we assigned d-dimensional vectors ("arrows") to indicate direction; here we combine occupation variable and facilitation direction into a single numerical value. Immobile liquid sites have $n_i = 0$, and mobile liquid sites have $n_i \in \{1, 2, \dots, 2^d\}$, where each state indicates a distinct direction of facilitation.

---

[2] Here we use the $f = 0$ limit of the Arrow model, the hierarchical limit, which corresponds to fragile glass-former dynamics [18].

The facilitation directions of lattice sites have a significant role in Arrow model dynamics. A mobile site can facilitate dynamics in d neighboring lattice sites located in the direction its facilitation arrow is pointing. Excitations with the same facilitation direction as the facilitating site can be created or destroyed at these neighboring sites. The equilibrium concentration of excitations, c_{eq}, is dependent on the system temperature such that as the temperature decreases, so does the number of mobile sites. The value of the equilibrium concentration is

$$c_{\mathrm{eq}} = \frac{2^d}{2^d + e^{J_0/\tilde{T}}} \tag{4.5}$$

where inverse temperature $1/\tilde{T} > 0$ in the Arrow model corresponds to inverse temperature minus the inverse onset temperature of glassy dynamics $1/k_{\mathrm{B}}T - 1/k_{\mathrm{B}}T_{\mathrm{o}}$ in real systems. The parameter J_0 gives the energetic cost of creating an excitation and can be tuned to the parameters of the atomistic system we hope to model, as demonstrated in Chapter 3. In this chapter we present results for a general Arrow-Potts model, and so our specific choice of J_0 is not critical.

4.2.2 Potts Models

A Potts model [90] is a multi-state generalization of the Ising model, and so we motivate our discussion of Potts models with a mapping from the more familiar Ising model. The general form of the Hamiltonian for an Ising model of N spins is

$$\mathcal{H}^{(\mathrm{I})} = -\sum_{\langle i,j \rangle} J_{ij}^{(\mathrm{I})} x_i x_j - \mu \sum_{i=1}^{N} h_i x_i \tag{4.6}$$

where $J_{ij}^{(\mathrm{I})}$ gives the energetic interaction between sites i and j, $x_i = \pm 1$ is the value of the spin at site i, μ is the chemical potential of the system, and h_i is the magnetic field acting upon the spin at site i. The first sum is over all pairs of nearest-neighbor lattice sites i and j, where a d-dimensional lattice site has $2d$ nearest neighbors. Often the model is simplified so that each site is equivalent by substituting $J^{(\mathrm{I})} \equiv J_{ij}^{(\mathrm{I})}$ and $\mu H \equiv \mu h_i$ for all i, j. The magnetization of the system is defined as

$$\langle M \rangle = \sum_{i=1}^{N} \mu x_i \tag{4.7}$$

and is equal to zero at high temperatures, where the system is in a disordered state with equal proportions of up spins and down spins, on average.

When $J^{(\mathrm{I})} > 0$, it is energetically favorable for neighboring spins to be aligned. For this choice in coupling constant, and for lattices in dimensions $d \geq 2$, the Ising model exhibits an order-disorder phase transition. Even in the absence of a magnetic field, spontaneous magnetization from $|M| = 0$ to $|M| > 0$ occurs for low enough temperatures and high enough

$J^{(\mathrm{I})}$. Nearest-neighbor interactions mediated by $J^{(\mathrm{I})}$ induce long-range correlations over macroscopic distances. The order-disorder phase transition occurs at a critical temperature T_c, which is dependent on both the value of $J^{(\mathrm{I})}$ and the lattice dimension. Below T_c, there is a first-order phase transition between the spin-up state and the spin-down state when the strength of an external field is varied. Fig. 4.5 illustrates the phase transitions that occur in the Ising model.

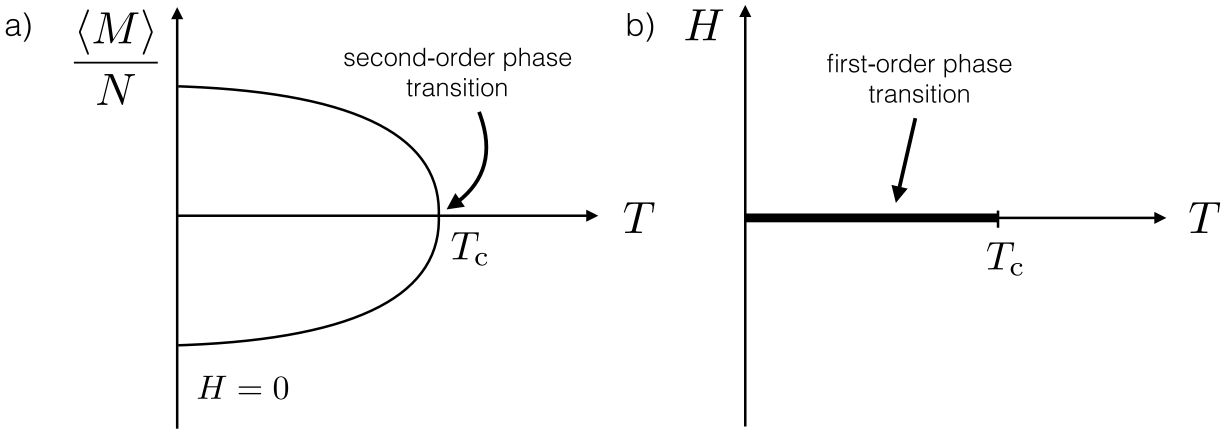

Figure 4.5: First and second order phase transitions in the Ising model. (a) An order-disorder phase transition occurs at $T = T_\mathrm{c}$. In the absence of an external field ($H = 0$), the system will spontaneously magnetize to either $\langle M\rangle/N > 0$ or $\langle M\rangle/N < 0$. When $T = 0$, $\langle M\rangle/N = \pm 1$. (b) Below T_c, at $H > 0$, the system is in a phase with $\langle M\rangle/N > 0$, which tends to $\langle M\rangle/N = 1$ as $T \to 0$. At $H < 0$, the system is in a phase with $\langle M\rangle/N < 0$, which tends to $\langle M\rangle/N = -1$ as $T \to 0$. There is a first-order phase transition between these two phases at $H = 0$.

The Ising model is equivalent to a two-state Potts model. A general Potts model Hamiltonian with an external field $h^{(\mathrm{P})}$ applied to sites in a state k can be written as

$$\mathcal{H}^{(\mathrm{P})} = -J^{(\mathrm{P})} \sum_{\langle i,j\rangle} \delta_{s_i,s_j} - h^{(\mathrm{P})} \sum_{i=1}^{N} \delta_{s_i,k} \tag{4.8}$$

where s_i is the Potts state of site i and $J^{(\mathrm{P})}$ denotes the coupling constant for neighboring sites in the same Potts state. In a two-state Potts model, we let $k \in \{0, 1\}$. We can show the isomorphism between the two lattice models by writing a correspondence between Ising and Potts variables in Eqns. 4.6 and 4.8

$$x_i x_j \equiv 2\delta_{s_i,s_j} - 1 \tag{4.9}$$

and substituting into Eqn. 4.6. We find that the models are equivalent within a constant factor with the mappings $J^{(\mathrm{P})} = 2J^{(\mathrm{I})}$ and $h^{(\mathrm{P})} = 2\mu H$.

Like the Ising model, Potts models also undergo phase transitions. A two-state Potts model is equivalent to the Ising model and therefore has a continuous order-disorder transition in the limit of zero applied field. In Potts models with at least four states in two dimensions, and three states in three dimensions, there is instead a first-order phase transition [83, 90]. As the liquid-crystal transition is also first-order, we are interested in mapping this first-order Potts transition to the liquid-crystal transition for a material of interest.

For inclusion in the Arrow-Potts model, we choose $2^d + 1$ Potts states for a d-dimensional lattice. The state $s_i = 0$ indicates that lattice site i is a liquid, while $s_i \in \{1, 2, \ldots, 2^d\}$ indicates that the site is a crystal in one of 2^d orientations. While in atomistic systems, the orientation of a crystal is a continuous value, we constrain the orientations in our model to a number of discrete values in order to simplify our analysis.[3]

Studying Polycrystallinity with Potts Models

Potts models are frequently utilized to study grain growth in polycrystalline materials over relatively short time scales [92, 93, 94, 95]. Such computer experiments are typically performed by choosing an existing grain structure as the initial configuration and then analyzing the evolution of grain sizes and boundaries over the course of a simulation. While this analysis can be valuable, it is limited in that it lacks information on how the grains and boundaries are formed in the first place. Furthermore, in the absence of kinetic constraints the dynamics of the grain boundaries are essentially unhindered, and so the timescale over which the Potts model falls into the thermodynamically favored single crystal state is much shorter than what is observed in experiments. Fig. 4.6 shows the grain structure of a simulated $d = 2$ Potts model over time, where each color represents a distinct crystal orientation. The first frame shows a grain structure with a variety of grains of different sizes. As time progresses to the middle frame, the grains become larger because neighboring crystals that are aligned are energetically favorable. Eventually, due to the lack of kinetic constraints, a single grain (likely with small defects) overtakes the system. Studying polycrystallinity with only Potts models is clearly limited, but the addition of kinetic constraints effectively arrests the growth of crystal domains over long times.

4.3 Model Thermodynamics

In this section, we discuss the Hamiltonian for the Arrow-Potts model and describe the required parameters for specifying the model's behavior. We derive a mean field theory to identify the first-order phase transition and construct a liquid-crystal phase diagram for a set of model parameters. This phase diagram is then compared with Potts model simulations.

---

[3] In a Potts model where lattice sites have continuous orientations and interaction energies depend on these orientations, there will be no first-order phase transition in $d = 2$ due to the presence of Goldstone modes [91].

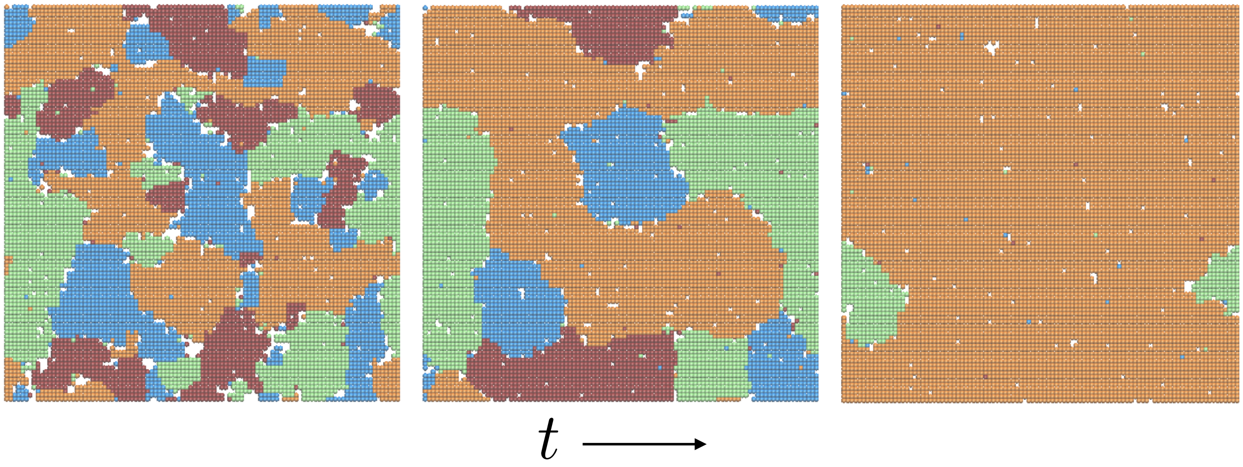

Figure 4.6: Evolution of a $d = 2$ Potts model configuration. Three snapshots from a Potts model simulation are shown, where each color represents a distinct crystal orientation. Initially, there are many grains of a variety of sizes. Over time, larger grains dominate because aligned crystal sites are energetically favorable. Eventually, a single grain (with small defects) overtakes the system.

4.3.1 Hamiltonian

When determining the energetics of a model to describe both glass formation and crystallization, there are several essential parameters. First, we need to incorporate the energy scale for hierarchical dynamics in glassy liquids. This energy scale, along with the temperature, dictates the concentration of mobile regions in the system. Second, we need to include a liquid-solid surface tension and grain boundary energy (i.e., the energetic penalty for misaligned crystals). Finally, we must include a temperature-dependent field that drives the system towards or away from the crystalline state. For example, the model should prefer to be a liquid at temperatures above the melting temperature T_{m} and a solid at temperatures below T_{m}; this preference must become stronger as the temperature moves further away from T_{m}. With these requirements in mind, we define an Arrow-Potts Hamiltonian

$$\begin{aligned}\mathcal{H} = -\frac{\Delta\epsilon}{2}\sum_{\langle ij\rangle}\Big[(1-\delta_{s_i,0})\delta_{s_j,0} + (1-\delta_{s_j,0})\delta_{s_i,0}\Big] - \epsilon\sum_{\langle ij\rangle}\delta_{s_i,s_j} + h(p,T)\sum_i \delta_{s_i,0} \\ + J_0\sum_i(1-\delta_{n_i,0}) + \sum_i C[s_i,n_i]\end{aligned} \tag{4.10}$$

where $s_i \in \{0, 1, ..., 2^d\}$ represents the Potts model state of site i and $n_i \in \{0, 1, ..., 2^d\}$ the Arrow model state. The Potts state $s_i = 0$ corresponds to a liquid, and states $s_i = 1, ..., 2^d$ correspond to crystals in 2^d different orientations. Similarly, the Arrow model state $n_i = 0$ is an immobile liquid, and states $n_i = 1, ..., 2^d$ are mobile with one of 2^d distinct facilitation directions. The sum over $\langle ij\rangle$ denotes a sum over nearest neighbor sites. The $C[s_i, n_i]$ term in Eqn. 4.10

$$C[s_i, n_i] = \begin{cases} \infty, & \text{if } s_i \neq 0,\ n_i \neq 0 \\ 0, & \text{otherwise} \end{cases} \tag{4.11}$$

enforces the constraint that if a lattice site is a crystal, it cannot facilitate mobility in neighboring sites. The Kronecker delta function is defined as

$$\delta_{p,q} = \begin{cases} 0, & p \neq q \\ 1, & p = q \end{cases} \tag{4.12}$$

where p and q represent state variables in our model.

The parameter $\Delta\epsilon$ in Eqn. 4.10 defines the interaction energy between neighboring liquid and crystal sites and thus reflects the value of the liquid-crystal surface tension. The parameter ϵ sets the interaction energy between two neighboring liquid sites or two neighboring aligned crystal sites. The interaction energy between two misaligned crystals, or grains, is set as the reference (i.e., zero) energy. $h(p,T)$ is the pressure- and temperature-dependent field biasing the system towards or away from the crystal state; this field is equal to the chemical potential difference between the liquid and crystal states at temperature T and pressure p. J_0 sets the energy scale for hierarchical glassy dynamics and is the energy required to create a new excitation in the liquid. As written, Eqn. 4.10 incorporates energy scales for kinetically constrained dynamics at all temperatures and is therefore a physically meaningful expression only when the system is below the onset of glassy dynamics.

We make the approximation that crystal orientations are discrete and choose 2^d as the arbitrary number of possible orientations, where all 2^d crystal states are degenerate in energy. While in reality, crystal orientation is a continuous quantity, choosing discrete values decreases the complexity of our model both analytically and numerically. We also make the simplifying assumption that each pair of misaligned crystals interacts with the same energy. In reality, high- and low-angle grain boundaries, which are defined by degree of misalignment of the two neighboring grain orientations, are associated with different interface energies and grain boundary dynamics (this is described in Section 4.1.3). We ignore any differences in grain boundary energies in the current version of the Arrow-Potts model, but they could be incorporated into the model by introducing additional parameters into Eqn. 4.10.

To study the thermodynamics of the Arrow-Potts model, we write a Potts model Hamiltonian for the system described by Eqn. 4.10 where we average over Arrow states and consider only Potts states. First, we can more succinctly write Eqn. 4.10 as

$$\mathcal{H} = \sum_{\langle ij \rangle} \Big[\Delta\epsilon(\delta_{s_i,0}\delta_{s_j,0}) - \epsilon(\delta_{s_i,s_j}) \Big] + \Big[h(p,T) - d\Delta\epsilon \Big] \sum_i \delta_{s_i,0} + J_0 \sum_i (1 - \delta_{0,n_i}) + \sum_i C[s_i, n_i] \tag{4.13}$$

Note that the representation in Eqn. 4.13 explicitly presents the field $h(p,T) - d\Delta\epsilon$ felt by each liquid site. After integrating out the arrow variables (i.e., n_i variables), we arrive at the Hamiltonian

$$\mathcal{H}' = \sum_{\langle ij\rangle}\Big[\Delta\epsilon(\delta_{s_i,0}\delta_{s_j,0}) - \epsilon(\delta_{s_i,s_j})\Big] + \Big[h(p,T) - d\Delta\epsilon - T\log\big(1+2^d e^{-J_0/T}\big)\Big]\sum_i \delta_{s_i,0} \quad (4.14)$$

where the field felt by liquid sites has been modified. The portion of Eqn. 4.13 relating to glassy dynamics has been absorbed into the liquid field, with the degeneracy in facilitation directions taken into account by inclusion of the 2^d factor. We are left with the Hamiltonian for a Potts model, with no kinetic constraints.[4] As such, we expect the same phase transition as the generic Potts model described in Section 4.2.2, but with a shifted transition on the phase diagram due to the renormalized field. The reduced Hamiltonian $\mathcal{H}'$ enables us to study the thermodynamics of the Arrow-Potts model both analytically and numerically.

4.3.2 Mean Field Approximation

We make use of the Potts model Hamiltonian in Eqn. 4.14 to derive a mean field theory. We start by defining x_k as the fraction of sites in the system with crystal state $k \in \{1,2,\dots,2^d\}$. The fraction of sites in the liquid state x_0 is determined by the values of the crystal fractions because we require $\sum_{k=0}^{2^d} x_k = 1$. With this definition and the Potts Hamiltonian in Eqn. 4.14, we can calculate the average energy and entropy of the system. We find

$$E(p,T) = N\Big[\big(h_{\text{eff}}(p,T) - d\Delta\epsilon\big)x_0 + d\Delta\epsilon x_0^2 - d\epsilon\sum_{k=1}^{2^d} x_k^2\Big] \quad (4.15)$$

and

$$S = -Nk_{\text{B}}\sum_{k=0}^{2^d} x_k \log x_k \quad (4.16)$$

where we define

$$h_{\text{eff}}(p,T) = h(p,T) - T\log(1+2^d e^{-J_0/T}) \quad (4.17)$$

as the effective field acting on liquid sites, for notational convenience. The free energy function $F = E - TS$ is then straightforward to compute

$$\frac{F(p,T)}{N} = \Big(h_{\text{eff}}(p,T) - d\Delta\epsilon\Big)x_0 + \Big(\Delta\epsilon - \epsilon\Big)dx_0^2 - \epsilon d\sum_{k=1}^{2^d} x_k^2 + T\Big(x_0\log x_0 + \sum_{k=1}^{2^d} x_k \log x_k\Big) \quad (4.18)$$

for dimension d, specified parameters ϵ and $\Delta\epsilon$, and values of pressure p and temperature T. For now, we choose arbitrary parameters $\epsilon = 0.46$ and $\Delta\epsilon = 0.37$.[5] We minimize the free energy function to determine the energy basins for our model.

---

[4] Note that the Potts model Hamiltonian in Eqn. 4.14 is not equivalent to the generic Hamiltonian in Eqn. 4.8. In Eqn. 4.14, state $s = 0$ has its own associated energetic interactions and so all Potts states are not degenerate.

[5] We choose $\epsilon > \Delta\epsilon$ so that the favorable energetic interaction between like crystal sites is stronger than the interaction between crystal and liquid, which is in turn stronger than the interaction between two misaligned grains. This is a physically relevant relationship.

The phase diagram is constructed by finding the value of $h(p, T)$ for a specific temperature T such that the free energy of the liquid phase is equal to the free energy of the crystal phase. The crystal phase corresponds to a $x_k = 1$, where $k > 0$ is a single crystal orientation. In the liquid phase, the fraction of liquid in the system x_0 dominates the fraction of any one crystal orientation, but all 2^d crystal orientations exist in equal—albeit very small—fractions $(x_1 = x_2 = \cdots = x_{2^d})$. The amount of crystal with which the liquid phase is enriched depends upon the value of the applied field (y-axis) along the phase transition line. The less negative the field, the more crystal is present in the liquid phase. This is illustrated in Fig. 4.7, which shows the fraction of liquid in the system x_0 as a function of the value of h_{eff} for three temperatures. The first-order phase transition is clearly shown for $\beta = 1.5, 2.5$, but there is no such transition for $\beta = 1$. The symmetry is not broken and crystal exists in equal proportions throughout the path through h_{eff}.

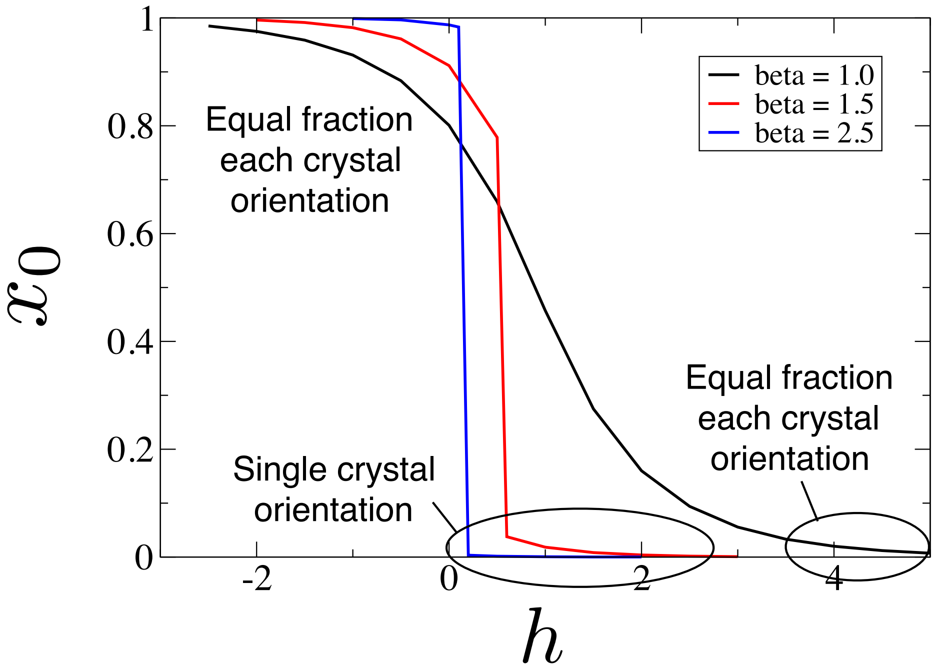

Figure 4.7: Fraction of liquid in $d = 3$ Potts model as a function of applied field and temperature. The fraction of liquid in the system x_0 is plotted as a function of $h(p, T)$ for three temperatures: $1/T = 1$ (black), $1/T = 1.5$ (red), and $1/T = 2.5$ (blue). Sharp transitions from the liquid state (predominantly liquid sites with small amounts of crystal) to the crystal state, where one crystal orientation dominates, are shown for the two lower temperatures. In the absence of a sharp transition to the crystal phase (as is shown for $1/T = 1$), crystal orientations exist in equal proportions.

Figure 4.8 shows the $d = 2$ and $d = 3$ phase diagrams for parameter choices $\epsilon = 0.46$, $\Delta\epsilon = 0.37$, and $J = 1000$ ("mean field" data points). We plot inverse temperature $1/T$ on the x-axis, and the field $[h_{\text{eff}}(p, T) - d\Delta\epsilon]/T$ that is felt by liquid sites on the y-axis. Note

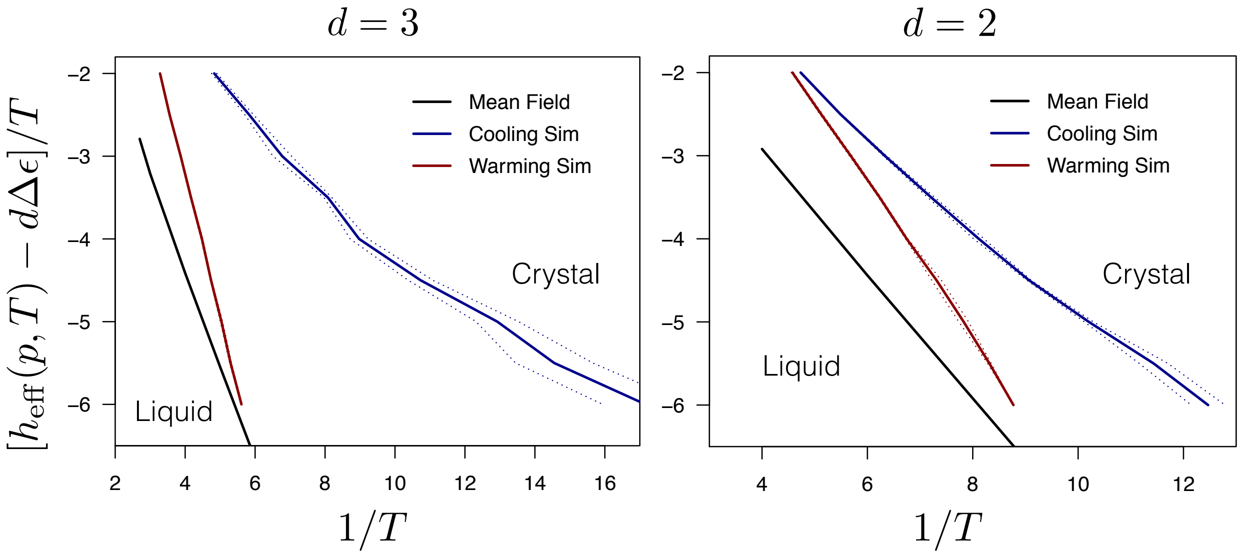

Figure 4.8: Arrow-Potts model phase diagram with mean-field approximation (black) and simulation (red and blue) results. Results for dimension $d = 3$ are shown in the left panel, and results for $d = 2$ in the right panel; note the difference in x-axis scales. The liquid-crystal transition as determined by cooling trajectories is marked with blue lines, where dotted lines indicate one standard deviation from the average of 4 trials. The transition as determined by subsequent warming trajectories is denoted by red lines in order to demonstrate the hysteresis observed in simulations. The liquid phase is located to the left of the phase transition lines in each dimension, at higher temperatures and more negative values of the field (y-axis). The crystal phase is located to the right of the phase transition lines, at lower temperatures and less negative values of the field.

that the dimension d is incorporated into the y-axis value and so a trivial shift between $d = 2$ and $d = 3$ transition lines is expected.

4.3.3 Potts Model Simulation

To test the extent to which the mean field analysis is commensurate with numerical results, we perform Metropolis Monte Carlo simulations[6] of a Potts model with the Hamiltonian in Eqn. 4.14. We require crystal sites ($s_i = 1, 2, \ldots, 2^d$) to first become liquid ($s_i = 0$) before adopting a new orientation.[7] This rule is implemented later in the full Arrow-Potts model and reflects the physical intuition that a crystal must melt before its constituent molecules can reorient themselves.

First, we discuss the nature of the crystal and liquid states in our simulated Potts model. As we observed in the mean-field approximation, the liquid phase consists primarily of lattice sites with $s_i = 0$, but the remaining sites have $s_i = 1, 2, \ldots, 2^d$ in equal and small proportions. Large domains of aligned crystal sites do not form. The crystal state consists almost entirely of aligned crystal sites with some small defects.

We simulate both cooling and warming trajectories to identify the location of the phase transition between liquid and crystal states. Each set of cooling and warming runs has a specific value of $h_{\text{eff}}(p, T)$ at each temperature to correspond with the y-axis in Fig. 4.8; this amounts to horizontal paths across the phase transition line. The system is initialized in the liquid state (all sites i have $s_i = 0$) and equilibrated such that the system composition no longer changes in time. It is then cooled at a rate ν until it crystallizes, i.e., falls into a single crystal state, to the right of the phase transition line. Each of the 2^d crystal phases may be formed with equal probability. The system is then warmed from the crystal at the same rate ν until it melts and once again becomes a liquid.

The temperatures at which the liquid-to-crystal and crystal-to-liquid phase transitions occur, for a specific value of the y-axis of Fig. 4.8, are not equivalent. We observe hysteresis consistent with first-order phase transitions; this is due to the difference in time scales between ordering from a metastable disordered liquid phase (cooling) and disordering from a metastable ordered crystal (warming). This effect grows more prominent at low temperatures in the phase diagram and is illustrated in Fig. 4.9.

Simulation results ("simulation" data points) are shown alongside analytical results in Fig. 4.8, where we present data both from cooling and warming trajectories to construct the Potts phase transition line [96]. The warming trajectory starts from a single crystal state and melts into the liquid state, whereas the cooling trajectory could lead to one of 2^d crystal orientations. The warming trajectory transition is thus a better indicator of the actual transition because no "corrections" of nucleated crystals in opposing directions is needed. This is confirmed by the locations of the warming lines relative to the cooling lines

---

[6] All Potts model and Arrow-Potts model (Section 4.4) simulations are performed using Monte Carlo methods. See Appendix A for a general discussion of the simulation methodology.

[7] Note that this requirement affects only the dynamics (and not the thermodynamics) of the model.

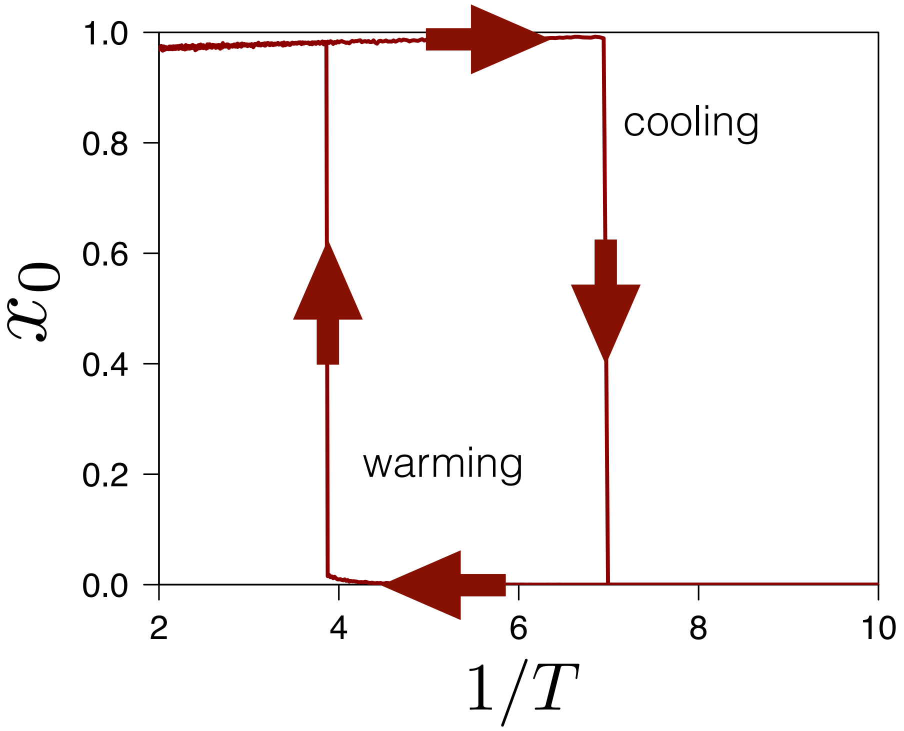

Figure 4.9: Potts model hysteresis for cooling and warming trajectories. The fraction of liquid x_0 is plotted against the inverse temperature $1/T$ for a $d = 3$ Potts model cooled from $1/T = 2$ to $1/T = 15$ and then warmed back to $1/T = 2$. The cooling and warming trajectories are run with a value of $h_{\text{eff}}(p, T)$ such that $[h_{\text{eff}}(p, T) - d\Delta\epsilon]/T$ is constant. Phase transitions from liquid to crystal and crystal to liquid occur at different temperatures for the cooling and warming runs. We keep the phase transition temperature from the warming trajectory for comparison with the mean-field theory.

in the two panels of Fig. 4.8. Overall, the warming simulation and analytical results are in good agreement, though we do expect some deviation because the mean-field analysis neglects fluctuations in the system for temperatures $T > 0$. In the limit of $T = 0$, however, there are no fluctuations and so we expect the mean field result to exactly match simulation. Indeed, Fig. 4.8 shows that the disagreement between warming simulation results and theory decreases with decreasing temperature for both $d = 2$ and $d = 3$. The fact that deviations between cooling simulation results and theory instead *increase* is due to increased hysteresis at low temperatures.

4.4 Simulating the Arrow-Potts Model

Now that we have explored the underlying thermodynamics of the Arrow-Potts model, we discuss the kinetic constraints that are enforced while simulating the model. We also present Monte Carlo simulation results to demonstrate important features of the Arrow-Potts model.

4.4.1 Lattice Initialization

Unless otherwise noted, each Arrow-Potts model simulation is initialized in an equilibrium liquid state at a temperature T just below the melting temperature (as indicated by the phase transition line in Fig. 4.8). State variables are initialized such that each site i has $s_i = 0$, and a value $n_i \neq 0$ is chosen with probability equivalent to the equilibrium excitation concentration c_{eq} for temperature T (Eqn. 4.5), where each of the 2^d facilitation directions is chosen with equal probability ($c_{\mathrm{eq}}/2^d$). All remaining $N(1 - c_{\mathrm{eq}})$ sites are assigned $n_i = 0$. Hierarchical dynamics arises naturally from the dynamical rules for the Arrow model; consequently, there is no onset temperature for the Arrow model above which hierarchical dynamics is absent. The Arrow-Potts model is only a valid description of liquid dynamics below the melting temperature (more precisely, the onset temperature $T_{\mathrm{o}} \approx T_{\mathrm{m}}$) where glassy dynamics is present.

4.4.2 Dynamical Rules

Here, we detail the kinetic constraints arising from the inclusion of the Arrow model and the resulting dynamical rules that must be followed when simulating the Arrow-Potts model. There are three categories of possible states for a lattice site i:

(1) **Mobile (“facilitating”) liquid** with $n_i \in \{1, 2, \ldots, 2^d\}$, $s_i = 0$; can facilitate dynamics or a change in Potts state at neighboring sites according to its direction of facilitation

(2) **Immobile (“non-facilitating”) liquid** with $n_i = 0$, $s_i = 0$; cannot facilitate dynamics

(3) **Crystal** with $n_i = 0$, $s_i \in \{1, 2, \ldots, 2^d\}$; inactive state that cannot facilitate dynamics

The dynamical rules and visual representations of these states are summarized in Fig. 4.10. The three possible states with their respective Arrow and Potts variables are shown in rectangles, with arrows showing allowed transitions between them. Note that a crystal site must first become a liquid before adopting a different crystal orientation. This choice makes intuitive sense, as a molecule must be in a liquid state in order to reorganize and adopt a crystalline structure. In visualizations of the Arrow-Potts models in upcoming sections, we represent immobile liquid sites with empty lattice sites, active liquid sites with arrows

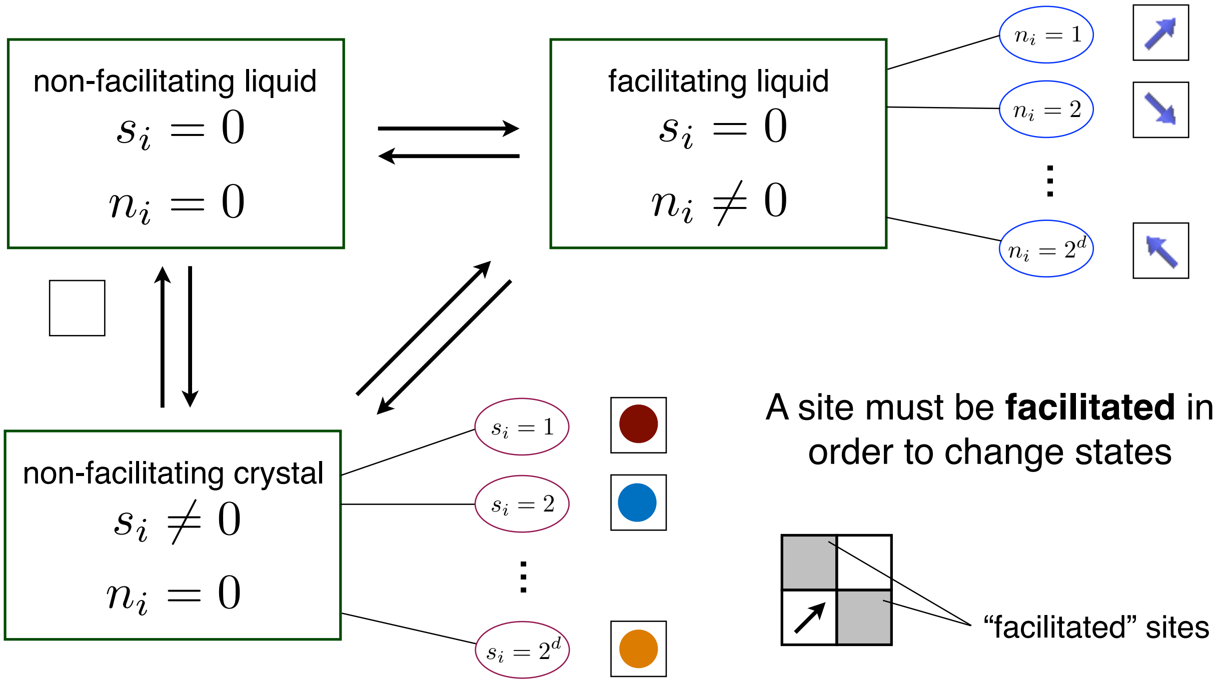

Figure 4.10: Illustration of Arrow-Potts model states and the allowed transitions between them. The three black rectangles represent the immobile (non-facilitating) liquid, mobile (facilitating) liquid, and crystal states with the values of their corresponding Arrow and Potts variables. Arrows denote allowed transitions between them. Note that a crystal site must first become a liquid before adopting a different crystal orientation. We represent immobile liquid sites with an empty lattice site; mobile liquid sites have arrows pointing in the appropriate direction of facilitation, and crystal sites are include spheres colored according to its crystal orientation. In the bottom right of this figure, we show facilitated neighboring sites (shaded gray) for an active liquid site in a $d = 2$ model. Facilitated immobile liquid sites may transition to mobile liquid sites with the same direction of facilitation as the facilitating site. A facilitated mobile liquid site may transition to a crystal of any orientation or to an immobile liquid site only if its direction of facilitation matches that of the facilitating site. A facilitated crystal site may transition to a mobile liquid site with the same direction of facilitation as the facilitating site or an immobile liquid site (no direction of facilitation). Only mobile liquid sites can facilitate dynamics.

pointing in the appropriate direction of facilitation, and crystal sites with spheres in the color corresponding to its orientation. These representations are shown alongside each state in Fig. 4.10.

Each active liquid site has a direction of facilitation, which determines its d nearest neighbors that are dynamically facilitated. Fig. 4.10 (lower right) shows a mobile liquid site with the two neighboring sites that it facilitates. Any site transitioning to a new state must first be facilitated by a mobile liquid site.

4.4.3 Simulation Results

With the dynamical rules of the Arrow-Potts model made clear, we demonstrate the types of behavior our model is capable of exhibiting and the quantities that can be calculated and compared to experimental results. In this section, we show that the timescale for our model to crystallize has a non-monotonic dependence on temperature, which is observed in atomistic systems. We also detail quenching and cooling experiments that reveal distinct average grain sizes depending on the specific preparation of the material. Finally, we discuss the nature of the grain structure in the polycrystalline materials.

Time-Temperature-Transformation Diagrams

In Section 4.1, we describe how the competition between crystallization and vitrification in atomistic materials results in a non-monotonic temperature-dependence of the timescale for crystallization. Here we calculate crystallization and liquid reorganization times as functions of temperature for the Arrow-Potts model and show that our model is capable of exhibiting this same behavior.

The liquid structural relaxation time τ_{liq} is computed by removing Potts dynamics in the system, i.e., by simulating only the Arrow model as is done in Section 3.3. The Arrow model is initialized with an equilibrium concentration of excitations (Eqn. 4.5) corresponding to the temperature at which the model is simulated. The structural relaxation time τ_{liq} is computed by considering the "persistence function" $\langle P(t) \rangle$, a correlation function that expresses the probability that a liquid site has not yet relaxed at time t [64, 65, 66]. A liquid site i is said to relax when the value of n_i changes. The persistence function is described in detail for the Arrow model in Section 3.3 and is only summarized here. $\langle P(t) \rangle$ is computed by averaging over time and over lattice sites, and decays from 1 to 0 as more sites are able to relax. The $1/e$ decay of $\langle P(t) \rangle$ is chosen as the value of τ_{liq}.

We define the crystallization time τ_{xtl} at a specific temperature as the time required for the system to become at least 50% crystal after quenching to that temperature from the liquid state. The Arrow-Potts model is first equilibrated as a liquid just below the melting temperature, where the liquid phase is metastable, and then quenched to a lower temperature at time $t = 0$. At time $t = \tau_{\text{xtl}}$, 50% of the lattice sites are crystalline. This quantity is averaged over 10 quenching experiments. Note that crystal of any orientation counts towards the 50%; kinetic constraints prohibit the formation of a single crystal phase.

Fig. 4.11 shows the temperature-time curves for the Arrow-Potts model with $\epsilon = 0.46$, $\Delta\epsilon = 0.37$, $T_\mathrm{m} = 1$, and $J = 1$. We observe the same non-monotonic temperature-dependence as in atomistic systems, where there is a minimum in crystallization time at moderately supercooled temperatures. This non-monotonicity in the Arrow-Potts model can be understood in terms of the decrease in concentration of active liquid sites as the temperature decreases. Liquid dynamics slows dramatically, and because sites must be facilitated in order to crystallize, so does the growth of crystal in the system.

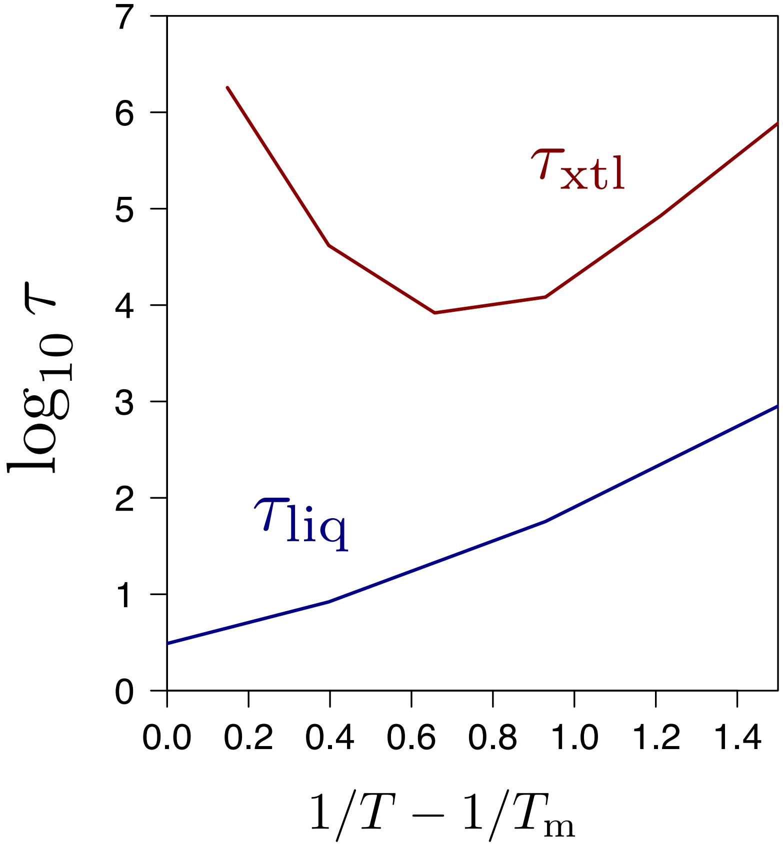

Figure 4.11: Temperature-time plots for liquid relaxation and crystal formation in the Arrow-Potts model. The liquid relaxation curve τ_liq (in blue) is measured as the $1/e$ decay time of the persistence function of liquid relaxation in the Arrow model. The crystal formation time τ_xtl (in red) is computed as the time until 50% of the system consists of crystal domains. The temperature is shifted by the inverse melting temperature $1/T_\mathrm{m}$ for the model.

The liquid relaxation and crystallization curves in Fig. 4.11 are well-separated and do not appear to meet in the low temperature limit. The crystal formation time τ_xtl clearly grows faster than the liquid relaxation time τ_liq at temperatures below the temperature associated with the minimum of τ_xtl. This is a consequence of the fact that the number of pathways by which liquid can relax in the Arrow-Potts model (at low temperatures, where crystal growth is heavily favored) decreases relative to the number of pathways in the Arrow model, due to confinement of the liquid sites between the growing crystal grains. Such confinement slows the diffusion of the liquid, which in turn slows the addition of crystal sites to a growing crystal. Confined liquid sites can be observed in the Arrow-Potts configurations in Fig. 4.12.

Quenching and Cooling Experiments

Depending on the way in which we prepare a polycrystalline material in the Arrow-Potts model, we find different resulting microstructure. That is, the sizes and shapes of grains depend upon the preparation of the material. We demonstrate this using quenching and cooling protocols. Fig. 4.12 shows visualizations of the Arrow-Potts model for three cooling protocols and three quenching protocols. The cooling simulations differ only in the rate at which the system was cooled; we see that slower cooling rates allow for more reorganization and thus larger grain sizes. The quenching simulations differ in the temperatures to which the system was quenched. The deeper the quench, the smaller the resulting grain sizes, as higher temperatures allow for a more active grain boundary annealing process. Fig. 4.13 provides a more quantitative measure of the effect of protocol on resulting grain structure, where we plot the average grain size $\langle N \rangle$ of all grains in the configuration as a function of quench depth and of cooling rate.

In Fig. 4.6, we show frames from a Potts model simulation that has been initialized as a liquid and quenched to a lower temperature at which crystallization is favored. These frames look strikingly different than the Arrow-Potts simulation frames shown in Fig. 4.12. Specifically, the Potts model experiences continuous grain growth and relatively quickly falls into a single crystal energy basin. The Arrow-Potts model, however, forms long-lasting polycrystalline structure that persists for times longer than can be observed over reasonable simulation time scales. Fig. 4.4 illustrates this eventual stagnation of grain sizes during an Arrow-Potts cooling protocol. The difference between these two simulations is the inclusion of kinetic constraints (in the form of the Arrow model) in the Arrow-Potts model; Arrow-Potts dynamics is dependent on the presence of excitations in the amorphous phase. While both models experience the initial nucleation and coarsening stages as described in Fig. 4.3, once the models reach the annealing stage, excitations in the Arrow-Potts model become trapped at grain boundaries. The timescales for motion of these grain boundaries depend on the ability of excitations to connect with each other and relax regions of the system, and so mobility slows significantly. In this way, a polycrystalline microstructure may become effectively “locked” in place.

Such long-lived polycrystalline microstructures are observed in nature, but the cause of arrested grain growth is not well understood. A current proposed mechanism involves characterization of rough and smooth grain boundaries, where grain boundary roughening is concluded to be responsible [86]. Our emphasis on kinetic constraints and glassiness at grain boundaries is a novel explanation for why experimental materials remain polycrystalline even over long time scales.

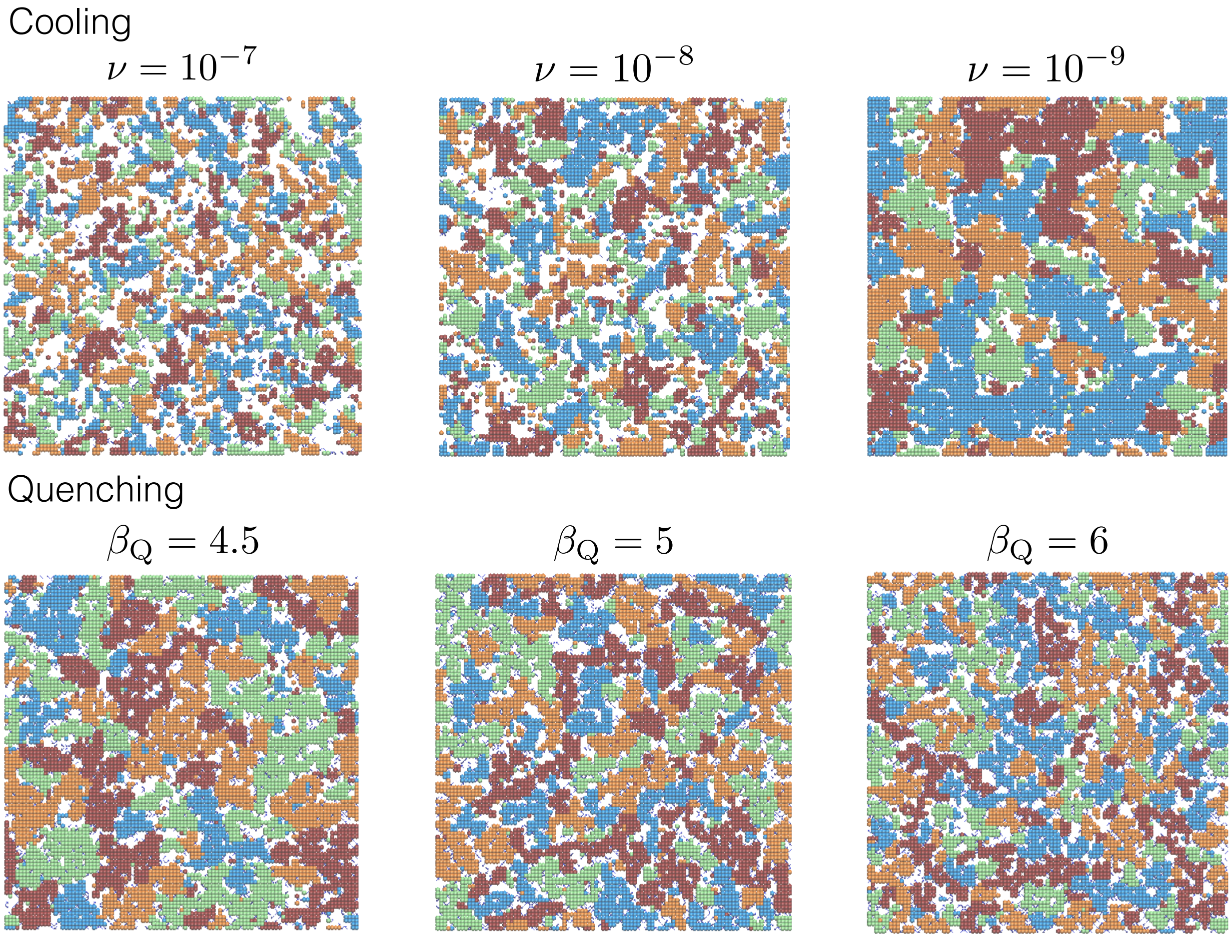

Figure 4.12: Visualizations of cooling and quenching experiments in the Arrow-Potts model. The four colors—blue, green, orange, and red—correspond to four distinct crystal orientations. White sites correspond to inactive liquid, and tiny dark purple arrows denote active liquid sites. In the top panel, the Arrow-Potts model is cooled from $\beta = 2$ to $\beta = 5$ at rates ν over three orders of magnitude. Slower cooling rates result in larger grain sizes. In the bottom panel, the Arrow-Potts model is quenched (i.e., instantaneously cooled) from $\beta = 2$ to three different temperatures β_{Q}. The deeper the quench, the smaller and more irregularly shaped grains. In all six simulations, $\epsilon = 0.46$, $\Delta\epsilon = 0.37$, and $J = 1$.

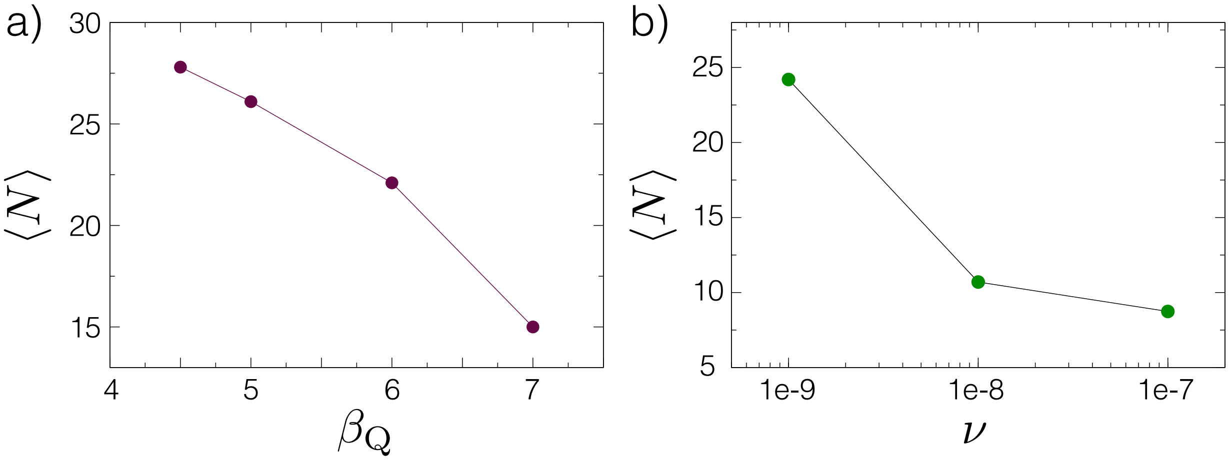

Figure 4.13: Average grain size as a function of quench depth and cooling rate. The average grain size $\langle N \rangle$ is measured as the average number of sites constituting grains in the configuration. A grain is defined as a cluster of nearest-neighbor lattice sites of the same crystal orientation. For all simulations represented in this figure, $\epsilon = 0.46$, $\Delta\epsilon = 0.37$, and $J = 1$. (a) Average grain size $\langle N \rangle$ as a function of quench depth β_{Q}, showing a clear decrease in grain size as the quench depth increases. The model was quenched from $\beta = 2$ was aged until the value of $\langle N \rangle$ no longer changed significantly. (b) Average grain size $\langle N \rangle$ as a function of cooling rate ν, showing a clear increase in grain size at slower cooling rates. The model was cooled from $\beta = 2$ to $\beta = 5$ at a rate ν.

4.5 Model Parameterization

In the above section, we show that the Arrow-Potts model exhibits the same qualitative behavior as atomistic materials. Specifically, the time required for the system to crystallize has a non-monotonic dependence on temperature, and the manner in which the system is cooled below its melting temperature affects the resulting polycrystalline microstructure. However, before we can quantitatively relate simulation results from the Arrow-Potts model to experimental materials, we must parameterize the model with a specific material in mind. In this section we present the parameterization for a generic material for which the relevant properties are known, properties including surface tension and melting temperature. We determine parameters for both the Arrow (J_0, ℓ_0) and Potts (ϵ, $\Delta\epsilon$, h, ℓ) portions of the Arrow-Potts model Hamiltonian (Eqn. 4.10), where ℓ_0 and ℓ denote lattice length scales resulting from the Arrow model parameterization and Potts model parameterization, respectively. At the end of this section, we discuss the case when these length scales are not commensurate.

4.5.1 Arrow Model Parameters

Here we determine the values of the Arrow-Potts model parameters that correspond to supercooled liquid dynamics: the energy scale for excitations on the lattice J_0, and the Arrow model lattice length ℓ_0. We generalize the atomistic system-to-East model mapping described in Ref. [20] for use with two and three-dimensional Arrow models. The required parameters from the atomistic system of interest are the fundamental length scale σ, the energy associated with a displacement of that length J_σ, the onset temperature for glassy dynamics T_o, and the parameter g, which accounts for entropy in relaxation pathways.[8] We utilize the empirically-determined $g_0 = 1.3$ for the three-dimensional Arrow model.[9] We use the equations

$$J_0 = \frac{J_\sigma}{1 + g_0 \ln(\sigma/\ell_0)} \tag{4.19}$$

$$g = \frac{g_0}{1 + g_0 \ln(\sigma/\ell_0)} \tag{4.20}$$

to determine the Arrow model energy scale J_0 and the ratio between fundamental length scales in the material and in the Arrow model σ/ℓ_0. The Arrow model equilibrium excitation concentration is then given in reference lattice units by

$$c_\mathrm{eq}\ell_0^d = \frac{2^d}{2^d + \exp(\tilde{\beta} J_0)}, \qquad \tilde{\beta} = 1/T - 1/T_\mathrm{o} \tag{4.21}$$

(Eqn. 3.21 in Chapter 3). We simulate the Arrow model with the concentration in Eqn. 4.21 to model the material at temperature T, using the specific value of T_o for the material.

4.5.2 Potts Model Parameters

In this section we determine the values of the energies ϵ and $\Delta\epsilon$, the temperature- and pressure-dependent field $h(p, T)$, and the lattice length ℓ required to model a specific material. The parameter $h(p, T)$ corresponds to the difference in chemical potentials of the liquid and solid at pressure p and temperature T and can be approximated for a range of temperatures and pressures. We use linear approximations for chemical potential [97]

$$\mu(T) = \mu(T^*) + \alpha \cdot (T - T^*) \tag{4.22}$$

$$\mu(p) = \mu(p^*) + \eta \cdot (p - p^*) \tag{4.23}$$

where $\mu(T^*)$ is the known chemical potential at a reference temperature T^*, and α is the temperature coefficient for the material of interest (and similarly, for pressure). As of now, we assume standard pressure ($p^* = 1$ atm) and vary only temperature. We can write the chemical potentials separately for liquid and crystal as

$$\mu_\mathrm{xtl}(p^*, T) = \mu_\mathrm{xtl}(p^*, T^*) + \alpha_\mathrm{xtl} \cdot (T - T^*) \tag{4.24}$$

$$\mu_\mathrm{liq}(p^*, T) = \mu_\mathrm{liq}(p^*, T^*) + \alpha_\mathrm{liq} \cdot (T - T^*) \tag{4.25}$$

---

[8] Ref. [20] uses the symbol γ for our g; we use γ later to refer to surface tension.

[9] Chapter 3, Section 3.5.1 gives the procedure used to calculate γ_0 for the Arrow model.

and thus set the field in our model as the difference in liquid and crystal chemical potentials

$$h(p^*, T) = \mu_{\text{liq}}(p^*, T) - \mu_{\text{xtl}}(p^*, T) \tag{4.26}$$

In the following sections, we use surface tension calculations from Potts model simulations to determine the values of the energies ϵ and $\Delta\epsilon$ and the lattice length ℓ. The Arrow-Potts parameters ϵ and $\Delta\epsilon$ reflect the surface tension and grain-grain energies for the material, and so we must ensure that their values are chosen such that the liquid-crystal interface behaves appropriately.

Liquid-crystal interfaces at coexistence may be "rough" or "smooth" [98]. Rough interfaces at coexistence experience interfacial fluctuations that scale as $1/\gamma k^2$, where k is a wavelength and γ is the surface tension; smooth interfaces do not exhibit such scaling. For materials like water, for example, the liquid-crystal interface is rough [99], and so it is important that we choose an Arrow-Potts parameter set such that this interface is represented appropriately. Ising models are known to have both rough and smooth interfaces separated by a "roughening transition" [98, 100], and so we must first identify the rough and smooth interface regimes of the Arrow-Potts phase diagram. We begin by deriving an expression for the capillary spectrum of a fluctuating liquid-solid interface and then find the correspondence between the analytical expression and the results computed from simulation for specific choices of ϵ and $\Delta\epsilon$.

Capillary Spectrum of Soft Interfaces

We describe the fluctuating interface in a three-dimensional system at time t with the relation

$$h(x, y; t) = h_0 + \delta h(x, y; t) \tag{4.27}$$

where h_0 is the average height of the interface, δh is the deviation from the average height, and x and y are spatial coordinates. The Hamiltonian for a system consisting of a soft interface can be approximated as

$$\mathcal{H}[h(x, y)] = \gamma \int\limits_{-L/2}^{L/2} \mathrm{d}x \int\limits_{-L/2}^{L/2} \mathrm{d}y \sqrt{1 + \left(\frac{\partial h}{\partial x}\right)^2 + \left(\frac{\partial h}{\partial y}\right)^2} \tag{4.28}$$

where L is the edge length of the interfacial surface and is assumed to be equal in both x and y dimensions, such that $L_x = L_y \equiv L$. The parameter γ is the surface tension. Given the mean height h_0, the instantaneous height of the interface can be written as

$$h(x, y) = h_0 + \delta h(x, y) \tag{4.29}$$

Substituting Eqn. 4.29 into Eqn. 4.28, we obtain

$$\mathcal{H}[h(x, y)] \approx \gamma L^2 + \frac{\gamma}{2} \int\limits_{-L/2}^{L/2} \mathrm{d}x \int\limits_{-L/2}^{L/2} \mathrm{d}y \left[\left(\frac{\partial \delta h}{\partial x}\right)^2 + \left(\frac{\partial \delta h}{\partial y}\right)^2\right] \tag{4.30}$$

where we assume that fluctuations are small, i.e., $\frac{\delta h}{h_0} \ll 1$, and expand the Hamiltonian to quadratic order in δh. We can write $\delta h(x, y)$ in terms of a Fourier series representation

$$\delta h(x,y) = \sum_{k_m} \sum_{k_n} \delta h_k e^{ik_m x + ik_n y} \tag{4.31}$$

where $k_m = 2\pi m/L$ and $k_n = 2\pi n/L$ are wavevectors in x and y dimensions, respectively. Substituting Eqn. 4.31 into Eqn. 4.30, we obtain

$$\mathcal{H}[h(x,y)] \approx \gamma L^2 - \frac{\gamma L^2}{2}\Bigg[\sum_{k_m}\sum_{k'_m}\sum_{k_n}\sum_{k'_n} \delta h_k \delta h'_k (k_m k'_m + k_n k'_n)\delta(k_m + k'_m)\delta(k_n + k'_n)\Bigg] \tag{4.32}$$

where we use the fact that integrals over x and y are periodic. We see from the Dirac delta functions that $k_m = -k'_m$ and $k_n = -k'_n$, so we can simplify to obtain

$$\mathcal{H}[h(x,y)] \approx \gamma L^2 - \frac{\gamma L^2}{2}\sum_k |\delta h_k|^2 (k_m^2 + k_n^2) \tag{4.33}$$

The approximate partition function for our system is therefore

$$\exp\big[-\beta \mathcal{H}\big] = \exp\big[-\beta\gamma L^2\big] \prod_k \exp\left[\frac{\beta\gamma L^2}{2}|\delta h_k|^2 (k_m^2 + k_n^2)\right] \tag{4.34}$$

and we can calculate the quantity $\langle|\delta h_k^2|\rangle$ by taking the variance of the Gaussian distribution in Eqn. 4.34

$$\langle|\delta h_k^2|\rangle = \frac{1}{\beta\gamma L^2 (k_m^2 + k_n^2)} \tag{4.35}$$

We compare this analytical result with results from Potts model simulations to determine the parameter set that corresponds to a material-specific surface tension.

Capillary Scaling in Simulated Interfaces

In order to correctly model a liquid-crystal interface, we must identify the region of the phase diagram where a stabilized interface has the correct fluctuation scaling. We simulate the $d = 3$ Potts model with a stabilized liquid-crystal interface at coexistence. The system is initialized as a two-component system (liquid and one crystal orientation) with two interfaces due to periodic boundary conditions. We simulate the Potts model with a harmonic constraint on the system composition

$$C_{\text{comp}} = \kappa\left(\sum_j^N \delta_{s_j,1} - N/2\right)^2 \tag{4.36}$$

which is added to the Potts Hamiltonian $\mathcal{H}'$ in Eqn. 4.14, where N is the total number of lattice sites in the model. Eqn. 4.36 ensures that the system is roughly composed of half crystal sites (here, we arbitrarily choose $s = 1$) and prevents one phase from overtaking the system. The value of κ is small, and a range of values can be used without any significant change in results. Fig. 4.14 shows the qualitative nature of the liquid-crystal interface at two different temperatures for the same parameter set. The interface on the left is noticeably smoother than the interface on the right, which is simulated at a higher temperature. We analyze the instantaneous heights of these interfaces and compute the Fourier components [101] to determine whether they obey the correct scaling for rough interfaces. Fig. 4.15 shows the results of these calculations for the interfaces presented in Fig. 4.14. The low-temperature interface clearly does not obey the $1/k^2$ fluctuation scaling derived in Eqn. 4.35; this temperature is below the roughening transition for the model. The higher-temperature interface does have the correct scaling for a rough interface. The Arrow-Potts parameters that yield this scaling behavior are thus valid choices for representing interfaces such as the ice-water interface at coexistence at standard pressure.

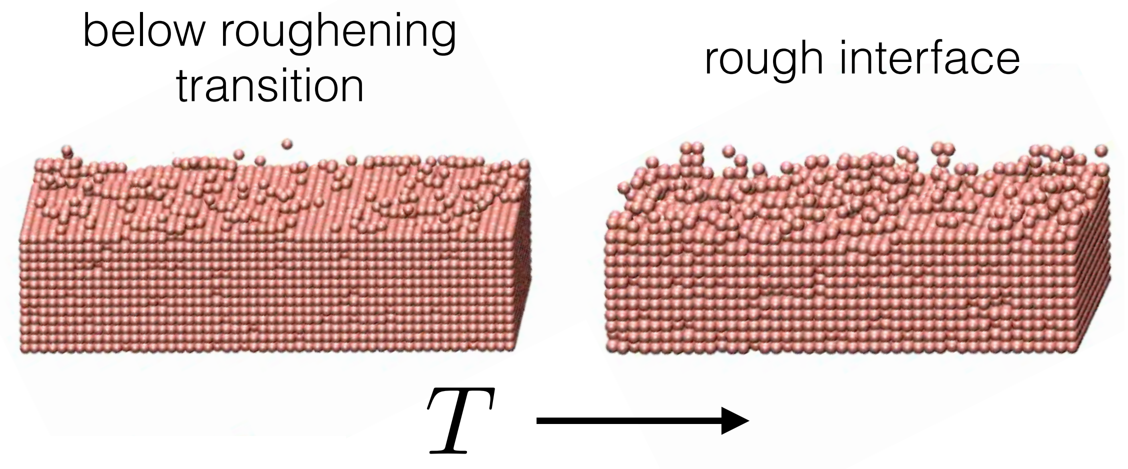

Figure 4.14: Potts model interfaces above and below the roughening transition. Pink spheres denote lattice sites in the crystal phase $s = 1$. The image on the left shows the liquid-crystal interface at $1/T = 3.2$ ($\epsilon = 0.46$ and $\Delta\epsilon = 0.37$). The interface is smooth, and surface fluctuations do not give the $1/k^2$ capillary scaling. The image on the right shows the liquid-crystal interface at a higher temperature $1/T = 2.7$ ($\epsilon = 0.46$ and $\Delta\epsilon = 0.37$). This interface is noticeably rougher than the first, and fluctuations at this interface do exhibit capillary scaling.

Determining Potts Model Parameters from Experimental Surface Tensions

To ensure that the Arrow-Potts model parameterization (namely, ϵ and $\Delta\epsilon$) corresponds to an experimentally-determined surface tension for a rough interface, we fit the data in Fig. 4.15 to our derived capillary scaling expression in Eqn. 4.35. We first discretize the

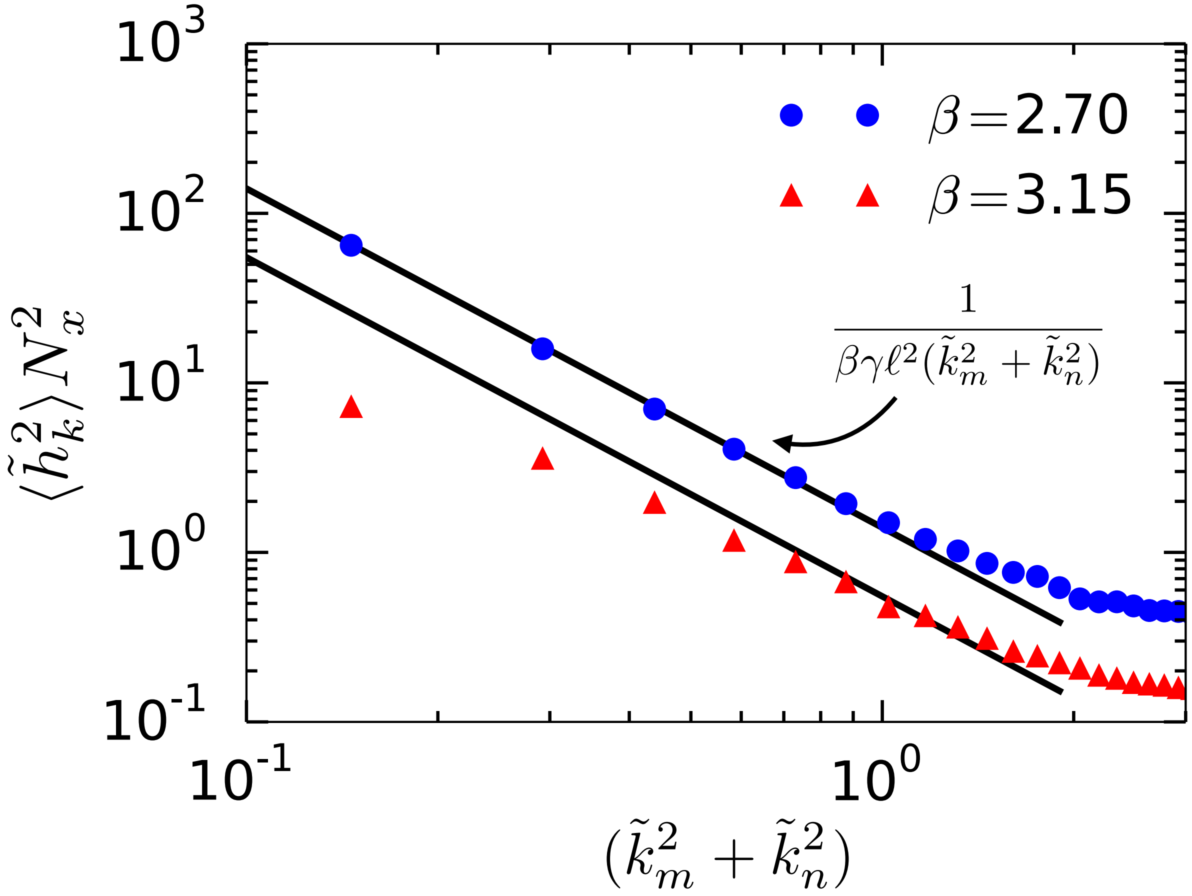

Figure 4.15: Interfacial fluctuation scaling of liquid-crystal interfaces at two temperatures. Interface height fluctuations are plotted versus wavelength k for Arrow-Potts simulations at coexistence at two temperatures, $\beta = 2.7$ (blue circles) and $\beta = 3.15$ (red triangles), for the parameters $\epsilon = 0.46$ and $\Delta\epsilon = 0.37$. Straight black lines indicate $1/k^2$ scaling of rough interfaces; the general equation of the lines is indicated.

Hamiltonian in Eqn. 4.30 to obtain

$$\mathcal{H}_{\text{disc}} = \gamma L^2 - \frac{\gamma \ell^2}{2} \sum_{\langle jl \rangle} (\tilde{h}_j - \tilde{h}_l)^2 \tag{4.37}$$

where

$$\tilde{h}_j = \frac{\delta h(x_j, y_j)}{\ell} \tag{4.38}$$

is a unit-less quantity measuring interfacial height, ℓ is the lattice site length in Angstroms such that $\ell N^{1/3} = L$ in a three-dimensional system, and the sum is over nearest neighbor pairs of lattice sites. We define

$$\tilde{h}_k = \frac{\delta h_k}{\ell} \tag{4.39}$$

such that earlier capillary analysis yields

$$\langle \tilde{h}_k^2 \rangle N_x^2 = \frac{1}{\beta \gamma \ell^2 (\tilde{k}_m^2 + \tilde{k}_n^2)} \tag{4.40}$$

where $\tilde{k}_m = 2\pi m / N_x$, $\tilde{k}_n = 2\pi n / N_y$, and $m, n = 0, \pm 1, \pm 2, \ldots$ are integers. The number of lattice sites N_x and N_y along the edges of the interface are related as $N_x = N_y = N^{1/3}$ for a three dimensional cubic lattice of N sites. $\beta = 1/k_{\text{B}}T$ is the experimental melting temperature in SI units. The fluctuations $\langle \tilde{h}_k^2 \rangle N_x^2$ are plotted versus $\tilde{k}_m^2 + \tilde{k}_n^2$ in Fig. 4.15, where the equation of the lines fit to the data is shown. The quantity $1/\beta\gamma\ell^2$ is the slope of the $\beta = 2.7$ curve (the curve corresponding to a rough interface) in the limit of small $\tilde{k}_m$ and $\tilde{k}_n$. The Potts lattice length ℓ is the length in Angstroms corresponding to a Potts lattice site. The surface tension γ for the material of interest is an experimental value in units of millinewtons per meter. We make the reasonable assumption that the surface tension associated with capillary fluctuations corresponds with the thermodynamic value measured experimentally [100, 102].

4.5.3 Final Parameterization

After following the above procedure, we obtain material-specific values for the following parameters: $J_0, \ell_0, \epsilon, \Delta\epsilon, \ell$. We also find the temperature-dependent field $h(p_0, T)$ acting on the liquid phase at a reference pressure p_0. Note that two of the parameters are length scales ℓ and ℓ_0 from the Potts and Arrow model lattices, respectively. If $\ell \approx \ell_0$, we have a single lattice length for the Arrow-Potts model, and all dynamical rules apply as written in earlier sections. No further parameterization effort is required. If these lattice lengths differ more significantly, however, some compromise in parameter values may be needed to avoid modifying the model. If such a compromise is unrealistic, another option is to consider a case in which the Arrow and Potts lattices are distinct; for example, an Arrow-Potts model in which each Potts lattice site has a specific number (greater than one) of corresponding Arrow lattice sites. This would require implementing new dynamical rules for the crystallization kinetics that we do not discuss here.

4.6 Conclusions and Future Work

In summary, we have introduced a lattice model which incorporates both glassy dynamics and the thermodynamics of a liquid-crystal phase transition to study the formation of polycrystalline materials. The parameters used to construct the model Hamiltonian are representative of experimentally-determined quantities like surface tension, grain-grain energies, and the energy cost of creating a new mobile region in a supercooled liquid, and so can be tuned to model a specific system of interest. In simulations, the Arrow-Potts model exhibits a non-monotonic temperature-dependence of crystallization timescales, consistent with experimental and atomistic simulation results. Furthermore, due to kinetic constraints, our model is capable of forming long-lasting polycrystalline microstructures that reflect the manner it which the polycrystalline material was prepared. Qualitatively similar microstructures are observed in experimental materials. The Arrow-Potts model has the potential to predict resulting grain structures (or types of glass) that are formed for a specific material and cooling protocol.

Section 4.5 presents a general procedure for parameterizing the Arrow-Potts model in order to describe a specific material. In future work, we will carry out this parameterization for liquid water and compare model results to those observed both experimentally and in simulated atomistic models. From Ref. [45], we know the relevant melting and onset temperatures, as well as the parameters needed to describe supercooled water dynamics. With these values, we can follow the parameterization procedure outlined above to simulate the Arrow-Potts model and obtain time-temperature-transformation diagrams that can be directly compared to atomistic water simulation results. We note in Fig. 4.11 that in the high-temperature limit, classical nucleation theory dominates the crystallization timescale curve, while in the low-temperature limit, dynamical facilitation theory of glassy dynamics dominates. Ref. [45] provides an interpolation formula for the τ_{xtl} curve to account for interplay between both theories in the intermediate temperature regime. This formula captures the non-monotonic behavior of τ_{xtl} and is fit to data from atomistic water simulations. We plan to fit this same formula to crystallization times measured from the Arrow-Potts model parameterized for water and compare to the fits to atomistic results.

Chapter 5

Glassy Dynamics in Protein Side-chains

In previous chapters, we characterize lattice models designed to reproduce dynamics observed in atomistic glass-forming liquids. Specifically, the Arrow and Arrow-Potts models exhibit time-correlated and heterogeneous dynamics. While such dynamics is well-known in liquids and kinetically constrained models, one can imagine other similarly dense, jammed-up systems in which it may be present. One such dense system is a folded protein molecule. In this chapter, we explore a biological application of many of the same tools and ideas used to characterize dynamics in glassy materials. This work was completed in collaboration with Gregory Bowman [103].

5.1 Introduction

When attempting to determine structure-function relationships, proteins are often assumed to exist in a single, rigid structure. However, recent experimental and computational work suggests that side-chains in both the core and near the exterior of the protein can sample multiple conformational states, despite their dense surroundings [104, 105, 106, 107, 108, 109]. The mechanism by which such constrained side-chain dynamics occurs, however, remains elusive. In this chapter, we study the side-chain dynamics of interleukin-2, β-lactamase, and RNase H and find that the dynamical events of an individual side-chain dihedral angle are temporally correlated due to the dense environment in a folded protein. For example, Fig. 5.1 shows a time trace of a particular dihedral angle that exemplifies the bursts of dynamics—separated by long periods of immobility—that we observe in all three proteins. This behavior is distinct from dynamics with short memory, and it is suggestive of dynamical heterogeneity within the protein. Indeed, we resolve correlations among different side-chains in the same protein and find that localized clusters of side-chains can be particularly mobile due to underlying structural features. These localized regions of mobility can then facilitate dynamics within neighboring regions of the protein.

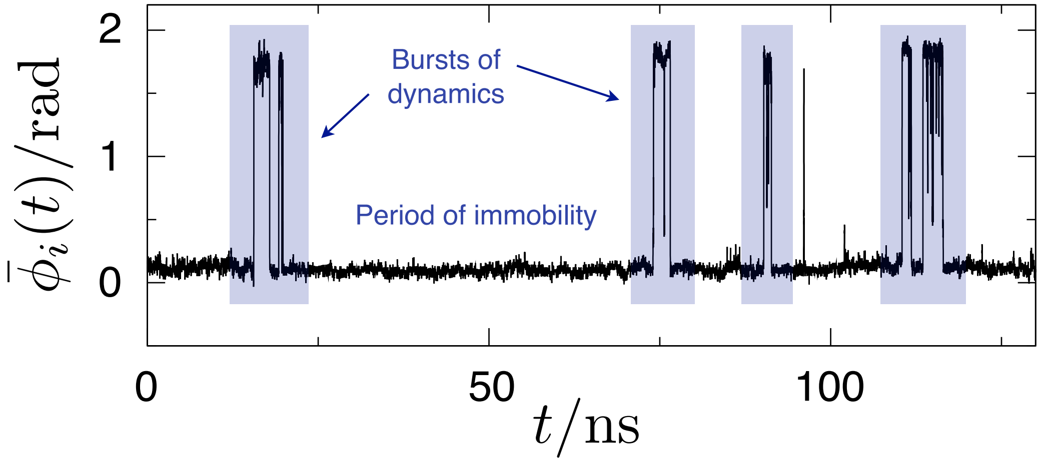

Figure 5.1: Bursts of dynamical activity separated by periods of immobility. An example dihedral angle i, where $\bar{\phi}_i(t)$ denotes $\phi_i(t)$ averaged from time t to time $t+\delta t$, where $\delta t = 1$ ps. The shaded regions call attention to periods in which the dihedral angle rotates several times within a relatively short period of time. These regions are separated by long periods in which there are no rotations.

An understanding of how side-chains move in the dense protein interior is important as side-chain dynamics play a critical role in protein function [110]. For example, communication across certain proteins has been found to proceed by dynamical mechanisms involving side-chain motions within the framework of a relatively rigid backbone [111, 112].

To elucidate side-chain dynamics, we borrow ideas and tools from condensed matter physics. In particular, in densely packed glass-forming liquids, dynamics proceeds via complex and highly correlated mechanisms [10]. Localized soft spots within an otherwise rigid material allow for mobility and facilitate dynamics of neighboring regions. Consequently, particles transition between mobile regimes (wherein they can rapidly undergo many reorganizational events) and immobile regimes (wherein they remain quiescent for an extended period of time). Here, we show that similar temporal and spatial correlations occur within the dense environment of a protein.

5.2 Dihedral Angle Dynamics

We simulate the dynamics of interleukin-2 (IL-2), β-lactamase, and RNase H (structural representations shown in 5.2) for hundreds of nanoseconds to microseconds. The details of these Molecular Dynamics simulations are presented in Appendix A. For each trajectory, we follow the orientation of each side-chain dihedral angle and find that side-chain dihedrals are often in distinct angular states due to steric constraints, with fleeting transitions between these states. We classify large enduring rotations between these states as dynamical events and examine these events for signatures of temporal and spatial correlations. Note that a given protein residue may have zero (e.g., glycine) to four (e.g., lysine) affiliated side-chain dihedral angles. As a result, IL-2 has 273 total side-chain dihedral angles, β-lactamase has 481, and RNase H has 295. The inset in the lower panel of Fig. 5.3 illustrates the meaning of the i^{th} dihedral angle, ϕ_i.

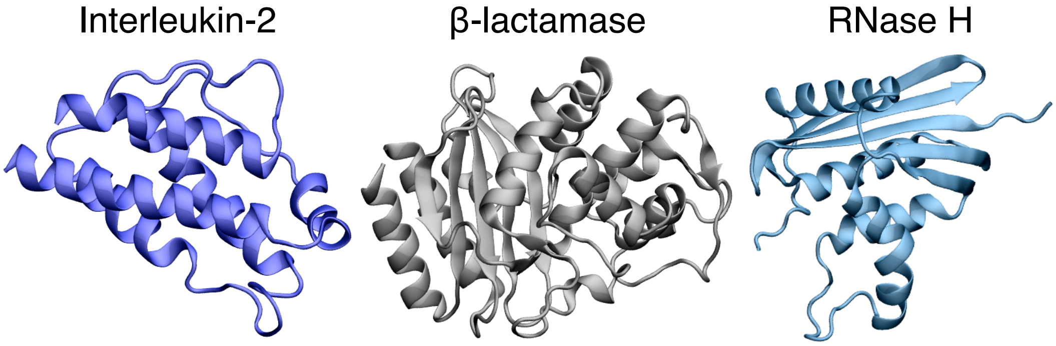

Figure 5.2: Native state crystal structures of interleukin-2 (128 residues), β-lactamase (263 residues), and RNase H (155 residues) in ribbon representations.

5.2.1 Coarse-graining Dynamics Over Time

There is a hierarchy of timescales associated with protein dynamics. Over milliseconds and longer, proteins can undergo significant conformational changes and eventually even unfold. Our focus on dihedral angle dynamics ensures that we study significantly shorter timescales. Atomic vibrations occur much more rapidly, with periods of the order of 10 to 100 femtoseconds. These vibrations do not endure, so we coarse-grain each dihedral angle trajectory $\phi_i(t)$ over time to obtain

$$\bar{\phi}_i(t) = \frac{1}{\delta t}\int_0^{\delta t} dt' \phi(t+t'), \tag{5.1}$$

where $\bar{\phi}_i(t)$ is the value of dihedral angle $\phi_i(t)$ coarse-grained over $\delta t = 1$ ps. The value of this coarse-graining time is large enough to project out most vibrational contributions to the dihedral angle trajectory, leaving only enduring displacements. Side-chain dihedral angles are calculated for all side-chains over the full duration of each protein simulation. Time resolution of the original trajectories is 0.1 ps.

5.2.2 Defining Dynamical Events

In order to identify the times at which such long-lived transitions between angular basins occur for a dihedral i, we utilize a transition function

$$\kappa_i(t) = \Theta[|\bar{\phi}_i(t) - \bar{\phi}_i(t-\Delta t)| - a_i], \tag{5.2}$$

where

$$\Theta(x) = \begin{cases} 1, & x > 0 \\ 0, & \text{otherwise} \end{cases} \tag{5.3}$$

denotes a Heaviside function. Eqn. 5.2 is equal to 1 if a transition of size a_i occurs at time t, and is 0 otherwise. The timescale over which we look for a transition is Δt, and a_i gives the minimum displacement necessary for a dynamical transition for dihedral i. The behavior of Eqn. 5.2 is illustrated in Fig. 5.3.

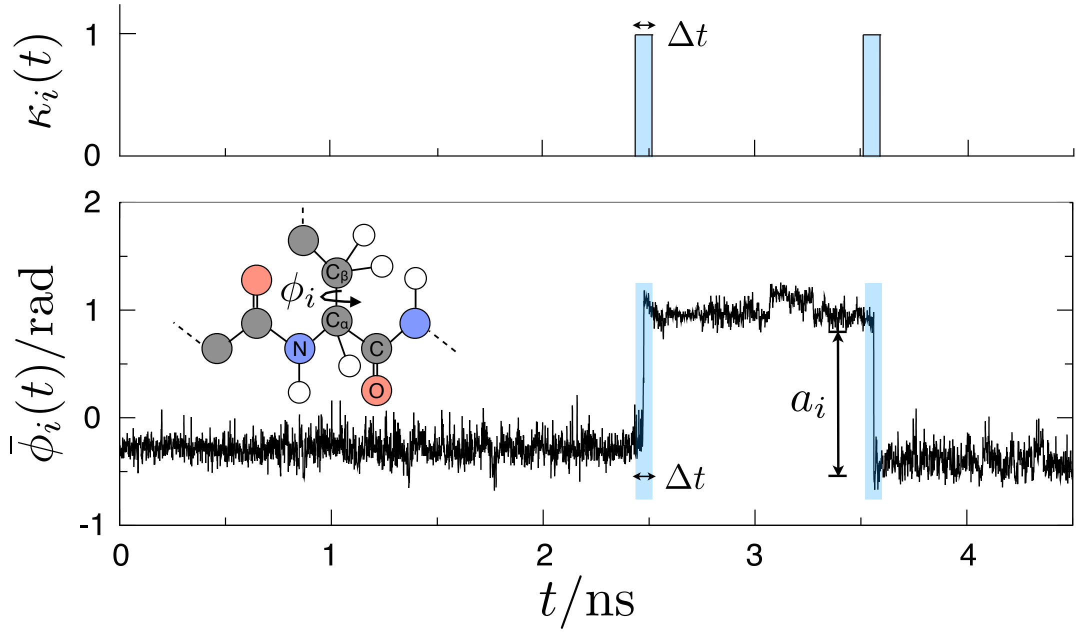

Figure 5.3: Illustration of side-chain dihedral angle analysis. In the lower panel, a sample dihedral angle trajectory for dihedral i is shown in black with dynamical events highlighted in blue. The upper panel gives the corresponding value of the transition indicator function $\kappa_i(t)$, defined in Eqn. 5.2. a_i gives the minimum displacement for a dynamical event, and $\Delta t = 10$ ps is the timescale over which we look for a transition. A protein backbone and side-chain, with a curved arrow to illustrate a rotating χ_1 dihedral angle (denoted ϕ_i), are shown in the inset of the lower panel.

The time window Δt is chosen to be 10 ps, which proves long enough to capture transitions between basins, while still allowing for the accurate determination of transition times. The most important factor in choosing Δt is its relationship to the coarse-graining time. In raw trajectories, transitions between basins occur on timescales of the order of 0.1 ps (the resolution of the trajectories) or faster; after coarse-graining, transitions occur on timescales similar to the coarse-graining time. It is therefore important that Δt be larger than the coarse-graining time. For a coarse-graining time of $\delta t = 1$ ps, the value of Δt was varied between 2 and 50 ps without significantly altering our results.

The value of the transition threshold a_i is specific to each dihedral and is the separation between distinct angular basins. a_i is computed for dihedral angle i as follows: for a given

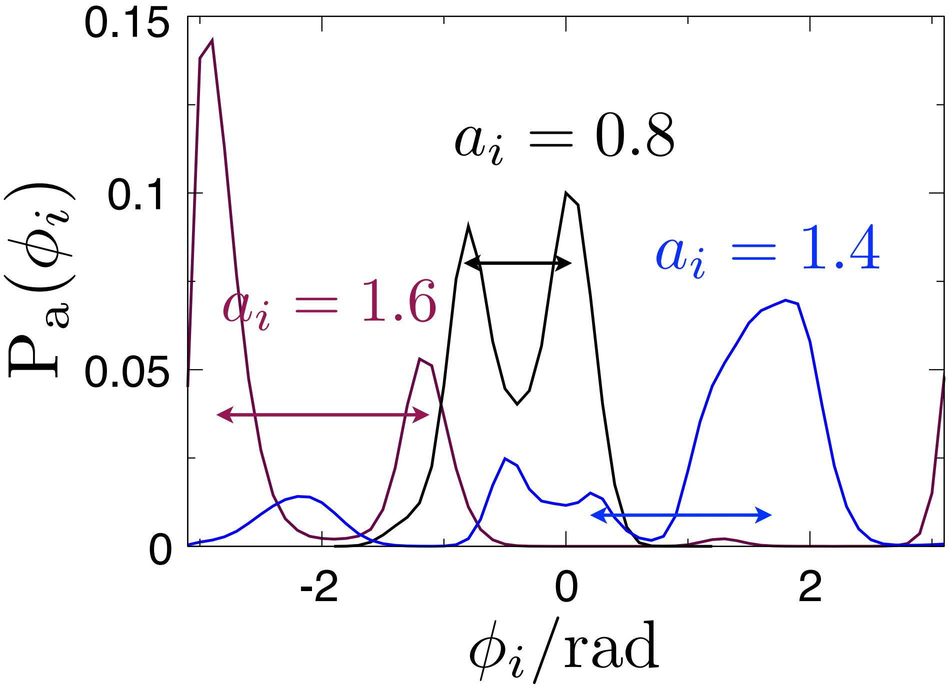

Figure 5.4: Illustration of using angular basins to determine threshold displacement a_i of dihedral i. Distributions for three different IL-2 dihedral angles are shown. The minimum separation between well-separated basins is labeled for each dihedral.

dihedral, the distribution of angles sampled during all trajectories is calculated and the minimum distance between the peaks of any resulting well-separated angular basins is defined as a_i. Two basins are said to be well-separated if the angular probability in between the basins is at most two thirds the probability of the less probable basin being considered. Only dihedral angles sampling more than one angular basin are considered when checking for dynamical transitions; due to the definition of κ_i (Eqn. 5.2), we do not consider as dynamical events fluctuations within these basins. Fig. 5.4 shows representative angular distributions for three dihedrals with the corresponding values of a_i. Typical values are between 0.5 and 3.0 radians.

With the above criteria in place, approximately 5% of IL-2 dihedrals, 23% of β-lactamase dihedrals, and 21% of RNase H dihedrals do not undergo transitions in any of their respective trajectories. These dihedrals are excluded from our analysis except for in Fig. 5.10a, where immobile dihedrals are visualized as dark blue spheres. We expect that most of these immobile dihedrals would undergo transitions if many more trajectories were analyzed. The collection of transition times for each dihedral angle as identified by Eqn. 5.2 is the foundation of subsequent analyses.

5.3 Correlated Intermittent Dynamics

To the extent that the protein dynamics exhibits no significant correlations in time, the time series for $\kappa_i(t)$ in Eqn. 5.2 would be that of a Poisson process. However, examining the pattern of dynamical events—as is shown in Fig. 5.1—reveals that events tend to cluster together in a manner consistent with the time-correlated intermittent behavior seen in glassy systems. Specifically, periods of high mobility consisting of many transitions are generally followed and preceded by relatively long periods of immobility. We refer to the presence of these intermittent bursts of dynamics as “correlated intermittency.” Furthermore, we observe that the degree to which dynamical events are clustered can vary widely between different dihedrals, even within the same protein.

In this section, we quantitatively analyze the degree to which dynamical events are clustered in time. To do so, we employ statistical metrics from the glassy physics literature, namely persistence and exchange times. We begin by providing mathematical definitions for persistence and exchange times, and then we compute these quantities in both native state and unfolded proteins.

5.3.1 Persistence and Exchange Times

To quantify the observed clustering of dynamical events in dihedral angle trajectories, we utilize persistence and exchange times [14, 12]. A persistence time t_p is the waiting time until the next dynamical event within the same side-chain dihedral trajectory, and an exchange time t_x is the time between two consecutive events. Persistence and exchange functions can be expressed in terms of the transition function defined in Eqn. 5.2, where

$$P_i(t', t) = \kappa_i(t' + t) \prod_{t''=t'+\delta t}^{t'+t-\delta t} [1 - \kappa_i(t'')] \tag{5.4}$$

indicates a persistence time $t_\mathrm{p} = t$ given a time origin t', and

$$X_i(t', t) = \kappa_i(t')\kappa_i(t' + t) \prod_{t''=t'+\delta t}^{t'+t-\delta t} [1 - \kappa_i(t'')] \tag{5.5}$$

gives an exchange time $t_\mathrm{x} = t$ for a time origin t'. The main difference between these expressions is that the persistence function considers all possible time origins, whereas the exchange function only considers starting times coinciding with dynamical events. Examples are labeled in the trajectories in Fig. 5.5.

The typical persistence time will be larger than the typical exchange time for a given dihedral if its dynamical events tend to cluster together to yield periods of high and low mobility. The distribution of exchange times for such a dihedral will therefore be distinct, or “decoupled,” from its distribution of persistence times. However, in the absence of time

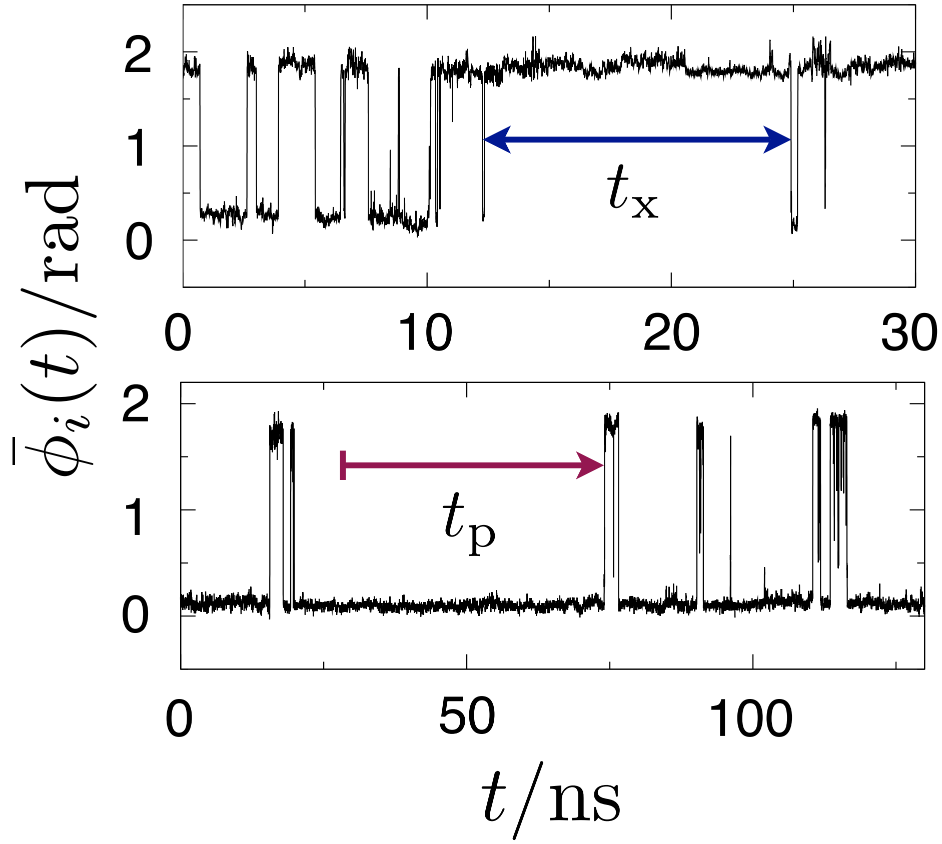

Figure 5.5: Examples of persistence and exchange times in a protein trajectory. Portions of two IL-2 dihedral angle trajectories with an example of an exchange time (top panel) and a persistence time (bottom panel) labeled. There are many more examples of t_x and t_p not shown. The distribution of persistence times is obtained by averaging over all time origins in the trajectory, while the distribution of exchange times is obtained by averaging over all times at which dynamical events occur.

correlations, the distributions will be very similar to one another and will appear to be drawn from a Poisson process.

To look further at the variety of dynamical behavior within the same protein and to compare dynamics among different proteins, we consider the ratio of average persistence time $\tau_{\mathrm{p}}^{(i)} = \langle t_{\mathrm{p}} \rangle_i$ to average exchange time $\tau_{\mathrm{x}}^{(i)} = \langle t_{\mathrm{x}} \rangle_i$ for dihedral i, where the angled brackets denote an average over time origins in all trajectory data for that dihedral. This ratio $\tau_{\mathrm{p}}^{(i)}/\tau_{\mathrm{x}}^{(i)}$ is indicative of the degree to which the intermittent dynamical events of dihedral i are correlated in time, as the average persistence time will be much longer than the average exchange time if the distributions are decoupled. A larger ratio thus indicates greater correlated intermittency, while $\tau_{\mathrm{p}}^{(i)}/\tau_{\mathrm{x}}^{(i)} = 1$ indicates Poissonian dynamics.

5.3.2 Native State Proteins

We compute distributions of persistence and exchange times for each dihedral angle in each of the three folded proteins and find that many dihedrals undergo intermittent bursts of dynamics over their trajectories. Fig. 5.6 shows sets of persistence and exchange distributions for four dihedrals in IL-2, illustrating the variety of dynamical features observed within a single protein. The distributions shown in maroon (χ_1 dihedral of PRO60), green (χ_3 dihedral of MET34), and blue (χ_1 dihedral of LEU113) all show varying degrees of decoupling; each of these dihedrals thus undergoes temporally correlated dynamical events. The persistence and exchange distributions in black (χ_3 dihedral of GLU101), however, almost completely overlap, indicating that the dynamical events of this specific dihedral are uncorrelated in time. While most distributions have a single peak, we do find dihedrals with bimodal distributions.

We calculate the quantity $\tau_{\mathrm{p}}^{(i)}/\tau_{\mathrm{x}}^{(i)}$ for each dihedral i and plot the distributions of ratios found in IL-2 ("Nat. IL-2"), β-lactamase, and RNase H; these are shown in Fig. 5.7. A significant range in ratios is evident for each protein, with the long time tails of the distributions spanning orders of magnitude (note the logarithmic ratio scale).

Persistence and exchange time calculations for each protein utilized all available trajectory data (1.2 μs total data for native IL-2, 200 ns for extended IL-2, 1 μs for both RNase H and β-lactamase). To check the convergence of the ratio $\tau_{\mathrm{p}}^{(i)}/\tau_{\mathrm{x}}^{(i)}$ for each dihedral, we calculate cumulative averages of $\tau_{\mathrm{p}}^{(i)}(T)/\tau_{\mathrm{x}}^{(i)}(T)$ as a function of T, the nanoseconds of trajectory data included in the average. Fig. 5.8 shows cumulative averages for three dihedrals in IL-2. The majority of dihedrals for all three proteins have cumulative averages resembling those of PHE119 χ_2 and LYS49 χ_3, indicating that our results are reasonably converged. However, some dihedrals—such as SER70 χ_1 in Fig. 5.8—have ratios that are still trending upwards, even after over a microsecond of trajectory data. This behavior is expected for dihedrals exhibiting very few dynamical events with a high degree of correlated intermittency; longer trajectories will continue to add longer persistence times, increasing the value of $\tau_{\mathrm{p}}^{(i)}(T)/\tau_{\mathrm{x}}^{(i)}(T)$.

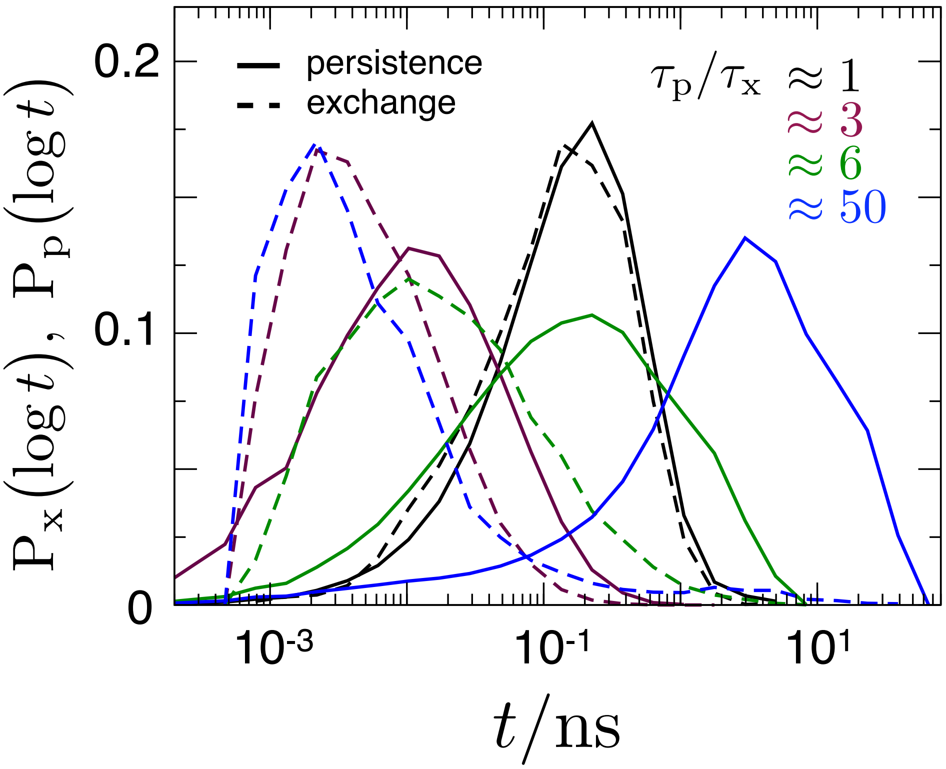

Figure 5.6: Decoupled persistence and exchange time distributions indicate correlated intermittency. Persistence and exchange time distributions (solid and dashed lines, respectively) for four side-chain dihedrals in IL-2, illustrating the variety of side-chain behaviors present in a single protein. The dihedrals shown are GLU101 χ_3 (black), PRO60 χ_1 (maroon), MET34 χ_3 (green), and LEU113 χ_1 (blue). The approximate ratios of mean persistence time to mean exchange time for the GLU101, PRO60, MET34, and LEU113 dihedrals are 1, 3, 6, and 50, respectively, as given in the figure. A greater ratio indicates greater decoupling and thus a higher degree of correlated intermittency.

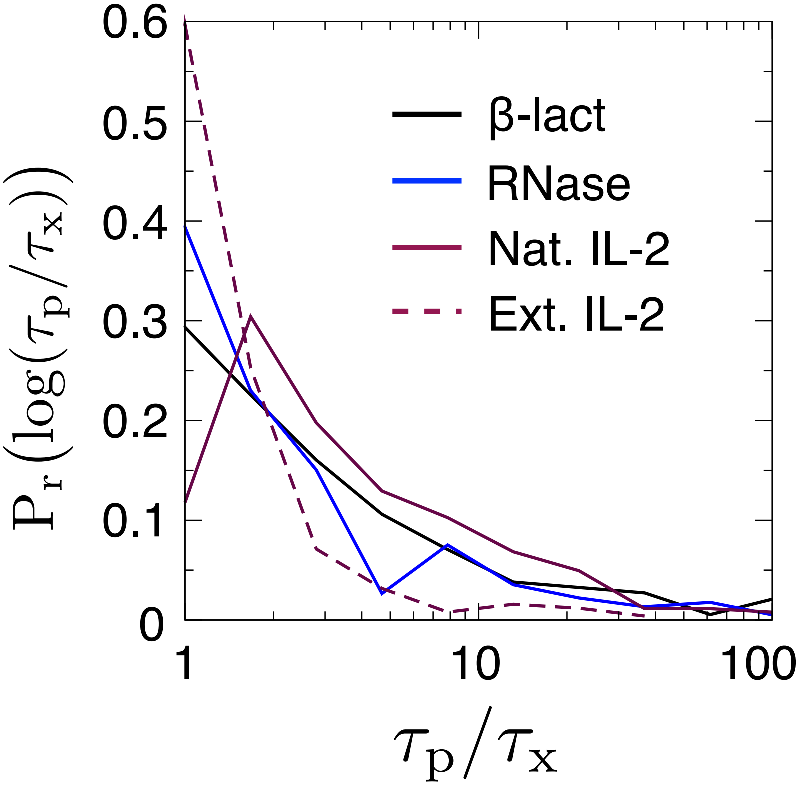

Figure 5.7: Distributions of ratios of average persistence time to average exchange time $\tau_{\mathrm{p}}/\tau_{\mathrm{x}}$ for dihedrals in each protein, including IL-2 in both native (solid line) and extended (dashed line) conformations. β-lactamase, RNase H, and native IL-2 each have a few dihedrals with ratios $\tau_{\mathrm{p}}/\tau_{\mathrm{x}} > 100$, not shown in this plot.

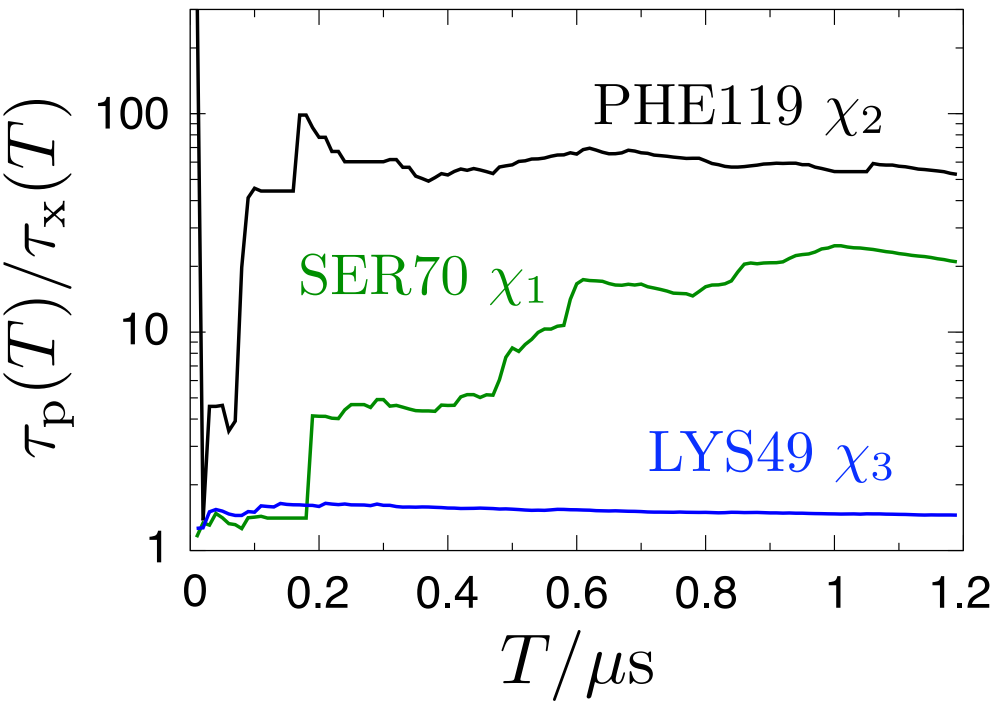

Figure 5.8: Cumulative averages for computing ratios of persistence and exchange times. Sample cumulative averages are shown for three dihedrals (as labeled) in IL-2.

Core Dihedrals

In order to ensure that the correlated intermittent dynamics observed in IL-2, β-lactamase, and RNase H is not only due to particularly mobile side-chains on the exterior of the proteins, we divide protein side-chains into two groups. We analyze dihedrals located in the protein core separately from dihedrals located near the exterior, based on a solvent accessible surface area criterion. Dihedrals of residues with a solvent accessible surface area that exceeds 0.1 nm^2 are said to be exterior dihedrals; all other dihedrals are considered to be within the protein core. Distributions of τ_p/τ_x for IL-2, β-lactamase, and RNase H are shown in Fig. 5.9. We notice that dihedrals can exhibit intermittency regardless of location within the protein. With the exception of IL-2, there are only slight differences in distributions between core and exterior dihedrals. While it is true that surface dihedrals are on average more mobile than interior dihedrals, the presence of correlated intermittency throughout the protein supports previous findings that there can be important dynamics in the dense protein core.

5.3.3 Unfolded Proteins

To determine whether the time-correlated intermittent dynamics described above is a result of the interactions that occur within a folded protein or an inherent property of amino acid polymers, we also simulate and analyze random coils with the same sequence as IL-2.

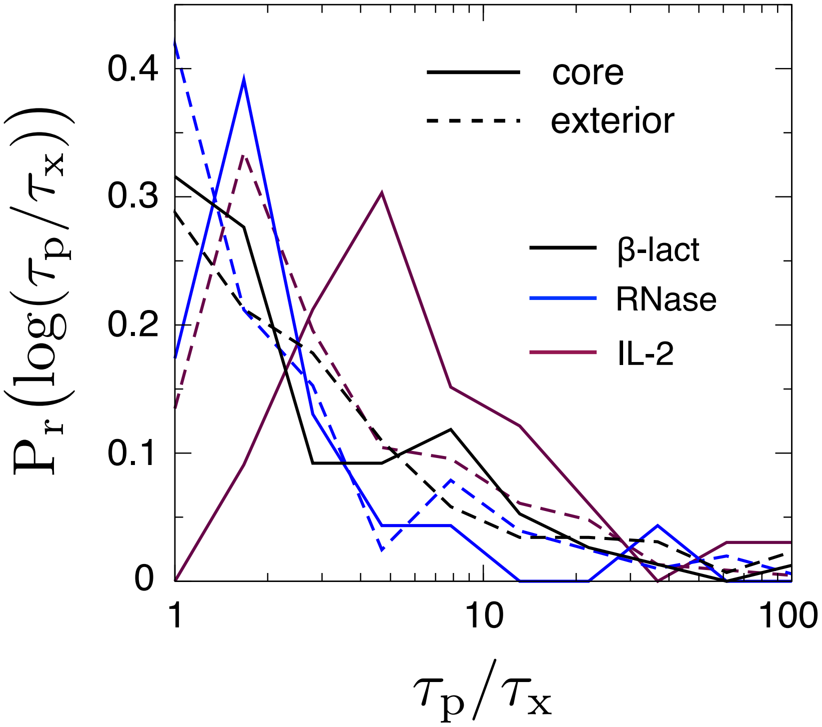

Figure 5.9: Separate analysis of core and exterior dihedrals. Distributions of τ_p/τ_x for core (solid) and exterior (dashed) dihedrals in β-lactamase (black), RNase H (blue), and IL-2 (maroon). Note that because there are a finite number of dihedrals in each protein—a small fraction of which are core dihedrals—a single dihedral may constitute a relatively high fraction of the core dihedral population.

We choose IL-2 to address this question because it has the largest proportion of dihedrals exhibiting correlated intermittency of the three proteins we studied.

We simulate IL-2 in an extended conformation with its backbone atoms fixed by harmonic restraints to prevent portions of the protein from refolding. Although long or bulky side-chains may still interact with their neighbors, this protocol removes many of the interactions that side-chains would experience within a protein core, including interactions with other side-chains and backbone atoms. We analyze the dihedral angle trajectories as outlined in the previous section, and we calculate average persistence and exchange times for each side-chain dihedral. The distribution of ratios $\tau_\mathrm{p}/\tau_\mathrm{x}$ for IL-2 in an extended conformation ("Ext. IL-2") is compared to that of the folded protein ("Nat. IL-2") in Fig. 5.7. We still observe dihedrals with correlated intermittency, but the extended IL-2 distribution lacks the large ratio tail found in that of native IL-2, and the majority of dihedrals have a ratio of approximately 1. This demonstrates that the dihedral dynamics in extended IL-2 exhibit little temporal correlations overall. Any existing intermittent bursts of dynamics are likely due to interactions between neighboring long or bulky side-chains.

To add support to our conclusion that interactions between long or bulky side-chains can give rise to correlated intermittency, we also simulate the dynamics of a much simpler system, a valine tripeptide in explicit water where all atoms are free to move. While the side-chains of the tripeptide are not prohibited from interacting with each other or with the backbone in our simulation, their local environment is exceedingly less constrained than that of dihedrals in a protein core. Persistence and exchange times for the three side-chain dihedrals over a 2 μs trajectory show little evidence of time-correlated intermittent dynamics, with mean persistence to mean exchange time ratios of 1.1, 1.1, and 1.9. Therefore, we conclude that time-correlated dynamics is a result of the substantial excluded volume constraints within a folded protein. Variation in correlated intermittency between the native state proteins as shown in Fig. 5.7 reflect differences between protein folds.

5.4 Facilitated Dynamics in Protein Side-chains

In general, decoupling of persistence and exchange distributions is a characteristic of systems with heterogeneous dynamics, where regions of high mobility exist among regions of low mobility. Spatial correlations within such systems allow for mobile regions to facilitate the mobility of neighboring regions, such that dynamics can eventually extend across the entire system. If such correlations were present in proteins, they could provide a means of transmitting information over long distances (i.e. allosteric communication) [113, 111, 112, 114, 115]. In this section, we apply qualitative and quantitative methods to resolve facilitated, heterogeneous dynamics in protein side-chains.

5.4.1 Visualization of side-chain mobility

Visualization of side-chain mobility in IL-2, β-lactamase, and RNase H suggests the existence of spatial correlations. To resolve correlations, we use dynamical transition times to determine the mobilities of side-chain dihedral angles over portions of trajectories relative to their average mobilities, where much longer trajectories are considered. For a given time t, each dihedral i has a relative mobility value

$$C_i(t) = \frac{1}{\tau\langle\kappa_i\rangle}\sum_{t'=0}^{t}\kappa_i(t'), \tag{5.6}$$

where $\langle\kappa_i\rangle$ gives the average transition rate for dihedral i and is defined as the time average of the transition function (Eqn. 5.2)

$$\langle\kappa_i\rangle = \frac{1}{t_{\mathrm{obs}}}\sum_{t'=0}^{t_{\mathrm{obs}}}\kappa_i(t'). \tag{5.7}$$

If $\langle\kappa_i\rangle = 0$ (dihedral i is immobile over our data), we set $C_i(t) = 0$ for all t. All simulation data is considered when calculating $\langle\kappa_i\rangle$ for each dihedral in each protein. The quantity $\tau\langle\kappa_i\rangle$ gives the expected number of dynamical events over a trajectory of length τ; setting τ thus allows us to look at relative mobilities over trajectories of varying lengths. (If correlated intermittency was absent in the protein of interest, each dihedral would have $C_i(t) = 1$ at time τ.) We normalize by $\tau\langle\kappa_i\rangle$ to resolve mobility that is significant for each dihedral, thus accounting for the structural heterogeneity inherent to proteins.

Dihedrals that are more mobile over the trajectory portion of interest than they are on average have large values of $C_i(t)$. Fig. 5.10 shows frames from 10 ns trajectories of IL-2 and RNase H, where each dihedral i at time t is represented by a sphere and is colored from blue to red while increasing in size, according to its value of $C_i(t)$. Red spheres indicate dihedrals that are more mobile in this portion of the trajectory than they are on average, while the darkest blue spheres represent dihedrals that have not yet moved.

Over the course of the IL-2 trajectory shown in Fig. 5.10, clusters of particularly mobile dihedrals develop across the protein, while other large regions remain essentially immobile. We see correlated regions of mobility and immobility, indicating heterogeneous dynamics. A similar phenomenon occurs in the RNase H trajectory, where mobility starts in the lower right portion of the protein and eventually spreads to the upper half. We do not imply that these regions are consistently mobile; rather, we are simply resolving regions that happen to be mobile over this relatively short portion of a longer trajectory.

5.4.2 Isoconfigurational Averaging

In order to gain insight into how emerging mobile regions facilitate new dynamics across a protein, we invoke the technique of isoconfigurational averaging (ICA) [116] as carried out by

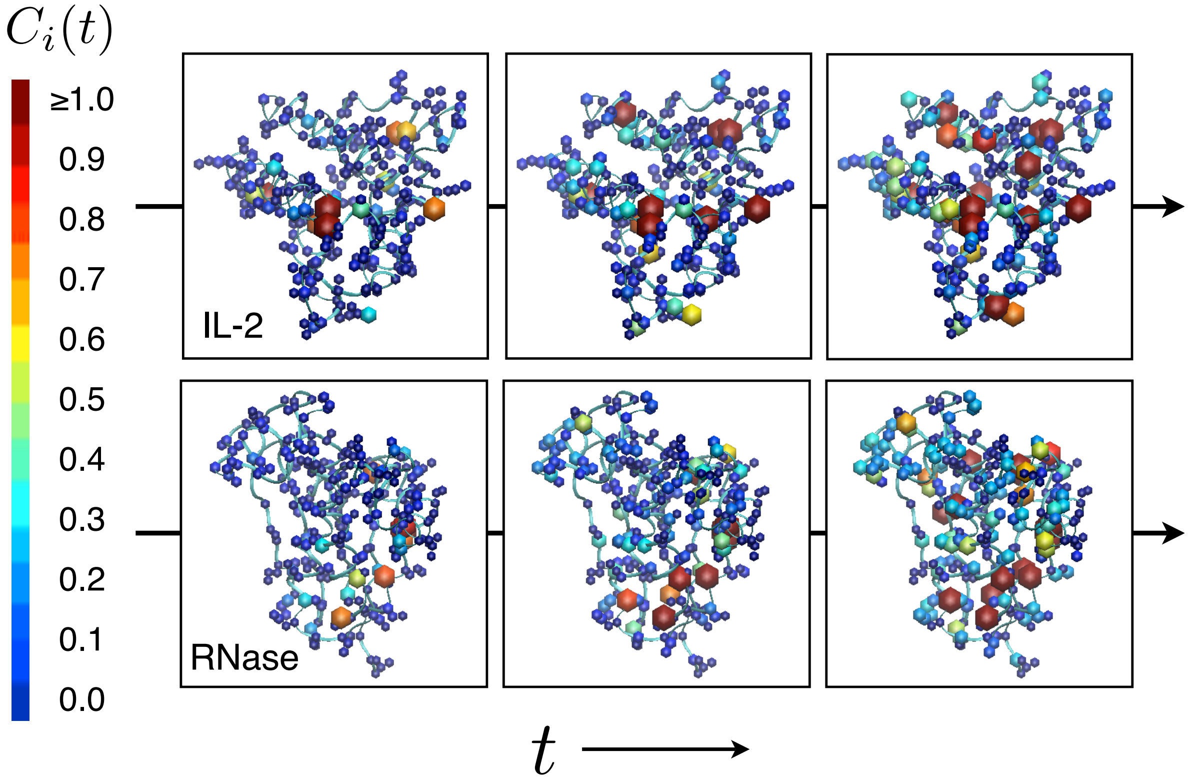

Figure 5.10: Side-chains are dynamically correlated with each other. Snapshots of IL-2 (top three frames) and RNase H (bottom three frames) to highlight the development and spreading of mobile regions over time. Side-chain dihedral angles are depicted by spheres, and the backbone is shown in the background in ribbon representation. A sphere is colored from dark blue to red, while increasing in size, as that specific dihedral becomes more mobile. The color key is shown to the right. We use $\tau = 10$ ns for IL-2, and $\tau = 50$ ns for RNase H. For clarity, all visual representations use fixed atom positions; each sphere is placed at the initial coordinates of a carbon atom determining the axis of rotation for its respective dihedral angle.

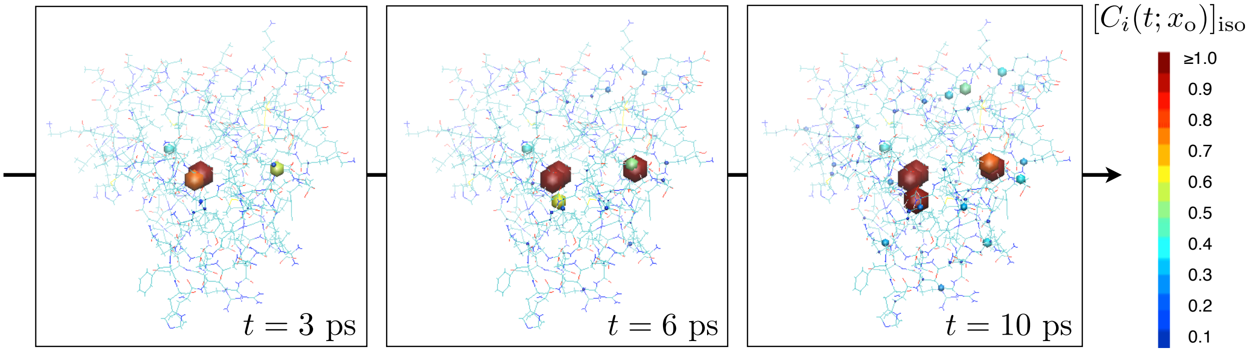

Figure 5.11: Localized regions of IL-2 are mobile due to underlying structural features. We show three snapshots of interleukin-2 along an isoconfigurationally averaged trajectory, where $\tau = 100$ ps. We include data from $M = 1000$ 10 ps trajectories.

Ref. [76]. Many 10 ps simulations are started from the same initial IL-2 configuration with randomized velocities drawn from a 300 K Maxwell-Boltzman distribution, and the mobility $C_i(t)$ of each dihedral i at time t is then averaged over all trajectories. These trajectories are first coarse-grained over time (Eqn. 5.1) to resolve significant dynamical events.[1]

The relative mobility $C_i(t)$ of dihedral i at time t is dependent on its initial position x_o and momenta p_o, so we write

$$C_i(t) \equiv C_i(t; x_\mathrm{o}, p_\mathrm{o}). \tag{5.8}$$

The quantity

$$\begin{aligned} [C_i(t;x_\mathrm{o})]_\mathrm{iso} &= \int \mathrm{d}p_\mathrm{o} \Phi(p_\mathrm{o}) C_i(t;x_\mathrm{o},p_\mathrm{o}) \\ &\approx \frac{1}{M} \sum_{j=1}^{M} C_i(t;x_\mathrm{o},p_j), \end{aligned} \tag{5.9}$$

where p_j is randomly drawn from a 300 K Maxwell-Boltzman distribution $\Phi(p_\mathrm{o})$, is the isoconfigurational average of the mobility for dihedral i at time t, where $M = 1000$ is the number of short trajectories. The initial positions x_o are the same for each trajectory j by definition of ICA. A dihedral that has been very mobile until time t over the majority of these short trajectories will have a large value of $[C_i(t;x_\mathrm{o})]_\mathrm{iso}$, while a dihedral that has been immobile over all collected trajectories has $[C_i(t;x_\mathrm{o})]_\mathrm{iso} = 0$. This technique reveals regions in a specific protein conformation that consistently become mobile due to underlying structural features. ICA averages out contributions from momentum, so any remaining mobility is strictly configurational in origin.

Fig. 5.11 shows a series of pictures of IL-2 resulting from this ICA analysis, utilizing a similar color scheme to what was used in Fig. 5.10, with the exception that immobile

---

[1] In contrast, Ref. [116] uses ICA analysis on short raw trajectories, obscuring any information on meaningful dynamical events.

dihedrals are not represented. We choose a value of $\tau = 100$ ps such that red dihedrals are approximately ten times more mobile than they are on average; this is appropriate for such short trajectories in which it may be rare for a dihedral to move at all. Due to the short length of these ICA trajectories, we use $\Delta t = 2$ ps (Eqn. 5.2) when determining transition times for each dihedral.

The resulting pictures reveal highly localized regions of mobility with dynamical clusters of a few dihedrals. It is significant that mobile dihedrals do not appear at random; new mobile dihedrals are always near previously mobile regions in these snapshots. This is highly suggestive of facilitated dynamics. Certain regions of IL-2 are structurally organized such that side-chain mobility is likely, and dynamics proceeds from these "soft spots" within the dense protein environment.

5.4.3 Mobility Susceptibility

To provide quantitative support for the visualized correlations between dihedrals in the same protein, we utilize a quantity reminiscent of the four-point correlation functions found in the glass literature [73]. We first measure the binary immobility number for dihedral angle i,

$$q_i(t) = \prod_{t'=0}^{t} [1 - \kappa_i(t')], \tag{5.10}$$

which is 0 if the dihedral has undergone at least one dynamical event before time t and is 1 otherwise. Fig. 5.12a shows $q_i(t)$ for an example dihedral trajectory. The time average of $q_i(t)$,

$$\langle q_i(t) \rangle = \frac{1}{t_{\text{obs}}} \sum_{t'=0}^{t_{\text{obs}}} q_i(t'), \tag{5.11}$$

has a unique decay time for each dihedral i, commensurate with its mean persistence time $\tau_{\text{p}}^{(i)}$. This is illustrated in Fig. 5.12b. When $q_i(t)$ is summed over all N dihedrals in the protein (excluding dihedrals that are immobile over the entire course of the trajectory) we obtain a function

$$Q(t) = \sum_{i=1}^{N} q_i(t) \tag{5.12}$$

that decays to zero over time as more dihedrals undergo dynamical events. The decay of the time average of $Q(t)$

$$\langle Q(t) \rangle = \frac{1}{t_{\text{obs}}} \sum_{t'=0}^{t_{\text{obs}}} Q(t') \tag{5.13}$$

is shown in the inset of Fig. 5.12c for IL-2, β-lactamase, and RNase H.

The variance in $Q(t)$ resolves spatial correlations among the dihedrals and peaks at the time of maximum dynamical heterogeneity. There is a contribution to the variance even in the absence of correlations

$$U(t) = \sum_{i=1}^{N} \langle q_i(t) \rangle [1 - \langle q_i(t) \rangle], \tag{5.14}$$

so we consider

$$V(t) = \langle (\delta Q(t))^2 \rangle - U(t), \tag{5.15}$$

which gives the excess variance due to correlations. Fig. 5.12c shows $V(t)/N$ for IL-2, β-lactamase, and RNase H. The larger the peak in $V(t)$, the greater the correlations between different dihedrals in that protein over time t. Fig. 5.12c shows that correlations among dihedrals exist in each protein with unique times of maximum dynamical heterogeneity. We observe two peaks in $V(t)$ for β-lactamase, indicating that dihedrals can be correlated over different timescales even within the same protein.

Our visual and quantitative analysis of spatially resolved side-chain mobility in IL-2, β-lactamase, and RNase H shows that dynamical events of different side-chain dihedrals are correlated and suggests that events at one side-chain facilitate new dynamical events at neighboring side-chains. Such correlations are likely to arise from interactions between side-chains and backbone motion and could enable long-range communication across proteins.

5.5 Conclusions

In summary, our analysis of protein side-chain dynamics in IL-2, β-lactamase, and RNase H reveals that the dynamics of an individual side-chain dihedral can exhibit long time correlations when that dihedral is in a dense environment with other protein residues. Such temporal correlations can be indicative of spatial correlations, and we indeed find localized regions of mobile dihedrals within the protein system. These regions of mobility arise from local structural features of the system, as suggested by isoconfigurational averaging results. These dynamical features are characteristic of glass-forming liquids, but to our knowledge, they have not previously been identified in proteins.

Although dihedrals in all three native state proteins studied here exhibit correlated intermittency and spatial correlations, each protein's dynamical features are unique. This likely reflects inherent differences in tertiary structures and may be related to each protein's specific function.

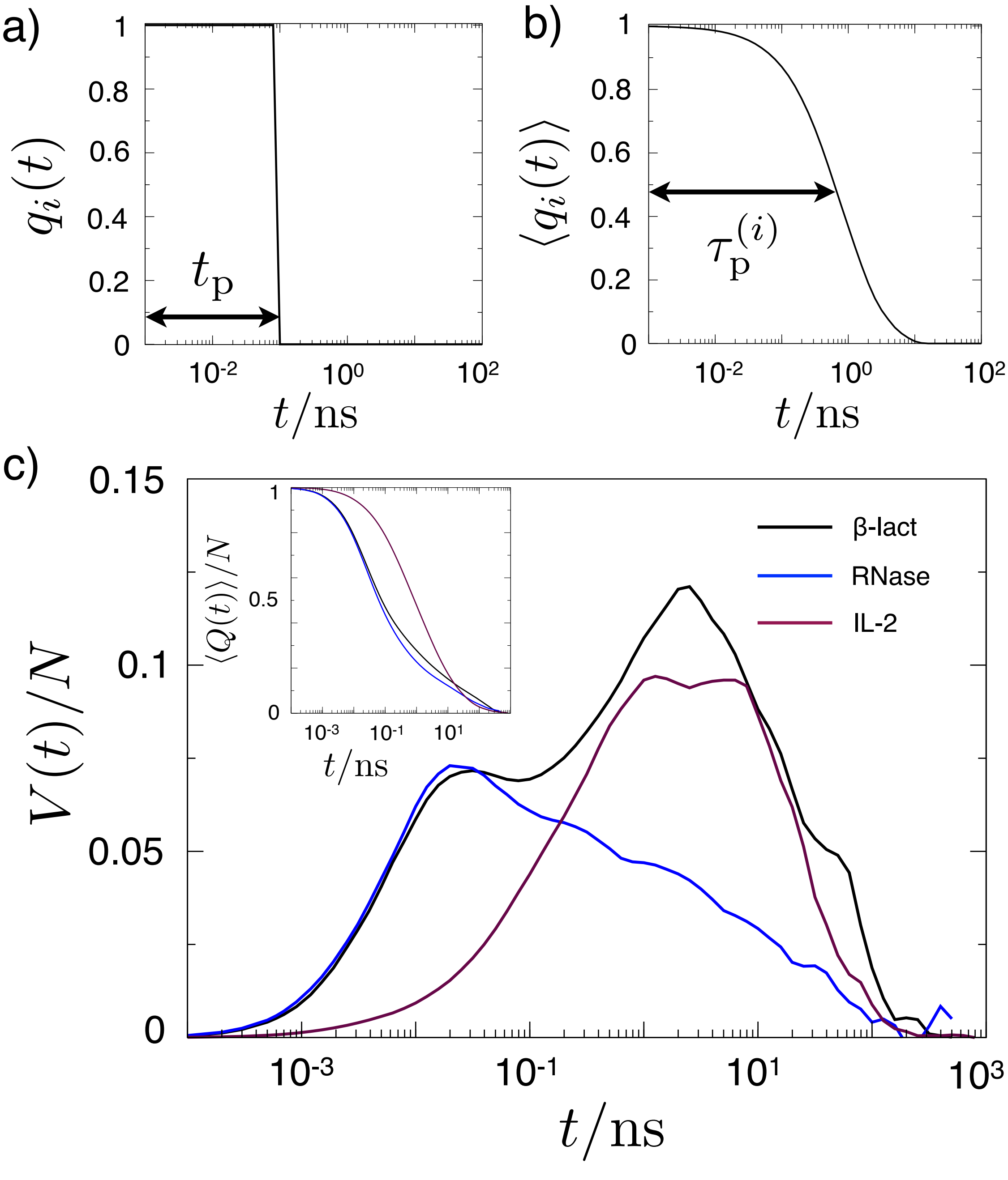

Figure 5.12: Side-chains are dynamically correlated with each other. (a) Illustration of the quantity $q_i(t)$ (Eqn. 5.10). $q_i(t)$ goes to zero when dihedral i undergoes a dynamical event; this is an example of a persistence time t_p for that dihedral. (b) The time average of $q_i(t)$ for a single dihedral i (Eqn. 5.11). The decay of $\langle q_i(t)\rangle$ indicates the average persistence time for dihedral i as shown. (c) Variance in $Q(t)$ due to correlations for IL-2 (maroon), β-lactamase (blact), and RNase H (blue). The decaying $\langle Q(t)\rangle$ function is shown in the inset. Both quantities are normalized by N, the number of dihedrals in each system that have at least one dynamical event over the course of the trajectory.

Bibliography

[1] M. D. Ediger, C. Angell, and S. R. Nagel, "Supercooled liquids and glasses," *The journal of physical chemistry*, vol. 100, no. 31, pp. 13200–13212, 1996.

[2] L. O. Hedges, R. L. Jack, J. P. Garrahan, and D. Chandler, "Dynamic order-disorder in atomistic models of structural glass formers," *Science*, vol. 323, no. 5919, pp. 1309–1313, 2009.

[3] D. Chandler, "Introduction to modern statistical mechanics," *Introduction to Modern Statistical Mechanics, by David Chandler, pp. 288. Foreword by David Chandler. Oxford University Press, Sep 1987. ISBN-10: 0195042778. ISBN-13: 9780195042771*, vol. 1, 1987.

[4] L. Berthier and G. Biroli, "Theoretical perspective on the glass transition and amorphous materials," *Reviews of Modern Physics*, vol. 83, no. 2, p. 587, 2011.

[5] P. G. Debenedetti and F. H. Stillinger, "Supercooled liquids and the glass transition," *Nature*, vol. 410, no. 6825, pp. 259–267, 2001.

[6] P. G. Debenedetti, *Metastable liquids: concepts and principles.* Princeton University Press, 1996.

[7] H. Tweer, J. H. Simmons, and P. B. Macedo, "Application of the environmental relaxation model to the temperature dependence of the viscosity," *The Journal of Chemical Physics*, vol. 54, no. 5, pp. 1952–1959, 1971.

[8] Y. S. Elmatad, D. Chandler, and J. P. Garrahan, "Corresponding states of structural glass formers," *The Journal of Physical Chemistry B*, vol. 113, no. 16, pp. 5563–5567, 2009.

[9] Y. S. Elmatad, D. Chandler, and J. P. Garrahan, "Corresponding states of structural glass formers. ii," *The Journal of Physical Chemistry B*, vol. 114, no. 51, pp. 17113–17119, 2010.

[10] A. S. Keys, L. O. Hedges, J. P. Garrahan, S. C. Glotzer, and D. Chandler, "Excitations are localized and relaxation is hierarchical in glass-forming liquids," *Physical Review X*, vol. 1, no. 2, p. 021013, 2011.

[11] R. Candelier, A. Widmer-Cooper, J. K. Kummerfeld, O. Dauchot, G. Biroli, P. Harrowell, and D. R. Reichman, “Spatiotemporal hierarchy of relaxation events, dynamical heterogeneities, and structural reorganization in a supercooled liquid,” *Physical review letters*, vol. 105, no. 13, p. 135702, 2010.

[12] L. O. Hedges, L. Maibaum, D. Chandler, and J. P. Garrahan, “Decoupling of exchange and persistence times in atomistic models of glass formers,” *The Journal of chemical physics*, vol. 127, no. 21, p. 211101, 2007.

[13] Y. Jung, J. P. Garrahan, and D. Chandler, “Excitation lines and the breakdown of stokes-einstein relations in supercooled liquids,” *Physical Review E*, vol. 69, no. 6, p. 061205, 2004.

[14] Y. Jung, J. P. Garrahan, and D. Chandler, “Dynamical exchanges in facilitated models of supercooled liquids,” *The Journal of chemical physics*, vol. 123, no. 8, p. 084509, 2005.

[15] W. Kob and H. C. Andersen, “Testing mode-coupling theory for a supercooled binary lennard-jones mixture. ii. intermediate scattering function and dynamic susceptibility,” *Physical Review E*, vol. 52, no. 4, p. 4134, 1995.

[16] G. Adam and J. H. Gibbs, “On the temperature dependence of cooperative relaxation properties in glass-forming liquids,” *The journal of chemical physics*, vol. 43, no. 1, pp. 139–146, 1965.

[17] X. Xia and P. G. Wolynes, “Fragilities of liquids predicted from the random first order transition theory of glasses,” *Proceedings of the National Academy of Sciences*, vol. 97, no. 7, pp. 2990–2994, 2000.

[18] J. P. Garrahan and D. Chandler, “Coarse-grained microscopic model of glass formers,” *Proceedings of the National Academy of Sciences*, vol. 100, no. 17, pp. 9710–9714, 2003.

[19] D. Chandler and J. P. Garrahan, “Dynamics on the way to forming glass: bubbles in space-time,” *Annual Review of Physical Chemistry*, vol. 61, pp. 191–217, 2010.

[20] A. S. Keys, J. P. Garrahan, and D. Chandler, “Calorimetric glass transition explained by hierarchical dynamic facilitation,” *Proceedings of the National Academy of Sciences*, vol. 110, no. 12, pp. 4482–4487, 2013.

[21] G. H. Fredrickson and H. C. Andersen, “Kinetic ising model of the glass transition,” *Physical review letters*, vol. 53, no. 13, p. 1244, 1984.

[22] F. Ritort and P. Sollich, “Glassy dynamics of kinetically constrained models,” *Advances in Physics*, vol. 52, no. 4, pp. 219–342, 2003.

[23] J. Jäckle and S. Eisinger, "A hierarchically constrained kinetic ising model," *Zeitschrift für Physik B Condensed Matter*, vol. 84, no. 1, pp. 115–124, 1991.

[24] P. Sollich and M. R. Evans, "Glassy time-scale divergence and anomalous coarsening in a kinetically constrained spin chain," *Physical review letters*, vol. 83, no. 16, p. 3238, 1999.

[25] H. Lindsay, W. Dozier, P. Chaikin, R. Klein, and W. Hess, "On the viscosity and shear modulus of strongly interacting colloids," *Journal of physics A: mathematical and general*, vol. 19, no. 13, p. 2583, 1986.

[26] G. Tarjus and D. Kivelson, "Breakdown of the stokes–einstein relation in supercooled liquids," *The Journal of chemical physics*, vol. 103, no. 8, pp. 3071–3073, 1995.

[27] Y. Jung, S. Kim, J. P. Garrahan, and D. Chandler, "Comment on" is there a breakdown of the stokes-einstein relation in kinetically constrained models at low temperature?" by o. blondel and c. toninelli, arxiv: 1307.1651," *arXiv preprint arXiv:1309.5894*, 2013.

[28] J. G. Berberian and R. H. Cole, "Approach to glassy behavior of dielectric relaxation in 3-bromopentane from 298 to 107 k," *The Journal of chemical physics*, vol. 84, no. 12, pp. 6921–6927, 1986.

[29] C. Angell, "Structural instability and relaxation in liquid and glassy phases near the fragile liquid limit," *Journal of non-crystalline solids*, vol. 102, no. 1, pp. 205–221, 1988.

[30] D. R. Neuville, L. Cormier, and D. Massiot, "Al coordination and speciation in calcium aluminosilicate glasses: Effects of composition determined by 27 al mq-mas nmr and raman spectroscopy," *Chemical geology*, vol. 229, no. 1, pp. 173–185, 2006.

[31] R. S. Smith and B. D. Kay, "Breaking through the glass ceiling: Recent experimental approaches to probe the properties of supercooled liquids near the glass transition," *The Journal of Physical Chemistry Letters*, vol. 3, no. 6, pp. 725–730, 2012.

[32] N. Karger, T. Vardag, and H.-D. Lüdemann, "Temperature dependence of self-diffusion in compressed monohydric alcohols," *The Journal of chemical physics*, vol. 93, no. 5, pp. 3437–3444, 1990.

[33] R. Rathbun and A. Babb, "Self-diffusion in liquids. iii. temperature dependence in pure liquids1," *The Journal of Physical Chemistry*, vol. 65, no. 6, pp. 1072–1074, 1961.

[34] R. Richert and C. Angell, "Dynamics of glass-forming liquids. v. on the link between molecular dynamics and configurational entropy," *Journal of Chemical Physics*, vol. 108, pp. 9016–9026, 1998.

[35] P. K. Dixon, N. Menon, and S. R. Nagel, “Comment on light scattering investigation of α and β relaxation near the liquid-glass transition of the molecular glass salol,” *Physical Review E*, vol. 50, no. 2, p. 1717, 1994.

[36] D. J. Plazek and J. H. Magill, “Physical properties of aromatic hydrocarbons. i. viscous and viscoelastic behavior of 1: 3: 5-tri-α-naphthyl benzene,” *The Journal of Chemical Physics*, vol. 45, no. 8, pp. 3038–3050, 1966.

[37] R. A. May, R. S. Smith, and B. D. Kay, “Mobility of supercooled liquid toluene, ethylbenzene, and benzene near their glass transition temperatures investigated using inert gas permeation,” *The Journal of Physical Chemistry A*, vol. 117, no. 46, pp. 11881–11889, 2013.

[38] K. R. Harris, J. J. Alexander, T. Goscinska, R. Malhotra, L. A. Woolf, and J. H. Dymond, “Temperature and density dependence of the selfdiffusion coefficients of liquid n-octane and toluene,” *Molecular Physics*, vol. 78, no. 1, pp. 235–248, 1993.

[39] H. Shintani and H. Tanaka, “Universal link between the boson peak and transverse phonons in glass,” *Nature materials*, vol. 7, no. 11, pp. 870–877, 2008.

[40] N. Lačević, F. W. Starr, T. Schrøder, and S. Glotzer, “Spatially heterogeneous dynamics investigated via a time-dependent four-point density correlation function,” *The Journal of chemical physics*, vol. 119, no. 14, pp. 7372–7387, 2003.

[41] L. Berthier and W. Kob, “The monte carlo dynamics of a binary lennard-jones glass-forming mixture,” *Journal of Physics: Condensed Matter*, vol. 19, no. 20, p. 205130, 2007.

[42] D. G. Thorpe, K. C. Schuster, D. Chandler, and J. P. Garrahan, “Corresponding states of structural glass formers. iii,” in preparation.

[43] G. Hinze and H. Sillescu, “2h nuclear magnetic resonance study of supercooled toluene: Slow and fast processes above and below the glass transition,” *The Journal of chemical physics*, vol. 104, no. 1, pp. 314–319, 1996.

[44] R. S. Smith and B. D. Kay, “The existence of supercooled liquid water at 150 k,” *Nature*, vol. 398, no. 6730, pp. 788–791, 1999.

[45] D. T. Limmer and D. Chandler, “Corresponding states for mesostructure and dynamics of supercooled water,” *Faraday discussions*, vol. 167, pp. 485–498, 2013.

[46] P. G. Debenedetti, “Supercooled and glassy water,” *Journal of Physics: Condensed Matter*, vol. 15, no. 45, p. R1669, 2003.

[47] D. T. Limmer and D. Chandler, "Phase diagram of supercooled water confined to hydrophilic nanopores," *The Journal of chemical physics*, vol. 137, no. 4, p. 044509, 2012.

[48] L. Liu, S.-H. Chen, A. Faraone, C.-W. Yen, and C.-Y. Mou, "Pressure dependence of fragile-to-strong transition and a possible second critical point in supercooled confined water," *Physical review letters*, vol. 95, no. 11, p. 117802, 2005.

[49] L. Liu, S.-H. Chen, A. Faraone, C.-W. Yen, C.-Y. Mou, A. I. Kolesnikov, E. Mamontov, and J. Leao, "Quasielastic and inelastic neutron scattering investigation of fragile-to-strong crossover in deeply supercooled water confined in nanoporous silica matrices," *Journal of Physics: Condensed Matter*, vol. 18, no. 36, p. S2261, 2006.

[50] F. Mallamace, M. Broccio, C. Corsaro, A. Faraone, U. Wanderlingh, L. Liu, C.-Y. Mou, and S.-H. Chen, "The fragile-to-strong dynamic crossover transition in confined water: nuclear magnetic resonance results.," *The Journal of chemical physics*, vol. 124, no. 16, pp. 161102–161102, 2006.

[51] D. W. Hwang, C.-C. Chu, A. K. Sinha, and L.-P. Hwang, "Dynamics of supercooled water in various mesopore sizes.," *The Journal of chemical physics*, vol. 126, no. 4, pp. 044702–044702, 2007.

[52] J. Hedström, J. Swenson, R. Bergman, H. Jansson, and S. Kittaka, "Does confined water exhibit a fragile-to-strong transition?," *The European Physical Journal Special Topics*, vol. 141, no. 1, pp. 53–56, 2007.

[53] H. Weingartner, "Self diffusion in liquid water. a reassessment," *Zeitschrift für physikalische Chemie*, vol. 132, no. 2, pp. 129–149, 1982.

[54] F. Prielmeier, E. Lang, R. Speedy, and H.-D. Lüdemann, "The pressure dependence of self diffusion in supercooled light and heavy water," *Berichte der Bunsengesellschaft für physikalische Chemie*, vol. 92, no. 10, pp. 1111–1117, 1988.

[55] K. T. Gillen, D. Douglass, and M. Hoch, "Self-diffusion in liquid water to -31 c," *The Journal of Chemical Physics*, vol. 57, no. 12, pp. 5117–5119, 1972.

[56] L. Onsager and L. Runnels, "Diffusion and relaxation phenomena in ice," *The Journal of Chemical Physics*, vol. 50, no. 3, pp. 1089–1103, 1969.

[57] K. Goto, T. Hondoh, and A. Higashi, "Determination of diffusion coefficients of self-interstitials in ice with a new method of observing climb of dislocations by x-ray topography," *Japanese journal of applied physics*, vol. 25, no. 3R, p. 351, 1986.

[58] A. Dehaoui, B. Issenmann, and F. Caupin, "Viscosity of deeply supercooled water and its coupling to molecular diffusion," *Proceedings of the National Academy of Sciences*, vol. 112, no. 39, pp. 12020–12025, 2015.

[59] W. S. Price, H. Ide, and Y. Arata, "Self-diffusion of supercooled water to 238 k using pgse nmr diffusion measurements," *The Journal of Physical Chemistry A*, vol. 103, no. 4, pp. 448–450, 1999.

[60] P. Charbonneau, Y. Jin, G. Parisi, and F. Zamponi, "Hopping and the stokes–einstein relation breakdown in simple glass formers," *Proceedings of the National Academy of Sciences*, vol. 111, no. 42, pp. 15025–15030, 2014.

[61] R. Mari and J. Kurchan, "Dynamical transition of glasses: From exact to approximate," *The Journal of chemical physics*, vol. 135, no. 12, p. 124504, 2011.

[62] N. F. Carnahan and K. E. Starling, "Equation of state for nonattracting rigid spheres," *The Journal of Chemical Physics*, vol. 51, no. 2, pp. 635–636, 1969.

[63] T. M. Truskett, S. Torquato, S. Sastry, P. G. Debenedetti, and F. H. Stillinger, "Structural precursor to freezing in the hard-disk and hard-sphere systems," *Physical review E*, vol. 58, no. 3, p. 3083, 1998.

[64] A. Buhot and J. P. Garrahan, "Crossover from fragile to strong glassy behavior in kinetically constrained systems," *Physical Review E*, vol. 64, no. 2, p. 021505, 2001.

[65] J. P. Garrahan and D. Chandler, "Geometrical explanation and scaling of dynamical heterogeneities in glass forming systems," *Physical review letters*, vol. 89, no. 3, p. 035704, 2002.

[66] L. Berthier and J. P. Garrahan, "Numerical study of a fragile three-dimensional kinetically constrained model," *The Journal of Physical Chemistry B*, vol. 109, no. 8, pp. 3578–3585, 2005.

[67] Y. S. Elmatad and A. S. Keys, "Manifestations of dynamical facilitation in glassy materials," *Physical Review E*, vol. 85, no. 6, p. 061502, 2012.

[68] A. Widmer-Cooper, H. Perry, P. Harrowell, and D. R. Reichman, "Localized soft modes and the supercooled liquid?s irreversible passage through its configuration space," *The Journal of chemical physics*, vol. 131, no. 19, p. 194508, 2009.

[69] J. Theiler, "Estimating fractal dimension," *JOSA A*, vol. 7, no. 6, pp. 1055–1073, 1990.

[70] M. Merolle, J. P. Garrahan, and D. Chandler, "Space–time thermodynamics of the glass transition," *Proceedings of the National Academy of Sciences of the United States of America*, vol. 102, no. 31, pp. 10837–10840, 2005.

[71] C. Bennemann, C. Donati, J. Baschnagel, and S. C. Glotzer, "Growing range of correlated motion in a polymer melt on cooling towards the glass transition," *Nature*, vol. 399, no. 6733, pp. 246–249, 1999.

[72] C. Donati, S. C. Glotzer, P. H. Poole, W. Kob, and S. J. Plimpton, "Spatial correlations of mobility and immobility in a glass-forming lennard-jones liquid," *Physical Review E*, vol. 60, no. 3, p. 3107, 1999.

[73] S. C. Glotzer, V. N. Novikov, and T. B. Schrøder, "Time-dependent, four-point density correlation function description of dynamical heterogeneity and decoupling in supercooled liquids," *The Journal of Chemical Physics*, vol. 112, no. 2, pp. 509–512, 2000.

[74] P. Chleboun, A. Faggionato, and F. Martinelli, "Time scale separation in the low temperature east model: rigorous results," *Journal of Statistical Mechanics: Theory and Experiment*, vol. 2013, no. 04, p. L04001, 2013.

[75] D. J. Ashton, L. O. Hedges, and J. P. Garrahan, "Fast simulation of facilitated spin models," *Journal of Statistical Mechanics: Theory and Experiment*, vol. 2005, no. 12, p. P12010, 2005.

[76] A. S. Keys, D. Chandler, and J. P. Garrahan, "Using the s ensemble to probe glasses formed by cooling and aging," *Physical Review E*, vol. 92, no. 2, p. 022304, 2015.

[77] K. Binder and D. Stauffer, "Statistical theory of nucleation, condensation and coagulation," *Advances in Physics*, vol. 25, no. 4, pp. 343–396, 1976.

[78] S. Auer and D. Frenkel, "Numerical prediction of absolute crystallization rates in hard-sphere colloids," *The Journal of chemical physics*, vol. 120, no. 6, pp. 3015–3029, 2004.

[79] A. P. Sutton and R. W. Balluffi, "Interfaces in crystalline materials," 1995.

[80] N. A. Gjostein and F. Rhines, "Absolute interfacial energies of [001] tilt and twist grain boundaries in copper," *Acta Metallurgica*, vol. 7, no. 5, pp. 319–330, 1959.

[81] W. Read and W. Shockley, "Dislocation models of crystal grain boundaries," *Physical Review*, vol. 78, no. 3, p. 275, 1950.

[82] J.-P. Poirier, *Creep of crystals: high-temperature deformation processes in metals, ceramics and minerals.* Cambridge University Press, 1985.

[83] P. M. Chaikin and T. C. Lubensky, *Principles of condensed matter physics*, vol. 1. Cambridge Univ Press, 2000.

[84] W. F. Smith and J. Hashemi, *Foundations of materials science and engineering.* McGraw-Hill, 2011.

[85] D. L. Olmsted, S. M. Foiles, and E. A. Holm, "Grain boundary interface roughening transition and its effect on grain boundary mobility for non-faceting boundaries," *Scripta Materialia*, vol. 57, no. 12, pp. 1161–1164, 2007.

[86] E. A. Holm and S. M. Foiles, “How grain growth stops: A mechanism for grain-growth stagnation in pure materials,” *Science*, vol. 328, no. 5982, pp. 1138–1141, 2010.

[87] H. Zhang, D. J. Srolovitz, J. F. Douglas, and J. A. Warren, “Grain boundaries exhibit the dynamics of glass-forming liquids,” *Proceedings of the National Academy of Sciences*, vol. 106, no. 19, pp. 7735–7740, 2009.

[88] K. H. Nagamanasa, S. Gokhale, R. Ganapathy, and A. Sood, “Confined glassy dynamics at grain boundaries in colloidal crystals,” *Proceedings of the National Academy of Sciences*, vol. 108, no. 28, pp. 11323–11326, 2011.

[89] E. Rabani, D. R. Reichman, P. L. Geissler, and L. E. Brus, “Drying-mediated self-assembly of nanoparticles,” *Nature*, vol. 426, no. 6964, pp. 271–274, 2003.

[90] F.-Y. Wu, “The potts model,” *Reviews of modern physics*, vol. 54, no. 1, p. 235, 1982.

[91] M. Kardar, *Statistical physics of fields.* Cambridge University Press, 2007.

[92] G. S. Grest, M. P. Anderson, and D. J. Srolovitz, “Domain-growth kinetics for the q-state potts model in two and three dimensions,” *Physical Review B*, vol. 38, no. 7, p. 4752, 1988.

[93] M. Anderson, G. Grest, and D. Srolovitz, “Computer simulation of normal grain growth in three dimensions,” *Philosophical Magazine B*, vol. 59, no. 3, pp. 293–329, 1989.

[94] J. Cahn, E. A. Holm, and D. J. Srolovitz, “Modeling microstructural evolution in two-dimensional two-phase microstructures,” in *Materials Science Forum*, vol. 94, pp. 141–158, Trans Tech Publ, 1992.

[95] G. Hassold and E. A. Holm, “A fast serial algorithm for the finite temperature quenched potts model,” *Computers in Physics*, vol. 7, no. 1, pp. 97–107, 1993.

[96] S. Katira, K. K. Mandadapu, S. Vaikuntanathan, B. Smit, and D. Chandler, “Pre-transition effects mediate forces of assembly between transmembrane proteins,” *Elife*, vol. 5, p. e13150, 2016.

[97] G. Job and F. Herrmann, “Chemical potential–a quantity in search of recognition,” *European journal of physics*, vol. 27, no. 2, p. 353, 2006.

[98] J. D. Weeks and G. H. Gilmer, “Dynamics of crystal growth,” *Adv. Chem. Phys*, vol. 40, no. 489, pp. 157–227, 1979.

[99] D. T. Limmer and D. Chandler, “Premelting, fluctuations, and coarse-graining of water-ice interfaces,” *The Journal of chemical physics*, vol. 141, no. 18, p. 18C505, 2014.

[100] S. Vaikuntanathan and P. L. Geissler, "Putting water on a lattice: The importance of long wavelength density fluctuations in theories of hydrophobic and interfacial phenomena," *Physical review letters*, vol. 112, no. 2, p. 020603, 2014.

[101] M. Frigo and S. G. Johnson, "The design and implementation of FFTW3," *Proceedings of the IEEE*, vol. 93, no. 2, pp. 216–231, 2005. Special issue on "Program Generation, Optimization, and Platform Adaptation".

[102] J. Mittal and G. Hummer, "Static and dynamic correlations in water at hydrophobic interfaces," *Proceedings of the National Academy of Sciences*, vol. 105, no. 51, pp. 20130–20135, 2008.

[103] K. C. Schuster, G. R. Bowman, and D. Chandler, "Facilitated intermittent dynamics in protein side-chains," in preparation.

[104] Y. Zhou, D. Vitkup, and M. Karplus, "Native proteins are surface-molten solids: application of the lindemann criterion for the solid versus liquid state," *Journal of molecular biology*, vol. 285, no. 4, pp. 1371–1375, 1999.

[105] K. Lindorff-Larsen, R. B. Best, M. A. DePristo, C. M. Dobson, and M. Vendruscolo, "Simultaneous determination of protein structure and dynamics," *Nature*, vol. 433, no. 7022, pp. 128–132, 2005.

[106] A. J. Wand, J. L. Urbauer, R. P. McEvoy, and R. J. Bieber, "Internal dynamics of human ubiquitin revealed by 13c-relaxation studies of randomly fractionally labeled protein," *Biochemistry*, vol. 35, no. 19, pp. 6116–6125, 1996.

[107] T. I. Igumenova, K. K. Frederick, and A. J. Wand, "Characterization of the fast dynamics of protein amino acid side chains using nmr relaxation in solution," *Chemical reviews*, vol. 106, no. 5, pp. 1672–1699, 2006.

[108] K. H. DuBay and P. L. Geissler, "Calculation of proteins' total side-chain torsional entropy and its influence on protein-ligand interactions," *Journal of molecular biology*, vol. 391, no. 2, pp. 484–497, 2009.

[109] G. R. Bowman and P. L. Geissler, "Extensive conformational heterogeneity within protein cores," *The Journal of Physical Chemistry B*, vol. 118, no. 24, pp. 6417–6423, 2014.

[110] A. J. Wand, "Dynamic activation of protein function: a view emerging from nmr spectroscopy," *Nature Structural & Molecular Biology*, vol. 8, no. 11, pp. 926–931, 2001.

[111] C.-J. Tsai, A. Del Sol, and R. Nussinov, "Allostery: absence of a change in shape does not imply that allostery is not at play," *Journal of molecular biology*, vol. 378, no. 1, pp. 1–11, 2008.

[112] K. H. DuBay, J. P. Bothma, and P. L. Geissler, "Long-range intra-protein communication can be transmitted by correlated side-chain fluctuations alone," *PLoS Comput Biol*, vol. 7, no. 9, p. e1002168, 2011.

[113] N. Popovych, S. Sun, R. H. Ebright, and C. G. Kalodimos, "Dynamically driven protein allostery," *Nature structural & molecular biology*, vol. 13, no. 9, pp. 831–838, 2006.

[114] S.-R. Tzeng and C. G. Kalodimos, "Protein dynamics and allostery: an nmr view," *Current opinion in structural biology*, vol. 21, no. 1, pp. 62–67, 2011.

[115] H. N. Motlagh, J. O. Wrabl, J. Li, and V. J. Hilser, "The ensemble nature of allostery," *Nature*, vol. 508, no. 7496, pp. 331–339, 2014.

[116] A. Widmer-Cooper, P. Harrowell, and H. Fynewever, "How reproducible are dynamic heterogeneities in a supercooled liquid?," *Physical review letters*, vol. 93, no. 13, p. 135701, 2004.

[117] D. Frenkel and B. Smit, *Understanding molecular simulation: from algorithms to applications*, vol. 1. Academic press, 2001.

[118] N. Metropolis, A. W. Rosenbluth, M. N. Rosenbluth, A. H. Teller, and E. Teller, "Equation of state calculations by fast computing machines," *The journal of chemical physics*, vol. 21, no. 6, pp. 1087–1092, 1953.

[119] L. Verlet, "Computer" experiments" on classical fluids. i. thermodynamical properties of lennard-jones molecules," *Physical review*, vol. 159, no. 1, p. 98, 1967.

[120] H. C. Andersen, J. D. Weeks, and D. Chandler, "Relationship between the hard-sphere fluid and fluids with realistic repulsive forces," *Physical Review A*, vol. 4, no. 4, p. 1597, 1971.

[121] D. R. Reichman and P. Charbonneau, "Mode-coupling theory," *Journal of Statistical Mechanics: Theory and Experiment*, vol. 2005, no. 05, p. P05013, 2005.

[122] W. Ketcham and P. Hobbs, "An experimental determination of the surface energies of ice," *Philosophical Magazine*, vol. 19, no. 162, pp. 1161–1173, 1969.

[123] T. Frolov and Y. Mishin, "Liquid nucleation at superheated grain boundaries," *Physical review letters*, vol. 106, no. 15, p. 155702, 2011.

[124] G. R. Bowman and P. L. Geissler, "Equilibrium fluctuations of a single folded protein reveal a multitude of potential cryptic allosteric sites," *Proceedings of the National Academy of Sciences*, vol. 109, no. 29, pp. 11681–11686, 2012.

[125] X. Wang, G. Minasov, and B. K. Shoichet, "Evolution of an antibiotic resistance enzyme constrained by stability and activity trade-offs," *Journal of molecular biology*, vol. 320, no. 1, pp. 85–95, 2002.

[126] Y. Duan, C. Wu, S. Chowdhury, M. C. Lee, G. Xiong, W. Zhang, R. Yang, P. Cieplak, R. Luo, T. Lee, *et al.*, "A point-charge force field for molecular mechanics simulations of proteins based on condensed-phase quantum mechanical calculations," *Journal of computational chemistry*, vol. 24, no. 16, pp. 1999–2012, 2003.

[127] E. R. Goedken, J. L. Keck, J. M. Berger, and S. Marqusee, "Divalent metal cofactor binding in the kinetic folding trajectory of escherichia coli ribonuclease hi," *Protein Science*, vol. 9, no. 10, pp. 1914–1921, 2000.

[128] S. Pronk, S. Páll, R. Schulz, P. Larsson, P. Bjelkmar, R. Apostolov, M. R. Shirts, J. C. Smith, P. M. Kasson, D. van der Spoel, *et al.*, "Gromacs 4.5: a high-throughput and highly parallel open source molecular simulation toolkit," *Bioinformatics*, p. btt055, 2013.

[129] D. Van Der Spoel, E. Lindahl, B. Hess, G. Groenhof, A. E. Mark, and H. J. Berendsen, "Gromacs: fast, flexible, and free," *Journal of computational chemistry*, vol. 26, no. 16, pp. 1701–1718, 2005.

[130] W. L. DeLano, "The pymol molecular graphics system," 2002.

[131] K. A. Feenstra, B. Hess, and H. J. Berendsen, "Improving efficiency of large timescale molecular dynamics simulations of hydrogen-rich systems," *J Comput Chem*, vol. 20, pp. 786–798, 1999.

[132] A. Onufriev, D. Bashford, and D. A. Case, "Exploring protein native states and large-scale conformational changes with a modified generalized born model," *Proteins: Structure, Function, and Bioinformatics*, vol. 55, no. 2, pp. 383–394, 2004.

[133] W. Humphrey, A. Dalke, and K. Schulten, "Vmd: visual molecular dynamics," *Journal of molecular graphics*, vol. 14, no. 1, pp. 33–38, 1996.

[134] J. E. Stone, "An efficient library for parallel ray tracing and animation," 1998.

Appendix A

Software and Simulation Details

In this appendix, we provide details of the software and simulation methods employed to produce the results in the preceding chapters.

A.1 Basic Simulation Methodology

While simulation methods are not the focus of this dissertation, the majority of the results presented were obtained using either Monte Carlo (MC) or molecular dynamics (MD) simulations. Simulation methods are valuable tools in chemistry because they allow for the exploration of time and length scales not accessible in experiments, as well as a convenient means to test theories. Below, we give brief descriptions of MC and MD simulation techniques as they relate to the research in this dissertation. Both of these techniques have a variety of complex implementations, but we cover only the basic principles here. Ref. [117] provides a more complete and accessible treatment of many MC and MD methods.

A.1.1 Monte Carlo Simulation

The Monte Carlo (MC) method is an approach for computing quantities in systems with many degrees of freedom, where analytical calculations are intractable. The MC method samples configuration space according to the Boltzmann factor $\exp[-\beta\mathcal{U}(\mathbf{r}^N)]$, where $\beta = 1/k_{\mathrm{B}}T$ is the inverse temperature and $\mathcal{U}(\mathbf{r}^N)$ is the energy of the configuration of N particles. In a MC simulation, new configurations are generated at random and are then accepted or rejected with a probability proportional to the appropriate statistical distribution for the system.

A common way of ensuring that the Monte Carlo simulation samples the correct equilibrium distribution is to impose a balance condition on the probabilities of transitioning between states. According to the Metropolis criterion [118], a trial move from state i to state j should be accepted with a probability

$$\mathrm{acc}(i \to j) = \min\big(1, e^{-\beta[\mathcal{U}(j)-\mathcal{U}(i)]}\big) \tag{A.1}$$

such that states are visited according to the relative probabilities between them. The basic Metropolis algorithm in the context of a lattice model simulation is as follows:

1. Randomly select a lattice site and compute its energy $\mathcal{U}(i)$, including any energetic contributions from interactions with neighboring sites
2. Propose a move to a new state and calculate the new energy $\mathcal{U}(j)$
3. Accept the proposed move with the probability in Eqn. A.1

In MC simulations, time is typically measured in units of “Monte Carlo sweeps.” In a single sweep, moves are proposed at M randomly chosen sites from the lattice, where M is the total number of sites in the system.

In Chapters 3 and 4 of this dissertation, we employ MC to simulate lattice models. MC can also be used to simulate particle systems, where Step 2 of the procedure above is modified to propose a random displacement instead of a new discrete state. However, MC is not typically used to study system dynamics, as the method generates random configurations that are not sequential in time. When information on particle dynamics is required, molecular dynamics is often the better choice.

A.1.2 Molecular Dynamics Simulation

Molecular dynamics (MD) methods allow for the computation of equilibrium properties of a classical system with many atoms or molecules. Each constituent particle has an associated position and momentum, and there may be a variety of forces acting upon it through interactions with other particles in the system. The positions and momenta of all particles in the system obey classical dynamics and thus evolve according to Newton’s laws of motion. A rudimentary procedure [117] is as follows:

1. Set parameters that specify the initial state and conditions of the system
2. Evaluate the forces acting on each particle in the system
3. Integrate Newton’s equations of motion and evolve positions and momenta of particles appropriately
4. Once equilibrated, compute measured quantities

In practice, Newton’s equations of motion are integrated numerically by choosing a discrete time step. The Verlet algorithm [119] is one such MD integration scheme, where the positions of particles at the next time step $t + \Delta t$ are dependent on their positions at times t and $t - \Delta t$, as well as the acceleration $\mathbf{f}(t)/m$ at time t

$$\mathbf{r}(t + \Delta t) \approx 2\mathbf{r}(t) - \mathbf{r}(t - \Delta t) + \frac{\mathbf{f}(t)}{m}\Delta t^2 \tag{A.2}$$

Care must be taken to ensure that the time step is large enough to make efficient progress, while small enough to avoid large increases in energy that destabilize the simulation.

The atoms and molecules in a MD simulation interact according to specified force fields. These forces may be as simple as a hard sphere potential, where the potential energy associated with two particles jumps from 0 to infinity once a threshold distance between them (typically corresponding to a particle diameter) is crossed. However, force fields may become significantly more complex, as is the case with biomolecular simulations. Bond angles, van der Waals forces, and electrostatic interactions between atoms must all be accounted for. A variety of biomolecular force fields exist and must be chosen carefully for each specific application. See Section A.2 for details on the MD simulations carried out for protein molecules in Chapter 5, as well as the specific force field used.

A.2 Protein Simulations

The results of Chapter 5 were obtained using molecular dynamics simulations of protein molecules. Initial structures used for simulations were drawn with PyMOL 1.5 [130]. All protein visualizations were made using VMD 1.9 [133, 134]. Molecular dynamics simulations were run using GROMACS 4.5 [128, 129]. All simulations were performed as described in Ref. [124], with the exception that here, conformations were stored every 100 fs. Brief overviews of all simulations are given below.

Native State IL-2

Two separate NVT simulations (200 ns and 1 μs in length) were started from PDB ID 1M47. Each simulation was run at 300 K with the AMBER03 force field [126] and TIP3P explicit solvent. V-sites were utilized with a 5 fs timestep [131].

For the isoconfigurationally averaged trajectories, a 100 ns simulation was initialized from the same IL-2 structure as above and the state of the system at 25 ns, 50 ns, 75 ns, and 100 ns taken as initial conditions. From these initial conditions, one thousand 50 ps trajectories were started with randomized velocities drawn from a 300 K Maxwell-Boltzman distribution. 5.10b shows ICA results for the 75 ns initial condition only; the other initial conditions show similar features.

Unfolded IL-2

Two separate 100 ns NVT simulations utilizing the AMBER03 force field [126] and TIP3P explicit solvent were started from an extended structure made in PyMOL [130] with the IL-2 sequence. After energy minimization, the backbone atoms were fixed while the side-chain atoms remained unconstrained for the simulation.

β-lactamase

Two separate NVT simulations (600 ns and 400 ns in length) were started from PDB ID 1JWP [125]. Each simulation was run at 300 K with the AMBER03 force field [126] and TIP3P explicit solvent, where 7 sodium ions were added to achieve charge neutrality. V-sites were utilized with a 5 fs timestep [131].

RNase H

Two separate NVT simulations (600 ns and 400 ns in length) were started from PDB ID 1F21 [127]. Each simulation was run at 300 K with the AMBER03 force field [126] and TIP3P explicit solvent, where 9 chlorine atoms were added to achieve charge neutrality. V-sites were utilized with a 5 fs timestep [131].

Valine Tripeptide

One 2 μs NVT simulation was started from a structure of three valine residues made in PyMOL [130]. The simulation was run at 300 K with the AMBER03 force field [126] and TIP3P explicit solvent.

A.3 Data Visualization

Many of the simulation data visualizations included in this dissertation (e.g., Figs. 3.6, 4.12, and 5.11) were created using the *VMDstream* library created by Aaron Keys. This library allows for the creation of custom movies and images by interacting with the Visualizing Molecular Dynamics (VMD) [133, 134] software through C++ code. Source code and examples can be found on Aaron's GitHub profile (github.com/askeys/vmdstream).